学 位 論 文

Construction and Control of Hierarchical Systems at the Interfaces on Functionalized Carbon Clusters

（化学修飾炭素クラスター界面における階層化システムの構築と制御）

平成２６年１２月博士（理学）申請

東京大学大学院理学系研究科
化学専攻

ゴルゴル　リカルド　ミゾグチ

— Abstract —

Carbon clusters have been widely used as scaffolds in the construction of hierarchical assemblies of organic and inorganic materials for applications in the field of biological and material sciences. Because of the unique shape, stability, and electron conductivity, assemblies of carbon clusters are expected to exhibit properties unprecedented to conventional mesoscopic assemblies. I investigated two nanocarbon assemblies of mesoscopic scaffold: a bilayer vesicle made of fullerene amphiphiles and aggregates of carbon nanohorns. The functional group introduced to the curved π-surface of fullerene or nanohorn is exposed on the surface of these assemblies, which allows the design of the interface on these clusters and thus control of their properties. In the present thesis, I developed the chemistry at the interfaces on carbons clusters based on precise molecular design and synthesis.

Chapter 1 describes the recent progress in the development and application of artificial mesoscopic assemblies. Self-assembly of fullerene amphiphiles in supramolecular vesicles is highlighted. In addition, the merit of using carbon clusters as substrates for observation of single molecule dynamics in electron microscope studies is discussed.

Chapter 2 describes the molecular recognition property of the fullerene vesicles in water. The vesicles made of nonpolar/polar/nonpolar fullerene amphiphile $R_5C_{60}^{-}K^{+}$ binds hydrophobic molecules in a way different to vesicles made of nonpolar/polar lipid molecules. The fullerene-rich interior of the fullerene bilayer is the primary binding site of aromatic molecules and it takes up planar molecules very well but not bulky molecules.

Chapter 3 describes the fullerene bilayer membranes as nanoreactors for polymer synthesis. The fullerene membrane is stabilized by orthogonal forces, π-π and hydrophobic interactions, that creates three regions: fullerene-rich core, alkyl interior and exterior. The location of the polymer chains in the bilayers could be controlled by installing different substituent groups to the fullerene amphiphile. Polymers of different regions produced supramolecular structures

of different morphology: capsules or particles.

Chapter 4 describes the decoration of fullerene vesicles with gold nanoparticles via interfacial adsorption. The fullerene vesicle bears hydrophobic groups on the surface that creates an interface in water and can be used as an adsorption site for surface-active nanoparticles. The assembly was sufficiently robust to grow the nanoparticles *in situ*. The high density of nanoparticles on the vesicle surface allowed interparticle coupling of the surface plasmon resonance.

Chapter 5 describes the imaging and analyses of the dynamics of single organic molecules covalently attached to carbon nanohorns by TEM. The motion of the single molecules could be controlled by the measurement conditions and the design of the specimen molecules.

Finally, chapter 6 summarizes the present thesis and presents possible outcomes for the chemistry of mesoscopic assemblies made of carbon clusters.

— Acknowledgements —

I am very grateful to my supervisor, Prof. Dr. Eiichi Nakamura, who guided me through the process of writing this thesis. His patience, motivation, enthusiasm, and immense knowledge helped me in all these years of research.

This thesis would not be possible without the support of assistant professor Dr. Koji Harano. I am very grateful for all the discussions, which were essential for understanding the experimental results, and for the guidance in the whole research process.

I would like to show my gratitude to associate professor Dr. Hayato Tsuji, associate professor Dr. Laurean Ilies, assistant professor Dr. Hideyuki Tanaka, and assistant professor Dr. Shunsuke Furukawa, who gave me good advices on the research life and made this laboratory a good and pleasurable place to work.

I appreciate the support of all members from Dr. Harano's subgroup; Dr. Chao Liu, Mr. Satoshi Okada, Mr. Junya Yamada, Mr. Kazutaka Shoyama, Mr. Kei Matsumoto, Mr. Junfei Xing, and Mr. Takuya Tsubota. I also thank the support from former members; Dr. Li-Fu Huang, Dr. Yonggang Zhen, Dr. Tatsuya Homma, Dr. Kosuke Minami, Dr. Akimitsu Narita, Mr. Shinya Takenaga, Ms. Eri Nishiyama, Mr. Shinichiro Mizuno, Ms. Kaori Kubo, Mr. Takakazu Seki, and Ms. Mami Nakatake. I am especially grateful for the support of Mr. Hirohisa Nitta.

I am indebted to all of my laboratory colleagues who showed immense support and patience to me. I also thank Mrs. Akemi Maruyama, who has supported the research in this lab for so many years.

I am thankful for the support of Prof. Dr. Kyoko Nozaki, assistant professor Dr. Shingo Ito, Mr. Takahiro Ohkawara and Mr. Wenhan Wang from The University of Tokyo, who allowed me to use the GPC machine.

I am grateful to Mr. Akira Yasuhara (JEOL Ltd.), Dr. Emrah Yücelen (FEI Company), associate professor Dr. Naoya Shibata (The University of Tokyo) and Dr. Akihito Kumamoto (The University of Tokyo) for the TEM measurements and meaningful discussion on the interpretation of the results. Some of the TEM measurements were conducted in the Research Hub for Advanced Nano Characterization, The University of Tokyo, and supported by "Nanotechnology Platform" (12024046), both sponsored by MEXT, Japan.

There are no words to describe how thankful I am to my parents, Mr. Jose Martinez Gorgoll and Mrs. Helena Emiko Mizoguchi Gorgoll, who gave me excellent education.

Lastly, I would like to thank the Japan Society for the Promotion of Science (JSPS), who gave me financial support during the period of my doctoral course (Research Fellowship for Young Scientists, No. 24-8773).

Ricardo Mizoguchi Gorgoll
December 2014

— List of Publication —

"Binding of Aromatic Molecules in the Fullerene-Rich Interior of a Fullerene Bilayer Vesicle in Water", Harano, K., Gorgoll, R. M., Nakamura, E. *Chem. Commun*. **49**, 7629–7631 (2013).

— Abbreviations —

AFM	Atomic Force Microscopy (Microscope)
APCI	Atmospheric Pressure Chemical Ionization
BF	Bright-Field Imaging
CNH	Carbon Nanohorn
DCC	Dicyclohexylcarbodiimide
DCM	Dichloromethane
DF	Dark-Field Imaging
DLS	Dynamic Light Scattering
DMAP	*N*,*N*-dimethyl-4-aminopyridine
DMF	*N*,*N*-Dimethylformamide
DPAT	Diphenylammonium triflate
DSS	4,4-dimethyl-4-silapentane-1-sulfonic acid
EDX	Energy-Dispersive X-ray Analysis
ESI	Electrospray Ionization
GPC	Gel Permeation Chromatography
HAADF	High-Angle Annular Dark-Field Imaging
HPLC	High Pressure (Performance) Liquid Chromatography
IR	Infrared Spectroscopy
ITO	Indium Tin Oxide
IZO	Indium Zinc Oxide
LLS	Laser Light Scattering
NMP	*N*-Methyl-2-Pyrrolidone
NMR	Nuclear Magnetic Resonance
ODCB	*o*-Dichlorobenzene
OEO	Olygoethylene Oxide
PEG:	Polyethylene Glycol
ROMP	Ring-Opening Metathesis Polymerization
SEM	Scanning Electron Microscopy (Microscope)
STEM	Scanning Transmission Electron Microscopy (Microscope)
TBAF	Tetra-*n*-Butylammonium Fluoride
TEO	Tetraethylene Oxide
TEM	Transmission Electron Microscopy (Microscope)
THF	Tetrahydrofran
TSU	*O*-(*N*-Succinimidyl)-*N*,*N*,*N*',*N*'-Tetramethyluronium Tetrafluoroborate
VT	Variable Temperature

— Contents —

– Chapter 1 –
General introduction

1.1 Science at the mesoscale

Mesoscale is commonly described as the boundary between quantum and classical sciences that connects the microscopic and macroscopic worlds (Figure 1-1).[1] There is no exact definition for mesoscale, which made Robert Laughlin, a physics Nobel laureate, to describe it as a "buzz word" of multiple definitions.[2] The lack of consensus is probably because the mesoscale is a wide field of science that embraces multiple disciplines: chemistry, physics and biology. Although there is no exact scientific definition, it is possible to attempt a description by the studies reported until now. A mesoscopic assembly is often a system in the size range of 100 nm – 1 μm developed by molecular design and manipulation to achieve novel physical properties for potential biological and material applications.[3] The development of the science at the mesoscale will help us understand and mimic natural phenomena. Moreover, a better understanding on how the molecular design affects the properties of bulk materials will allow the development of novel mesoscopic architectures that may produce new functionalities and, consequently, new technologies.

There are many examples of mesoscale systems in nature and the cell is probably the most complex set of mesoscopic systems reported until now.[4] For instance, the cell membrane produces a compartment in water that in combination with transmembrane proteins, polymers and chemicals, can regulate the transport of substances and reactions with precision, allowing the maintenance of life.[5] Most astonishingly, the cell membrane is formed via a bottom-up mechanism and its complex chemistry is possible by a dynamic composition of lipid molecules, which makes it challenging for chemists to reproduce such a system in a laboratory. The construction of artificial mesoscopic systems is still very far from producing complex systems such as the cell membrane.

In the last decades, the field of synthetic chemistry has developed considerably. One attempt of preparing mesoscopic systems with single molecules began with the synthesis of star-like polymers, dendrimers, by sequential growth of a core molecule with reactive ends. This synthetic approach succeeded in producing particles of controllable size.[6] However, control of the structure becomes difficult as the size increases. Hence, self-assembly of unit molecules into large structures became an essential tool for

the development of mesoscopic assemblies.[7]

In a similar way to the cell, artificial vesicles were prepared by the self-assembly of lipid molecules in water.[8] The lipid molecules organize into a bilayer membrane in a way that the polar head of the molecule is exposed to the aqueous environment on the vesicle surface, and the nonpolar tail forms the membrane interior. These vesicles, called liposomes, have been very useful as a model for the cell membrane; however, the high fluidity of lipid membranes makes their manipulation difficult. To address this issue, more robust vesicles were developed. The self-assembly of amphiphilic polymers produces vesicles, called polymersomes[9], that were demonstrated to be useful as smart materials[10].

In contrast to the soft structures made by amphiphilic molecules and polymers, coordination of metal ions and organic linkers makes rigid crystalline structures that have well-defined pores. Generally, coordination polymers are not dispersible in liquid media, and thus completely different outputs have been reported for the chemistry in rigid assemblies.

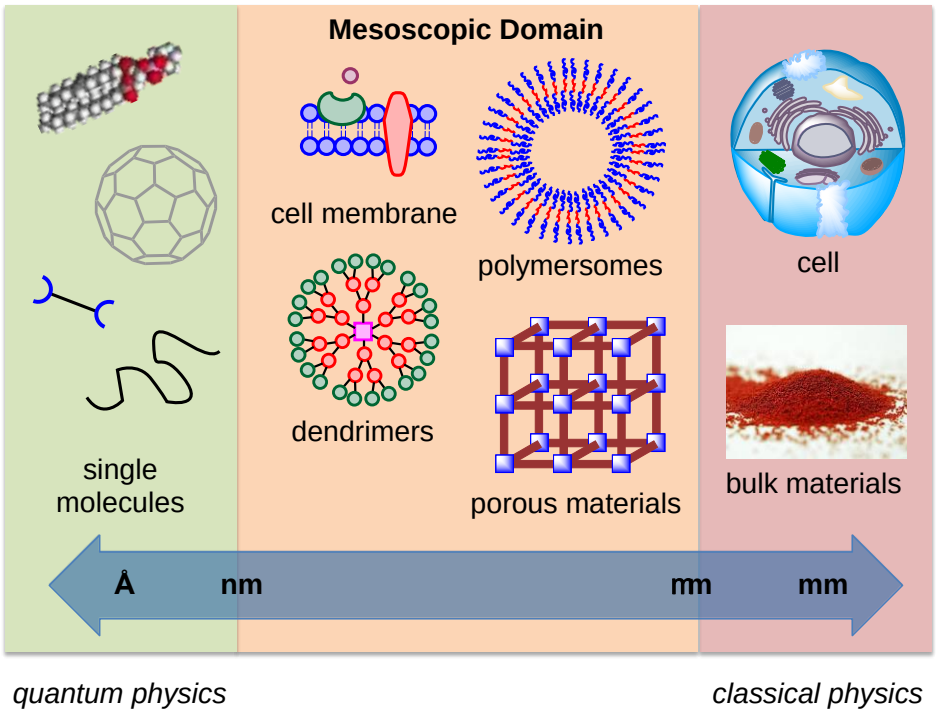

Figure 1-1. Science at different size scales.

A common characteristic of mesoscopic systems is the ability to interact

with extraneous molecules (Figure 1-2). In most of the reports, the interaction occurs by nonspecific hydrophobic effect, but the system can be designed to interact specifically with certain molecules via hydrogen or halogen bonding, π-π interaction, etc. For instance, hydrophobic molecules can be spontaneously incorporated in the hydrophobic interior of soft assemblies. Incorporation of molecules in lipid membranes by hydrophobic effect allows regulation of the membrane properties. [11] The loading of chemotherapeutical agents in membranes or dendrimers was reported in drug delivery applications.[12,13] In contrast to soft assemblies that can incorporate several types of molecules, the binding of molecules in rigid assemblies such as porous coordination polymers (PCP) is selective regarding the molecular size and shape. For instance, the design of PCP frameworks for selective binding was investigated for filtration[14] and storage[15] applications.

The interior of mesoscopic assemblies can also be used for confinement of reactions. For example, confinement in the hydrophobic environment of soft assemblies can accelerate reactions in water.[16] On the other hand, the rigidity of metal-organic frameworks allows the achievement of high selectivity in the reaction product (e.g. asymmetric reactions)[17].

The unique shape of mesoscopic assemblies can be used to mold polymeric objects. Polymerization inside a lipid membrane produces polymeric capsules[18], while polymerization in PCP produces linear polymer chains [19]. Mesoscopic assemblies have also been reported as templates for hierarchical structures of higher complexity where nanocrystals are added to grant new functionalities to the assembly.[20]

Recently, there have been many reports on the application of mesoscopic assemblies as a support for the investigation of molecules or molecular events that were unachievable by investigation of isolated molecules. Lipid membranes were used as a support for the investigation of the function of single protein molecules.[21] Fujita et al. obtained the crystal structure of a protein via encapsulation in nm-sized porous of coordination structures. [22] More recently, they observed several steps of a chemical reaction in a porous complex as X-ray snapshots.[23] Similarly, Shionoya et al. reported the binding process of small molecules in crystalline channels.[24]

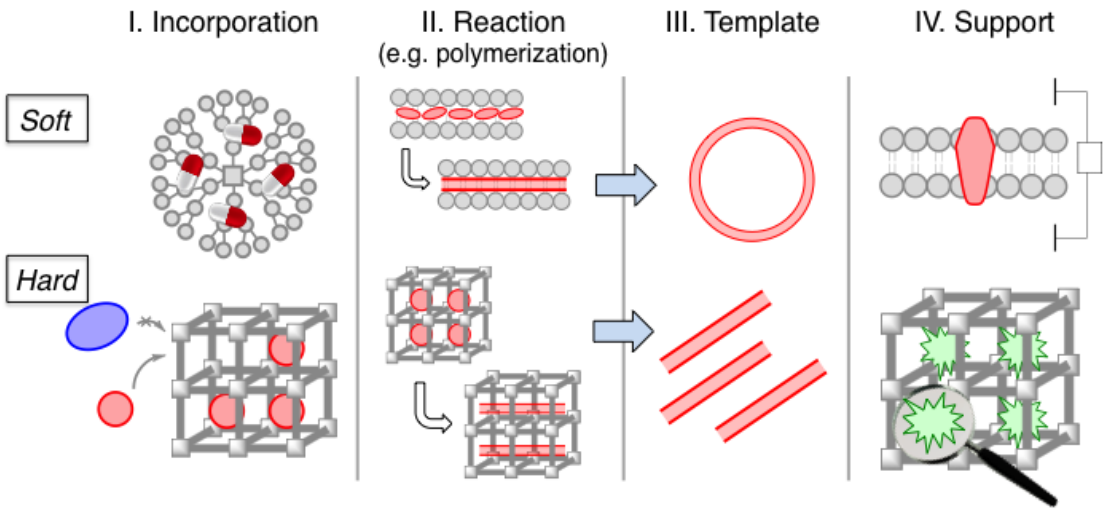

Figure 1-2. Applications of confinement in the interior of soft and hard mesoscopic assemblies: molecular incorporation, designable reaction site, template for nanocrystals and polymers, and support for observation of complex molecules and events.

Although the chemistry in soft and hard mesoscopic assemblies is similar, their output is very different. The discovery of carbon clusters and the development of their chemistry in recent years allowed the construction of mesoscopic systems that show properties of soft and hard assemblies. These assemblies may be used as a bridge between soft and hard assemblies in the construction of new materials that cover outputs that were previously unreachable by conventional mesoscopic assemblies.

1.1 The chemistry of sp^2 carbon clusters

Carbon-based materials have been used as molecular adsorbents in a wide range of applications (e.g. filtration, separation, catalyst support) for a long time, being the oldest reports from 1500 B.C. by the Egyptians.[25] However, the chemistry of carbon based materials was developed only in recent years with the discovery of sp^2 carbon clusters: fullerene in 1985[26], followed by carbon nanotubes in 1991[27,28,29] and graphene in 2004[30] (Figure 1-3). The well-defined structure of sp^2 carbon clusters, when compared to previous amorphous carbon materials, allowed the design of their chemistry. For instance, the introduction of functional groups to carbon clusters allows the regulation of the properties of the electron-rich surface and it has been proved useful in organic electronics (e.g. solar cells, sensors, etc.)[31].

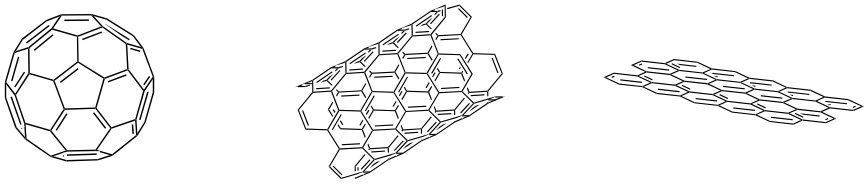

fullerene (1985) carbon nanotube (1991) graphene (2004)

Figure 1-3. sp^2 Carbon clusters: fullerene, carbon nanotube and graphene. The year of discovery is shown inside the parenthesis.

In addition to the electronic properties of the electron-rich surface, π–π interaction facilitates the assembly of carbon clusters in supramolecular structures. The strong intermolecular interaction was first suggested by the low solubility of these molecules. For instance, fullerene has extremely low solubility in water and organic solvents.[32] Moreover, the dispersion of carbon nanotubes and graphene is still challenging, making these materials difficult to handle.[33] By installing functional groups, it is possible to control the assembly of nanocarbons in solution producing mesoscopic assemblies.

There are many structural variations of carbon clusters (e.g. onion-type fullerenes, multi-walled carbon nanotubes, graphene nanoribbons, and so on). One variation of carbon nanotube that has been extensively investigated is the carbon nanohorn (Figure 1-4). Carbon nanohorn is the name given to horn-shaped carbon nanotubes.[34] It is formed as 100 nm dahlia-like aggregates by CO_2 laser ablation of carbon at room temperature. Because of the 100 nm size, spherical shape, and metal-free composition, carbon nanohorn aggregates were mainly investigated as drug carriers in biological applications.[35] However, the unique chemical properties of the horn-shaped nanotube also have prospective applications in material sciences.[36] The high curvature of the nanohorn edge makes it more reactive than the horn walls, allowing the introduction of functional groups selectively to the aggregate periphery and forming a well-defined hierarchical structure.[37] As carbon nanotubes, the characterization of the functionalized nanohorns is difficult, and the observation of the functional groups by TEM has been one way to support the introduction of functional groups.

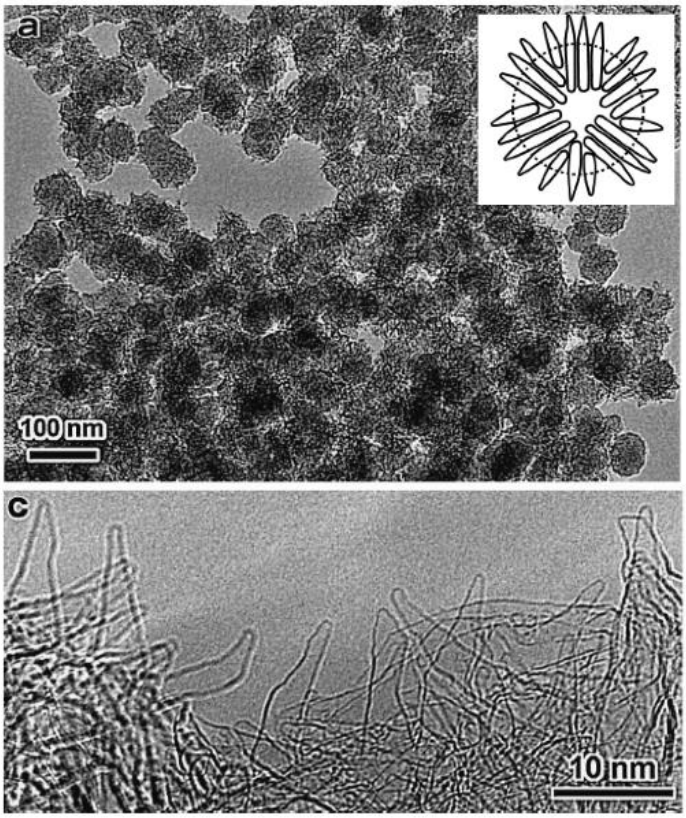

Figure 1-4. TEM images of carbon nanohorn aggregates. A schematic image is shown in the inset. Reprinted from ref. 34 with permission from Elsevier.

In this thesis, I developed the chemistry of mesoscopic assemblies made from fullerene and carbon nanohorn.

1.2 Vesicular assemblies of fullerene derivatives

The curved π-surface of fullerenes acts as an electrophile in chemical reactions (e.g. Bingel[38], Prato[39], or pentaaddition reactions[40]) and can be easily functionalized with diverse functional groups. The decrease in the extension of the π-conjugation of fullerene together with the introduction of functional groups increases the solubility of the fullerene derivative in organic solvents and water. Because of the different chemical nature of the fullerene and the substituent group moieties, the resultant molecule often forms an amphiphile that assembles into supramolecular structures in solution.

The introduction of a polar group to the fullerene molecule results in the formation of a common polar/nonpolar amphiphile. In a way similar to lipid molecules, these amphiphiles may assemble into bilayer vesicles in solution, where the fullerene moiety forms the membrane interior and the polar head is

exposed to water. Tour et al. reported the formation of 10–70 nm bilayer vesicles by dissolution and sonication of a cationic fullerene modified with dimethylpyrrolidinium iodide moiety in water (Figure 1-5a).[41] Similarly, Shinkai et al. reported the formation of 20-50 nm bilayer vesicles from the self-assembly of a fullerene derivative with two ammonium head groups.[42] Nakamura et al. developed a completely new type of amphiphile by introduction of the polar head to the fullerene framework (Figure 1-5b).[43] Deprotonation of pentaphenyl fullerene $Ph_5C_{60}H$ produced cyclopentadienyl on fullerene, giving the amphiphile $Ph_5C_{60}^-K^+$. The assembly of the potassium salt of pentaphenyl fullerenes in water produced anionic vesicles of 30 nm, as demonstrated by light scattering studies.

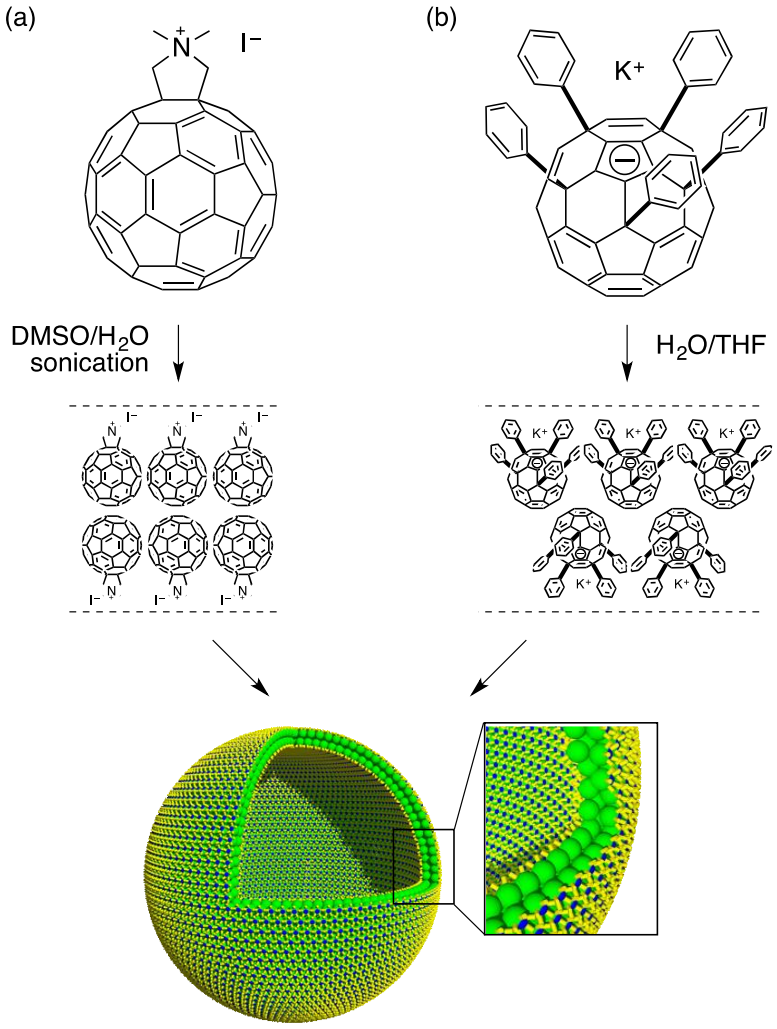

Figure 1-5. Vesicles made of fullerene derivatives modified with hydrophilic moieties by self-assembly in polar solvents.

Surprisingly, functionalization of fullerene with alkyl chains, which are nonpolar groups, also formed amphiphilic molecules that self-assembled in

supramolecular structures in solution. Nakanishi et al. reported that a delicate balance between π-π and van der Waals (vdW) interactions in this uncommon alkyl-conjugated fullerene amphiphile allows the fabrication of diverse structures, such as vesicles and nanoflowers (Figure 1-6). [44, 45] The hydrophobicity of the solvent determined the arrangement of the molecules in the supramolecular assemblies. In the hydrophobic *n*-decane, the alkyl moiety is exposed on the vesicle surface; in the hydrophilic 1,4-dioxane, the less hydrophobic fullerene is exposed on the vesicle surface. However, this was found to be a specific phenomenon, as the type of assembly formed by the fullerene derivative strongly depended on the alkyl group of fullerene.

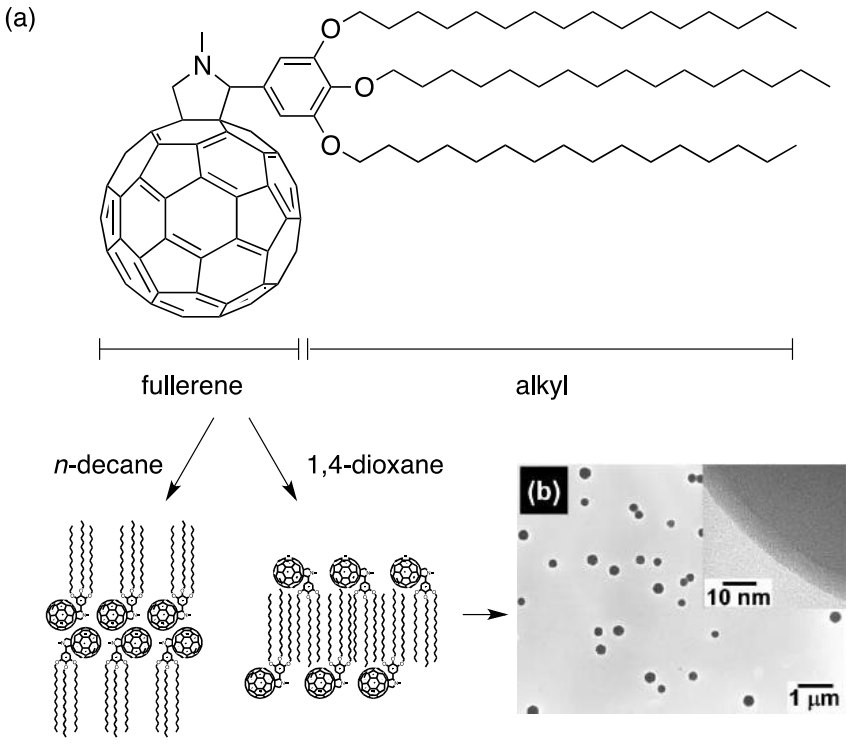

Figure 1-6. Vesicles made of uncommon fullerene amphiphiles, prepared by modification of fullerene with alkyl chains. Depending on the solvent polarity, the location of the fullerene moiety changes between outer surface and membrane interior. TEM image of vesicles was reproduced from ref. 44 with permission of The Royal Society of Chemistry.

In 2010, Nakamura *et al.* reported a new type of fullerene amphiphile, R_5C_{60}-K^+, that contains both hydrophilic moiety and alkyl (or perfluoroalkyl) chains (Figure 1-7). Alkyl and pefluoroalkyl chains were synthetically introduced to the *para* position of the phenyl substituents of the previously

reported pentaphenyl fullerene. This amphiphile has a unique ternary architecture formed by fullerene (nonpolar), cyclopentadienide anion (polar), and alkyl or perfluoroalkyl chains (nonpolar). Although this molecule did not have the usual nonpolar/polar motif, vesicles were formed upon injection to water. In this bilayer, the fullerene is located in the core and the (perfluoro)alkyl chains are exposed to water on the vesicle surface. This architecture produces orthogonal forces, π-π in the fullerene core and vdW in the alkyl interior, that strongly stabilize the fullerene membrane. Hereafter, the vesicles formed by the pentaadduct fullerene amphiphile $R_5C_{60}^-K^+$ are called as fullerene vesicles.

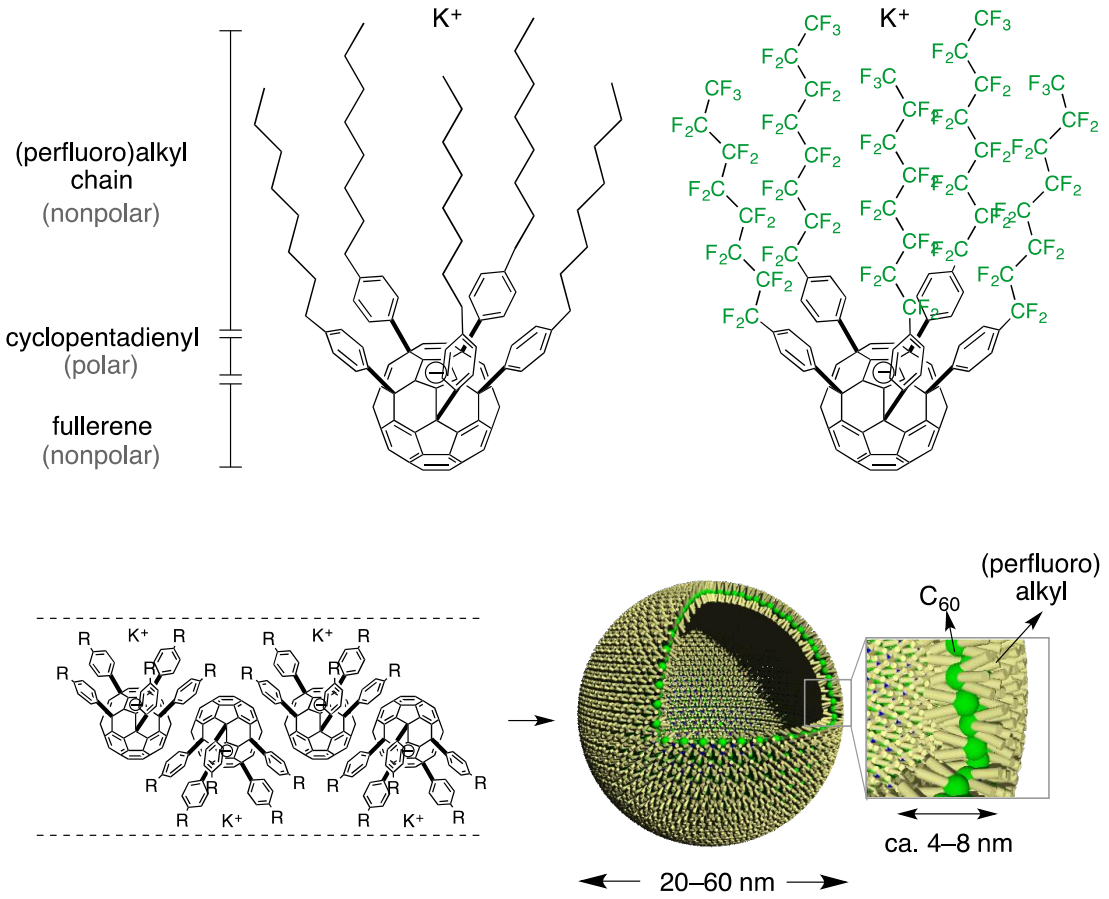

Figure 1-7. Self-assembly of fullerene pentaadduct amphiphiles of nonpolar / polar / nonpolar ternary architecture into interdigitated bilayer vesicles in water.

The formation of vesicles in the absence of alkyl groups in $Ph_5C_{60}^-K^+$ suggests that the polar moiety and the strong π- π interaction on the fullerene molecule are the driving forces for the vesicle formation in water; therefore, installation of diverse substituent R groups should not affect the formation of

the vesicles. The surface functionalization of the fullerene vesicles via chemical modification of the fullerene amphiphile allowed the control of the membrane properties and visualization of proteins in electron microscopy. Photocrosslinking of vesicles functionalized with the photo-active coumarin increased the vesicle stability against aggregation or fusion (Figure 1-8a).[46] The introduction of alkyne moiety to fullerene amphiphile produced vesicles that could be post-modified.[47] Introduction of biotin moiety to the vesicle surface via click reaction allowed non-covalent binding of avidin (Figure 1-8b). Because of the high stability of fullerenes under electron microscope conditions and the highly-ordered hierarchical structure of the vesicles, the avidin molecules could be observed on the vesicle surface as bulges by high-resolution scanning electron microscopy (Figure 1-8b, inset).

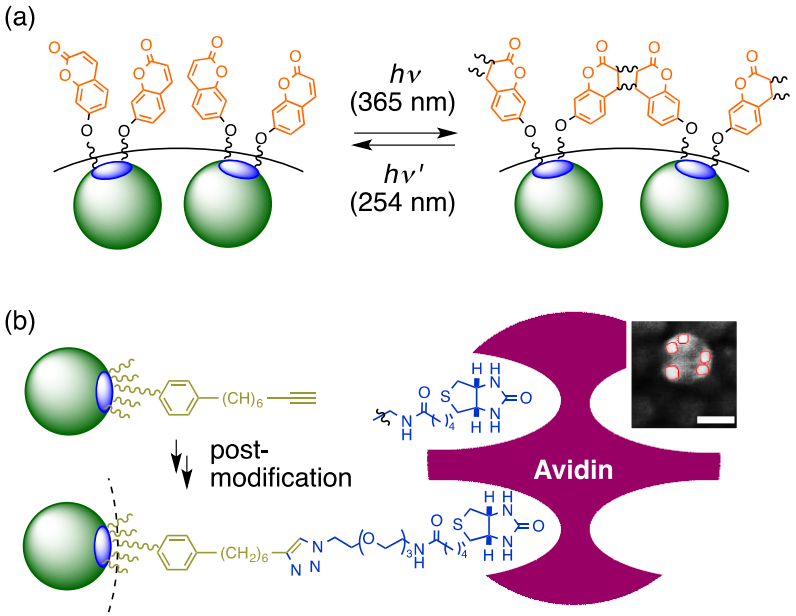

Figure 1-8. Examples of surface modification of fullerene vesicles via chemical modification of the fullerene amphiphile. (a) Modification of fullerene vesicles with photoresponsive coumarin pendant for photocrosslinking of the vesicle membrane. (b) Protein imaging on the vesicle surface via premodification of the fullerene amphiphile with alkyne, followed by post-modification with biotin and noncovalent binding to avidin. (Inset) SEM image of a vesicle modified with avidin. Scale bar is 20 nm. The SEM image was reproduced from ref. 47 with permission of The Royal Society of Chemistry.

The fullerene vesicle exhibits physical properties that differ from vesicles made of common amphiphiles, liposomes and polymersomes, as shown in Table 1-1. The fullerene vesicle is spontaneously formed as small

assemblies of 20–60 nm without requiring any further treatment, while lipid vesicles and polymersomes prepared by standard procedures are larger than 100 nm. Although the thickness of the fullerene bilayer is similar to the one of lipid bilayers, the permeability of water through the membrane can be more than 100 times lower. [48] The high water-tightness was explained by a permeation mechanism unique to fullerene membranes, where water molecules strongly bind to the fullerene core of the membrane. In contrast to liposomes and polymersomes that immediately collapse after removal of water, the fullerene vesicles can maintain their spherical shape as demonstrated by SEM.

Table 1-1. Comparison of the structure and properties of the membrane of bilayer vesicles made from lipid molecules, amphiphilic polymers, or fullerene pentaadduct amphiphiles.[a] Diameter of vesicles obtained in a typical procedure without treatment to reduce the assembly size. Data for polymersome is cited from ref. 9.

	liposome	polymersome	fullerene vesicle
amphiphile	nonpolar/polar	nonpolar/polar	nonpolar/polar/nonpolar
diameter[a] (nm)	> 100	> 200	20 – 60
membrane thickness (nm)	3 nm	> 8 nm	2 – 8 nm
water permeability (x 10^{-6} m / s)	25 – 150[49]	2.5 ± 1.2	0.17 – 3.36

The fullerene vesicles are much more robust than the previously reported vesicles assemblies. The question is whether the high robustness will allow the introduction of extraneous molecules for application as mesoscopic assemblies. Molecular dynamics simulation analysis of the fullerene membranes performed by Fileti *et al.* shows spatial non-uniformity in the mass density distribution and suggests the existence of many voids in the membrane (blue regions, Figure 1-9) that should be able to accommodate small hydrophobic molecules.[50]

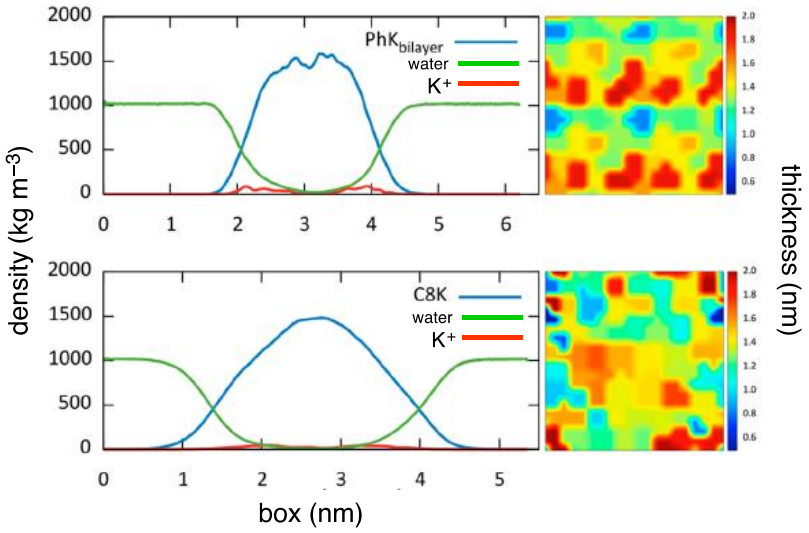

Figure 1-9. Molecular dynamics simulation of fullerene bilayer membranes made of (top) $Ph_5C_{60}^-K^+$ and (bottom) $(C_8H_{17}{}^pC_6H_4)C_{60}^-K^+$. (Left) Mass density distribution calculated along the z direction for the components of a fullerene interdigitated bilayer. (Right) Two-dimensional representation of the membrane thickness. Adapted with permission from ref 50. Copyright 2014 Americal Chemical Society.

The fullerene vesicle is a novel type of hierarchical assembly with unprecedented scaffold. The unique nonpolar/polar/nonpolar architecture may change the way it interacts with extraneous molecules, allowing the development of a new chemistry that was not possible with conventional soft and rigid assemblies.

1.3 Carbon nanohorn aggregates as supports for observation of single organic molecule in TEM movies

For a long time it was believed that the observation of organic molecules by transmission electron microscopy (TEM) would be impossible due to the damage of the sample by electron irradiation during the TEM measurement.[51] However, this was found not to apply to single organic molecules. As discussed for fullerene vesicles, carbon clusters are in general highly stable under electron irradiation and this high stability made possible the observation of organic molecules. By fixation to carbon clusters, the imaging of single organic molecules was achieved. Carbon clusters were found to be excellent substrates for the imaging of single organic molecules by TEM because of its single-atom thickness that do not disturb the image contrast of specimen molecules.

The observation of single organic molecules began with the imaging of

fullerene molecules encapsulated in a single-wall carbon nanotube, the so-called fullerene peapod (Figure 1-10).[52] Briggs et al. also noticed that a series of TEM images taken with a small time interval could show translational (Figure 1-10a) and rotational (Figure 1-10b) motions of fullerene in the nanotube.[53] Although the fullerene-nanotube interaction is strong, the uniformity of the nanotube surface allows the fullerene molecule to move from one position to another with only weak energy barriers. This result first suggested the use of TEM for imaging dynamics of single organic molecules as movies.

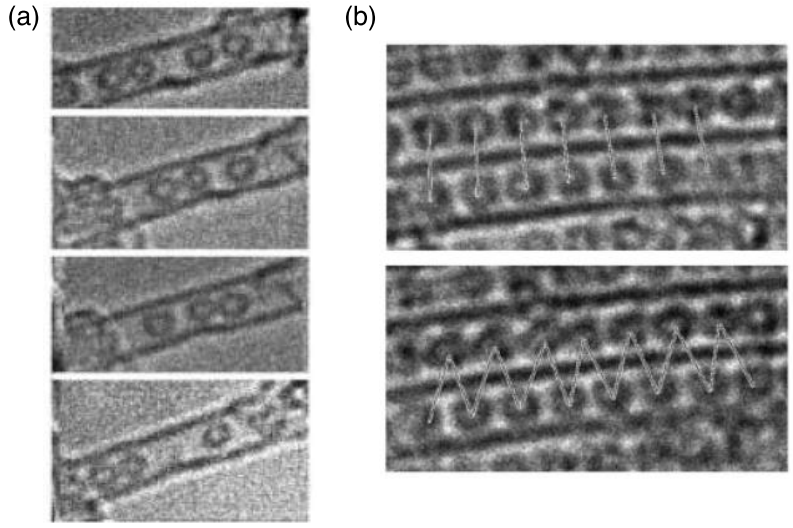

Figure 1-10. TEM images showing the translational and rotational motions of fullerenes in carbon nanotubes. (a) C_{82} and (b) Ce@C_{82} in a carbon nanotube. Time interval is (a) 10 s or (b) 1 min. Reprinted from ref. 53. Copyright © 2004 WILEY-VCH Verlag GmbH & Co. KGaA, Weinheim.

Nakamura et al. considered the feasibility of using TEM for the observation of single molecule phenomena. As a first attempt, an alkyl-conjugated carborane was designed for the observation of the conformational changes of an alkyl chain (Figure 1-11a).[54] In this molecular design, carborane was introduced as a maker for the alkyl chain, which has a weak contrast and is difficult to be localized in the nanotube. The TEM movie of this molecule showed the small conformational changes of the alkyl chain inside the nanotube (Figure 1-11b). As in the case of fullerene molecules, translational motion of the molecule was also observed.

By observation of TEM movies of other precisely designed molecules, Nakamura *et al.* succeeded in the imaging of several molecular phenomena,

such as reactions between fullerenes[55], trapping of molecules in carbon nanotubes defects[56] and conformational analysis of perfluoroalkyl chains.[57] However, the TEM observation of single molecules by encapsulation in carbon nanotubes had several limitations, such as the size of encapsulated molecules, the rather low encapsulation efficiency, the difficulty in locating the single molecules inside the long tubes, and the carbon nanotube background on the images of the single molecules.

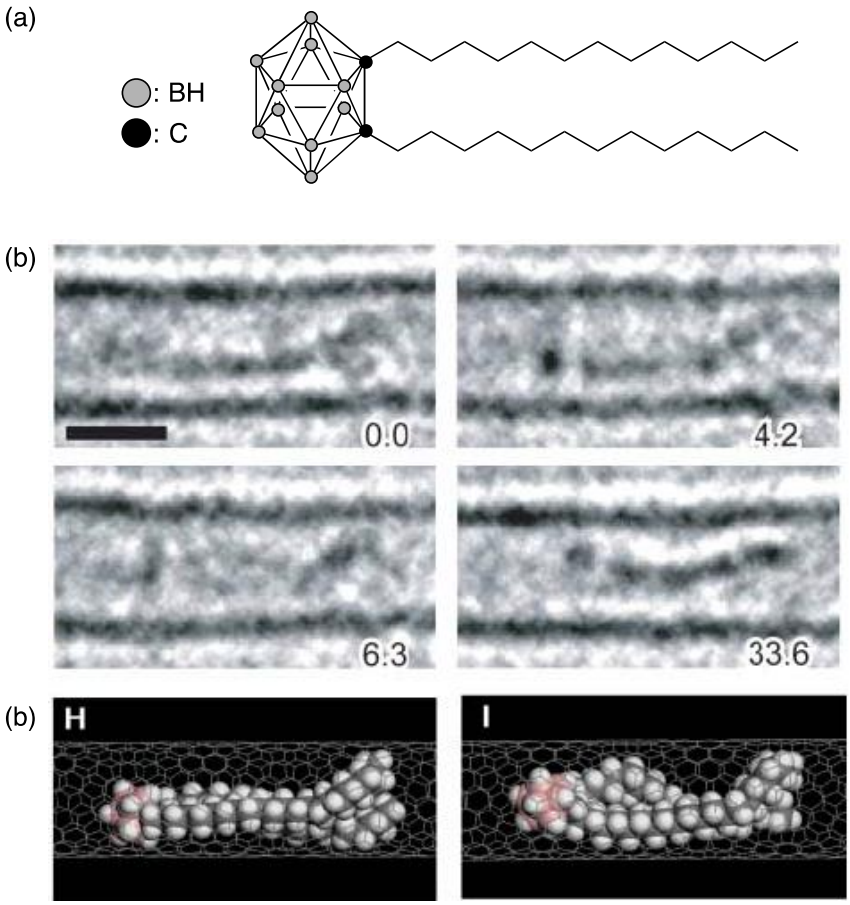

Figure 1-11. Conformational changes of a alkyl-conjugated carborane molecule (a) Chemical structure. (b) TEM images. Numbers shows the frame time in seconds. (c) Molecular model. From ref. 54. Reprinted with permission from AAAS.

The limitations of TEM imaging using carbon nanotubes were partially overcome by using carbon nanohorns instead. In the case of carbon nanohorn, the single molecule was covalently attached to the outer surface of the horn, which relieves the size limitation of the molecules. The edge of the nanohorn is functionalized much more efficiently than the nanotube walls and can be easily

recognized in TEM images. Nakamura *et al.* reported the first example of a movie of molecular motion using carbon nanohorn for a triamide biotinylated molecule (Figure 1-12).[58]

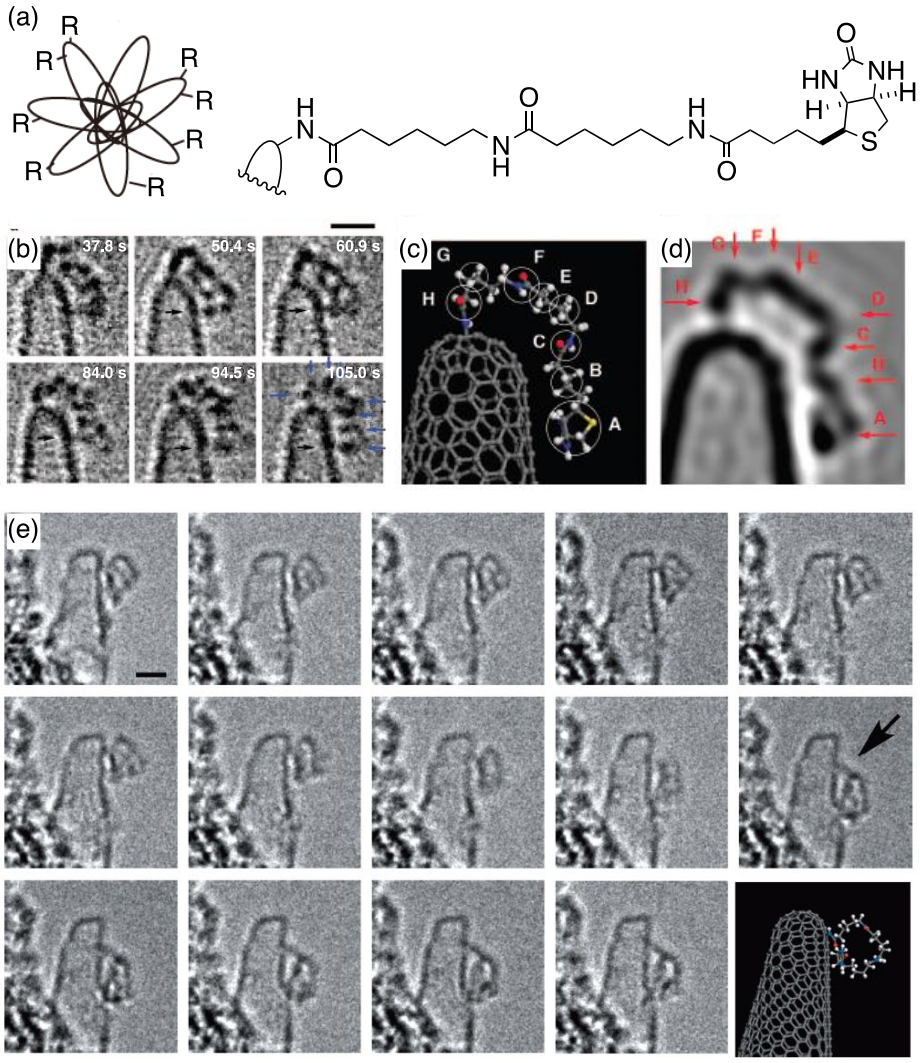

Figure 1-12. Conformational changes of a triamide biotinylated molecule covalently attached to a carbon nanohorn. (a) Molecular structure. (b) TEM images, (c) a plausible molecular model and (c) a TEM image simulated from the molecular mode. The figure captions refer to the time after initiation of the measurement. Reprinted with permission from ref. 58. Copyright 2008 American Chemical Society. (e) TEM images of a large conformational change. Scale bars are 1 nm. Reprinted from ref. 59. Copyright © 2013 WILEY-VCH Verlag GmbH & Co. KGaA, Weinheim.

The small conformational changes observed for this molecule were explained by the existence of several conformers of similar energy that could be exchanged during the electron irradiation by TEM. Not only small conformational changes, but also a large conformational change, showing the

molecule hovering on the nanohorn surface, was reported (Figure 1-12e). Although the resolution of the images was sufficient to propose plausible conformations for the molecule in the TEM image, the molecule image was blurred suggesting vibrational perturbations in the time scale of the TEM measurement.

To further understand the conformational changes found in the TEM movie, Nakamura *et al.* designed a rigid di(bromophenyl)benzamide (Y-shaped molecule, Figure 1-13a) modified carbon nanohorn.[60] The rigid Y shape of this molecule and the bromine atoms were introduced to facilitate the determination of the structural conformers observed in the TEM images. The bottom part of the molecule, which is inflexible, could be clearly observed during the whole movie (Figure 1-13b). On the other hand, the two rotating bromophenyl groups were observed only in a few images, suggesting a fast rotation of the C-C bond in the time scale of the TEM measurement. Movies taken at 4 K indicate that the C-C bond rotation does not stop even at very low temperatures.

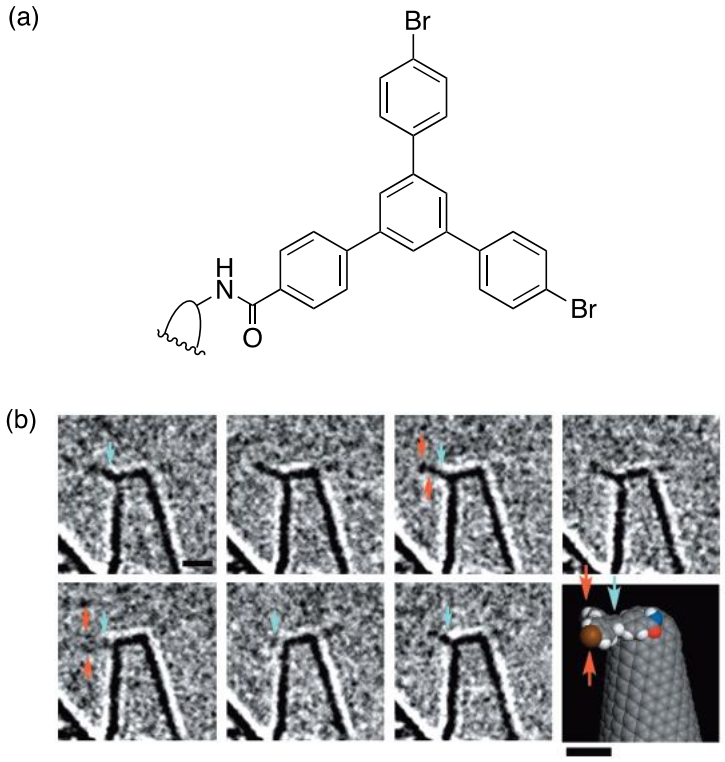

Figure 1-13. Rotation of Y-molecule (dibromophenylbenzamide) covalently attached to a carbon nanohorn. Scale bar is 1 nm. Reprinted from ref. 59. Copyright © 2013 WILEY-VCH Verlag GmbH & Co. KGaA, Weinheim.

The results reported by Nakamura *et al.* demonstrate the potential of TEM imaging and surface modification of carbon nanohorn for investigation of single molecule dynamics. The origin of the conformational changes of organic molecules observed by TEM is still not fully understood and more studies are necessary.

1.2 Summary of this study

The functional group introduced to the curved π-surface of fullerene or nanohorn is exposed on the surface of the fullerene vesicle or on the periphery of carbon nanohorn aggregates. The introduction of different functional groups allows the design of the interface on these clusters and the construction of highly ordered hierarchical structures. In this thesis, I investigated the chemistry of mesoscopic assemblies of carbon clusters in 6 chapters as follows.

Chapter 1 describes the recent progress in the development of artificial mesoscopic assemblies, focusing on the formation of supramolecular vesicles from the self-assembly of fullerene amphiphiles and on the TEM observation of single organic molecules on a carbon cluster substrate.

Chapter 2 describes the molecular recognition property of fullerene vesicles in water.

Chapter 3 describes the control of a polymerization reaction confined in fullerene bilayer membranes.

Chapter 4 describes the assembly of gold nanoparticles on fullerene vesicles via interfacial adsorption.

Chapter 5 describes the imaging of dynamic conformational changes of single organic molecules by TEM. The motion of the molecules could be accelerated by the measurement conditions and molecular design.

Chapter 6 puts in perspective the findings of this thesis and presents possible outcomes for the chemistry of mesoscopic assemblies of carbon clusters.

1.4 References

[1] Crabtree, G., Sarrao, J. *et al.* From Quanta to the Continuum: Opportunities for Mesoscale Science. *BESAC Meso Report* (2012)

[2] Reich, E. S. Mesoscale physics buzz eludes exact definition. *Nature News Blog*, 1 March 2012.

[3] Crabtree, G. & Sarrao, J. L. Opportunities for mesoscale science. *MRS Bull.* **37**, 1079–1088 (2009).

[4] Nakatsuji, N. Mesoscopic science, where materials become life and life inspires materials. A great opportunity to push back the frontiers of life, materials, and biomaterials sciences. *Biomater. Sci.* **1**, 9-10 (2013).

[5] van Meer, G., Voelker, D. R. & Feigenson, G. W. Membrane lipids: where they are and how they behave. *Nat. Rev. Mol. Cell Biol.* **9,** 112–124 (2008).

[6] Tomalia, D. A., Baker, H., Dewald, J., Hall, M., Kallos, G., Martin, S., Roeck, J., Ryder, J., Smith, P. A New Class of Polymers: Starburst-Dendritic Macromolecules. *Polym. J.* **17**, 117–132 (1985).

[7] Whitesides, G. M., Boncheva, M. Beyond molecules: self-assembly of mesoscopic and macroscopic components. Proc. Natl. Acad. Sci. USA **99**, 4769–4774 (2002).

[8] Bangham, A. D. & Horne, R. W. Negative staining of phospholipids and their structural modification by surface-active agents as observed in the electron microscope. *J. Mol. Bio.* **8**, 660–668 (1964).

[9] Discher, B. M., Won, Y. Y., Ege, D. S., Lee, J. C., Bates, F. S., Discher, D. E., Hammer, D. A. Polymersomes: tough vesicles made from diblock copolymers. *Science* **284**, 1143–1146 (1999).

[10] Oliveira, H. D., Thevenot, J. & Lecommandoux, S. Smart polymersomes for therapy and diagnosis: fast progress toward multifunctional biomimetric nanomedicines. *WIREs Nanomed. Nanobiotechnol.* **4**, 525–546.

[11] Chong, P. L. G., Zhu, W. W. & Venegas, B. On the lateral structure of model membranes containing cholesterol. *Biochim. Biophys. Acta, Biomembr.* **1788**, 2–11 (2009).

[12] Allen, T. M. & Cullis, P. R. Drug delivery systems: entering the main stream. *Science* **303**, 1818–1822 (2004).

[13] Adler-Moore, J. AmBisome targeting to fungal infections. *Bone Marrow Transplant.* **14**, S3–S7 (1996).

[14] Czaja, A. U., Trukhan, N. & Müller, U. Industrial applications of metal-organic frameworks. *Chem. Soc. Rev.* **38**, 1284–1293 (2009).

[15] Li, J.–R., Kuppler, R. K. & Zhou, H.–C. Selective gas adsorption and separation in metal-organic frameworks. *Chem. Soc. Rev.* **38**, 1477–1504 (2009).

[16] Hecht, S. & Fréchet, J. M. Light-drive catalysis within dendrimers: Designing amphiphilic singlet oxygen sensitizers. *J. Am. Chem. Soc.* **123**, 6959–6960 (2001).

[17] Ma, L., Abney, C. & Lin, W. Enantioselective catalysis with homochiral metal-organic frameworks. *Chem. Soc. Rev.* **38**, 1248–1256 (2009).

[18] Gomes, J. F. P. S., Sonnes, A. F.–P., Kronenberger, A., Fritz, J., Coelho, M. A. N., Fournier, D., Fournier–Nöel, C., Mauzac, M. & Winterhalter, M. Stable polymethacrylate nanocapsules from ultraviolet light-induced template radical polymerization of unilamella liposomes. *Langmuir* **22**, 7755–7759 (2006).

[19] Uemura, T., Yanai, N. & Kitagawa, S. Polymerization reaction in porous coordination polymers. *Chem. Soc. Rev.* **38**, 1228–1236 (2009).

[20] Dong, R., Liu, W. & Hao, J. Soft vesicles in the synthesis of hard materials. *Acc. Chem. Res.* **45**, 504–513 (2012).

[21] Tschodrich-Rotter, M. & Peters, R. An optical method for recording the activity of single transporters in membrane patches. *J. Microsc.* **192**, 114–125 (1998)

[22] Fujita, D., Suzuki, K., Sato, S., Yagi-Utsumi, M., Yamaguchi, Y., Mizuno, N., Kumasaka, T., Takata, M., Noda, M., Uchiyama, S., Kato, K. & Fujita, M. Protein encapsulation within synthetic molecular hosts. *Nat. Commun.* **3**, 1093 (2012).

[23] Ikemoto, K., Inokuma, Y., Rissanen, K. & Fujita, M. X-ray snapshot observation of palladium-mediated aromatic bromination in a porous complex. *J. Am. Chem. Soc.* **136**, 6892–6895 (2014).

[24] Kubota, R., Tashiro, S., Shiro, M. & Shionoya, M. In situ X-ray snapshot analysis of transient molecular adsorption in a crystalline channel. *Nat. Chem.* **6**, 913–918 (2014).

[25] Cheremisinoff, P. N., & Ellerbusch, F. *Carbon adsorption applications* (Ann Arbor Science Publishers, Inc. Ann Arbor, Michigan, 1980)

[26] Kroto, H. W., Heath, J. R., O'Brien, S. C., Curl, R. F. & Smalley, R. E. C_{60}: Buckminsterfullerene. *Nature* **318**, 162–163 (1985).

[27] Iijima, S. Helical microtubules of graphitic carbon. *Nature* **354**, 56–58 (1991).

[28] Iijima, S. & Ichihashi, T. Single-shell carbon nanotubes of 1-nm diameter. *Nature* **363**, 604–605 (1993).

[29] Bethune, D. S., Kiang, C. H., Vries, M. S. d., Gorman, G., Savoy, R., Vazquez, J. & Beyers, R. Cobalt-catalysed growth of carbon nanotubes with single-atomic-layer walls. *Nature* **363**, 605–606 (1993).

[30] Novoselov, K. S., Geim, A. K., Morozov, S. V., Jiang, D., Zhang, Y., Dubonos, S. V., Grigorieva, I. V. & Firsov, A. A. Electric field effect in atomically thin carbon films. *Science* **306**, 666–669 (2004).

[31] Dai, L. Carbon nanotechnology: Recent developments in chemistry, physics, materials science and device applications, 1st Edition, (Elsevier Science, Amsterdan, 2006).

[32] Mchedlov-Petrossyan, N. O. Fullerene in liquid media: an unsettling intrusion into the solution chemistry. *Chem. Rev.* **113**, 5249–5193 (2013).

[33] Hu, L., Hecht, D. S. & Grüner, G. Carbon nanotube thin films: fabrication, properties, and applications. *Chem. Rev.* **110**, 5790–5844 (2010).

[34] Iijima, S., Yudasaka, M., Yamada, R., Bandow, S., Suenaga, K., Kokai, F. & Takahashi, K. Nano-aggregates of single-walled graphitic carbon nano-horns. *Chem. Phys. Lett.* **309**, 165–170 (1999).

[35] Ajima, K., Yudasaka, M., Murakami, T., Maigné, Shiba, K. & Iijima, S. Carbon nanohorn as anticancer drug carriers. *Mol. Pharm.* **2**, 475–480 (2005)

[36] Dai, H., Yang, C., Ma, X., Lin, Y. & Chen, G. A higly sensitive and selective sensing ECL platform for naringin based on b-cyclodextrin functionalized carbon nanohorns. *Chem. Commun.* **47**, 11915–11917 (2011).

[37] Tasis, D., Tagmatarchis, N., Bianco, A. & Prato, M. Chemistry of carbon nanotubes. *Chem. Rev.* **106**, 1105–1136.

[38] Bingel, C. Cyclopropylation of fullerenes. *Chem. Ber.* **8**, 1957–1959 (1993)

[39] Maggini, M. & Scorrano, G. Addition of azomethine ylides to C60: Synthesis, characterization, and functionalization of fullerene pyrrolidines. *J. Am. Chem. Soc.* **115**, 9798–9799 (1993).

[40] Matsuo, Y. & Nakamura, E. Selective multiaddition of organocopper reagents to fullerenes. *Chem. Rev.* **108**, 3016–3028 (2008).

[41] Cassel, A. M., Asplund, C. L., Tour, J. M. Self-assembling supramolecular: nanostructures from a C_{60} derivative: Nanorods and vesicles. *Angew. Chem. Int. Ed.* **38**, 2403–2405 (1999).

[42] Sano, M., Oishi, K., Ishi-I, T. & Shinkai, S. Vesicle formation and its fractal distribution by bola-amphiphilic [60]fullerene. *Langmuir* **16**, 3773–3776 (2000).

[43] Zhou, S., Burger, C., Chu, B., Sawamura, M., Nagahama, N., Toganoh, M., Hackler, U. E., Isobe, H. & Nakamura, E. Spherical bilayer vesicles of fullerene-based surfactants in water: A laser light scattering study. *Science* **291**, 1944–1947 (2001).

[44] Nakanishi, T., Schmitt, W., Michinobu, T., Kurth, D. G. & Ariga, K. Hierarchical supramolecular fullerene architectures with controlled dimensionality. *Chem. Commun.* **48**, 5982–5984 (2005).

[45] Nakanishi, T. Supramolecular soft and hard materials based on self-assembly algorithms of alkyl-conjugated fullerenes. *Chem. Commun.* **46**, 3425–3436 (2010).

[46] Harano, K., Narita, A. & Nakamura, E. Photocrosslinking of the exterior of a fullerene bilayer that prevents vesicle aggregation. *Chem. Lett.* **43**, 877–879 (2014).

[47] Harano, K., Minami, K., Noiri, E., Okamoto, K. & Nakamura, E. Protein-coated nanocapsules via multilevel surface modification. Controlled preparation and microscopic analysis at nanometer resolution. *Chem Commun.* **49**, 3525–3527 (2013).

[48] Isobe, H., Homma, T. & Nakamura, E. Energetics of water permeation through fullerene membrane. *Proc. Nat. Acad. Sci. USA* **104**, 14895–14898 (2007).
[49] Bloom, M., Evans, E. & Mouritsen, O. G. Physical properties of the fluid lipid-bilayer component of cell membranes: a perspective. Q. Rev. Biopohys. **24**, 293–397 (1991)
[50] Fileti, E. E. Atomic description of fullerene-based membranes. *J. Phys. Chem. B* **118**, 12471–12477 (2014).
[51] Massover, W. H. New and unconventional approached for advancing resolution in biological transmission electron microscopy by improving macromolecular specimen preparation and preservation. *Micron* **42**, 141–151 (2011).
[52] Khlobystov, A. N., Britz, D. A. & Briggs, G. A. D. Molecules in carbon nanotubes. *Acc. Chem. Res.* **38**, 901–909 (2005).
[53] Khlobystov, A. N., Porfyrakis, K., Kanai, M., Britz, D. A., Ardavan, A., Shinohara, H., Dennis, T. J. S. & Briggs, G. A. D. Molecular motion of endohedral fullerenes in single-walled carbon nanotubes. *Angew. Chem. Int. Ed.* **43**, 1386–1389 (2004).
[54] Koshino, M., Tanaka, T., Solin, N., Suenaga, K., Isobe, H. & Nakamura, E. Imaging of single organic molecules in motion. *Science* **316**, 853 (2007).
[55] Koshino, M., Niimi, Y., Nakamura, E., Kataura, H., Okazaki, T., Suenaga, K. & Iijima, S. Analysis of the reactivity and selectivity of fullerene dimerization reactions at the atomic level. *Nat. Chem.* **2**, 117–124 (2010).
[56] Koshino, M., Solin, N., Tanaka, T., Isobe, H. & Nakamura, E. Imaging the passage of a single hydrocarbon chain through a nanopore. *Nat. Nanotechnol.* **3**, 595–597 (2008).
[57] Harano, K., Takenaga, S., Okada, S., Niimi, Y., Yoshikai, N., Isobe, H., Suenaga, K., Kataura, H., Koshino, M. & Nakamura, E. Conformational analysis of single perfluoroalkyl chains by single-molecule real-time transmission electron microscopic imaging. *J. Am. Chem. Soc.* **136**, 466–473 (2014).
[58] Nakamura, E., Koshino, M., Tanaka, T., Niimi, Y., Harano, K., Nakamura, Y. & Isobe, H. Imaging of conformational changes of biotinylated triamide molecules covalently bonded to a carbon nanotube surface. *J. Am. Chem. Soc.* **130**, 7808–7809 (2008).
[59] Nakamura, E. Movies of molecular motions and reactions: The single-molecule, real-time transmission electron microscope imaging technique. *Angew. Chem. Int. Ed.* **52**, 236–252 (2013).
[60] Harano, K., Homma, T., Niimi, Y., Koshino, M., Suenaga, K., Leibler, L. & Nakamura, E. Heterogeneous nucleation of organic crystals mediated by single-molecule templates. *Nat. Mater.* **11**, 877–881 (2012).

— Chapter 2 —

Binding of aromatic molecules in the fullerene-rich interior of a fullerene bilayer vesicle in water

2.1 Introduction: Binding of hydrophobic molecules in the membrane interior of bilayer vesicles

A vesicle made of a lipid, that has a polar head and nonpolar tail(s), is composed of a bilayer where the alkyl part forms the hydrophobic interior, and the hydrophilic part of the lipid is exposed to an aqueous environment.[1,2,3,4] The lipid vesicle readily takes up aliphatic molecules in the hydrophobic interior, which in many cases drastically change the physical properties of the lipid bilayer, resulting in weakening or stiffening of the bilayer and in reorganization or destruction of the whole compartment structure. As a consequence, the incorporation of extraneous molecules in lipid membranes is mostly limited to amphiphilic molecules (e.g. cholesterol, amphotericin B) that do not disturb the membrane architecture.

In contrast, a vesicle made of a nonpolar/polar/nonpolar (n-p-n') amphiphilic fullerene, $R_5C_{60}^-K^+$, is composed of a bilayer of amphiphilic fullerenes where the fullerene core is located in the interior, the R groups are exposed to an aqueous environment, and the anionic part is located in the middle (Figure 2-1a,b).[5,6,7,8,9] Because of the different architecture and the fullerene-rich interior, I expected that such vesicles would bind small hydrophobic molecules in a way different from lipid vesicles. Control of the loading capacity of the membranes would also be possible by the design of the hydrophobic environment of the vesicles with different R substituent groups on the fullerene.

In this chapter, the binding of small hydrophobic molecules in a series of fullerene bilayers was investigated. The binding site in the membranes was determined by the incorporation profile of a fluorescence probe and small hydrophobic molecules. The fullerene-rich interior of the fullerene bilayer (green in Figure 2-1b) is the primary binding site of a small aromatic molecule, while the outer layer (yellow) may host an aliphatic molecule when the R group bears aliphatic side chains—a type of selectivity thus far unexplored. The fullerene interior prefers a planar molecule (**3**) rather than a bulky molecule (**5**). The vesicle swells by up to 40% without loss of the spherical structure when loaded with a saturation amount of small molecules.

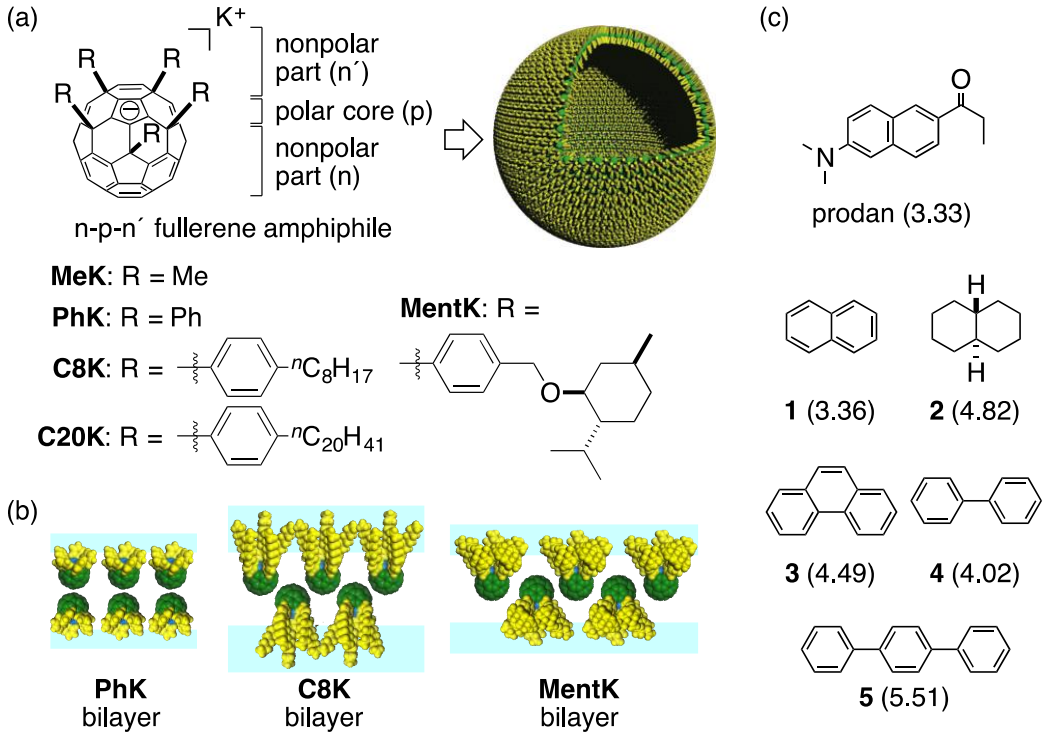

Figure 2-1. The bilayer made of amphiphilic fullerenes. (a) Schematic model of (interdigitated) bilayer vesicles constructed from fullerene anions $R_5C_{60}^-K^+$ with nonpolar/polar/nonpolar structure. (b) Schematic image of the bilayer. (c) The structures of prodan and hydrocarbons investigated in this study. 1-Octanol/water partition coefficients (logP_{ow}) of the compounds are shown in parentheses.

2.2 Synthesis of a vesicle with bulky alkyl substituents

Fullerene vesicles with different R substituents on the surface were prepared: **MeK**, **PhK**, **C8K** and **C20K** (Figure 2-1a). As previously reported, these vesicles form spontaneously when a THF solution of $R_5C_{60}^-K^+$ is injected into water at room temperature.[9] **MeK** and **PhK** represent an all-aromatic molecular structure lacking aliphatic substituents (n′-part), and **C8K** and **C20K** represent an archetypal n-p-n′ structure. The vesicle is much smaller (20–60 nm in diameter) than lipid vesicles (sub-μm to μm size), almost perfectly spherical and the size distribution is narrow without any purification (dynamic light scattering (DLS) analysis, Figure 2-12). The vesicle is very rigid and robust, both in water and in the vacuum of an electron microscope, because of strong intermolecular π–π interactions and the high hydrophobicity of the fullerene core.[9]

By installing bulky alkyl groups instead of long alkyl chains as in **C8K** or **C20K**, it should be possible to loose this bilayer structure and maximize the

loading of the hydrophobic molecules. For this purpose, I synthesized a new fullerene bearing five menthyloxy groups (**MentK**) according to the procedure described previously (Figure 2-2a),[9] and compared the properties of the **MentK** vesicle with other vesicles. The formation of **MentK** vesicle was confirmed by DLS and electron microscopy. Dissolution of **MentK** in water produced vesicles of 21.5 ± 0.2 nm in hydrodynamic diameter (DLS, Figure 2-2b). The spherical morphology was also observed by scanning electron microscopy (STEM) on an amorphous carbon film after removal of water by reduced pressure (Figure 2-2c). Note that the menthyloxy group is the largest group to be accommodated in a fullerene vesicle (Figure 2-1b).

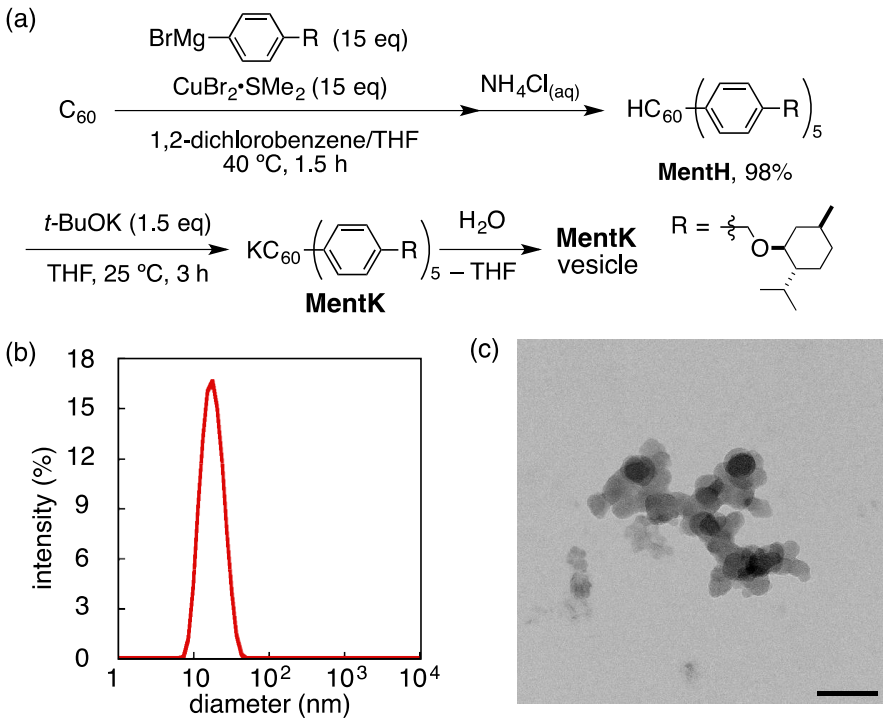

Figure 2-2. Synthesis and characterization of **MentK** vesicles. (a) Synthesis of **MentK**. (b) Size distribution of **MentK** vesicle determined in water at 25 °C by DLS. (c) STEM images of an agglomerate of **MentK** vesicles on an amorphous carbon film. The vesicles can be observed without the use of staining techniques. Scale bar is 100 nm.

Further characterization of **MentK** vesicles indicated that the bilayer of this vesicle is much more flexible than other bilayers. The ^{1}H NMR measurement of the **MentK** vesicle in D_2O at room temperature provided the first information on its flexibility: the menthyloxy and phenyl groups were observed as broad signals (Figure 2-3, top), as opposed to the structurally rigid

vesicles of **PhK**, **C8K** and **C20K**, for which no ^{1}H NMR signals could be seen below 50 °C (bottom)[9].

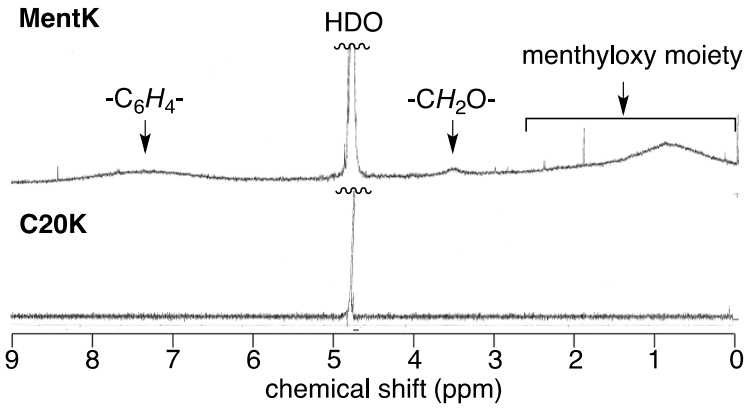

Figure 2-3. ^{1}H NMR spectra of **MentK** and **C20K** in D_2O at 20 °C.

Unlike the **MeK** to the **C20K** vesicles that maintain their spherical shape under diverse conditions,[9,10] the **MentK** vesicle almost entirely collapsed on an indium–tin oxide (ITO) surface, as observed by scanning electron microscopy (Figure 2-4), suggesting that the bulky menthyloxy groups reduces structural integrity of the vesicle to make the bilayer flexible.

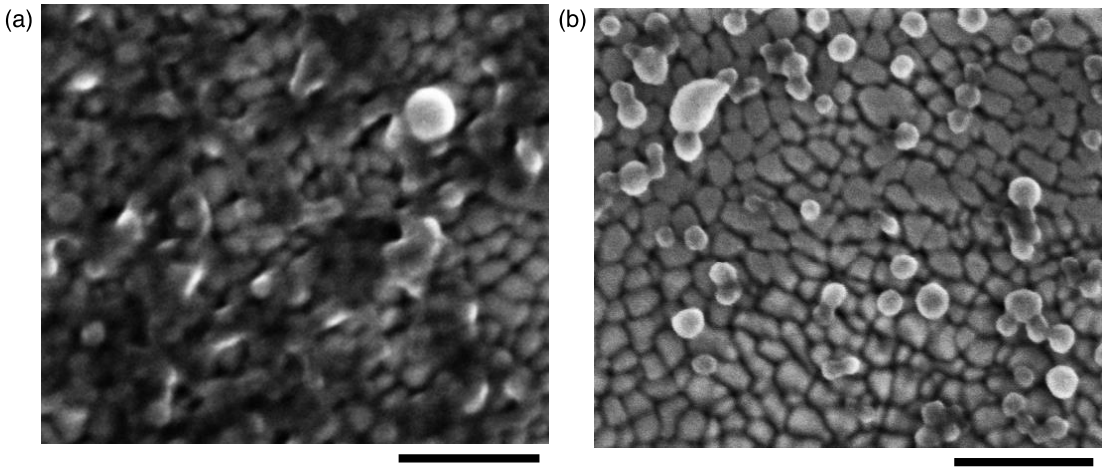

Figure 2-4. SEM images of (a) **MentK** and (b) **PhK** vesicles on ITO/glass substrate. Scale bars are 100 nm. Images were taken at an acceleration voltage of 1.5–2 kV and a current intensity of 6.3–25 pA.

Note, however, that the **MentK** vesicle is still as watertight as the others are (i.e., 2.20 ± 0.05 × 10^{-7} m/s at 20 °C), because the fullerene moiety largely

controls the water permeability (Figure 2-5).[7,9] The permeability coefficient *P* of **MentK** vesicle uniformly declines with the increase in the temperature (Figure 2-5a), as in **C20K** vesicles. As in other fullerene vesicles, water permeation though the fullerene membrane has a high entropy cost in contrast to a low enthalpy cost, due to the binding of water molecules to the fullerene moiety of the membrane (Figure 2-5b).

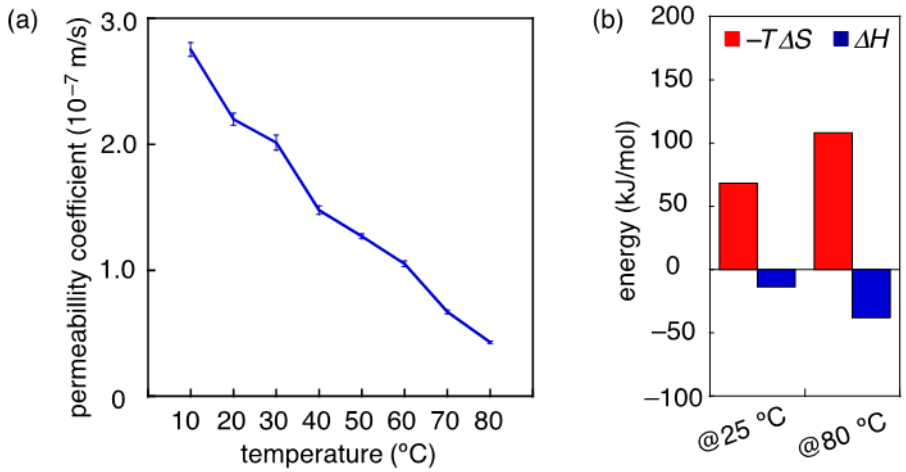

Figure 2-5. Water permeation through **MentK** membrane. (a) Temperature dependence of water permeability of **MentK** vesicle: 10 °C: (2.75 ± 0.06) x 10^{-7}, 20 °C: (2.20 ± 0.05) x 10^{-7}, 30 °C: (2.01 ± 0.06) x 10^{-7}, 40 °C: (1.48 ± 0.03) x 10^{-7}, 50 °C: (1.27 ± 0.02) x 10^{-7}, 60 °C: (1.05 ± 0.02) x 10^{-7}, 70 °C: (0.69 ± 0.01) x 10^{-7}, 80 °C: (0.43 ± 0.01) x 10^{-7} m s^{-1}. Error bars show the standard errors of mean of three measurements. (b) Activation enthalpy ($\Delta H^{\ddagger}$, blue bars) and activation entropy ($-T\Delta S^{\ddagger}$, red bars) values for water permeation at 25 and 80 °C. 25 °C: $\Delta H^{\ddagger}$ = –13.7, $-T\Delta S^{\ddagger}$ = 68.3 kJ/mol; 80 °C: $\Delta H^{\ddagger}$ = –38.0, $-T\Delta S^{\ddagger}$ = 108.0 kJ/mol.

2.3 Determination of the binding site of extraneous molecules in fullerene bilayers

Prodan (octanol-water partition coefficient logP_{ow} = 3.33)[11], a fluorescent dye commonly used to study the binding behavior of lipid vesicles[12], was used to probe in what part of the bilayer the fullerene vesicle traps organic molecules. Thus, a 20 μM aqueous solution of prodan (1 equiv to fullerene, containing 2.50% methanol) was added to a 20 μM solution of a R_5C_{60}-K^+ vesicle and stirred for 12 h. Most conspicuously, the fluorescence of prodan was quenched almost entirely (88% to 99% against the reference fluorescence intensity measured in water; Figure 2-6). Inclusion in the **MeK** and **C20K** vesicles

resulted in 99% quenching and 88% in **C8K**. Prodan in the **MentK** vesicle was quenched by 91%. In light of the ability of fullerene to quench effectively the excited state of nearby molecules,[13] it was considered that prodan is bound close to the internal fullerene array. This is supported by the correlation of the quenching and the λ_{max} of the fluorescence, which is related to the hydrophobicity of the environment of the prodan dye.[14] The fluorescence spectrum of this aqueous solution showed that the fluorescence maximum shifted from 502 (which corresponds to 100% methanol),[14] to 512 (25% ethanol in water) to 516 nm (10% 2-propanol in water) for **PhK**, **MentK** and **C8K** vesicles (Figure 2-6b), suggesting that the prodan environment becomes less hydrophobic in this order (the same order as the quenching efficiency).

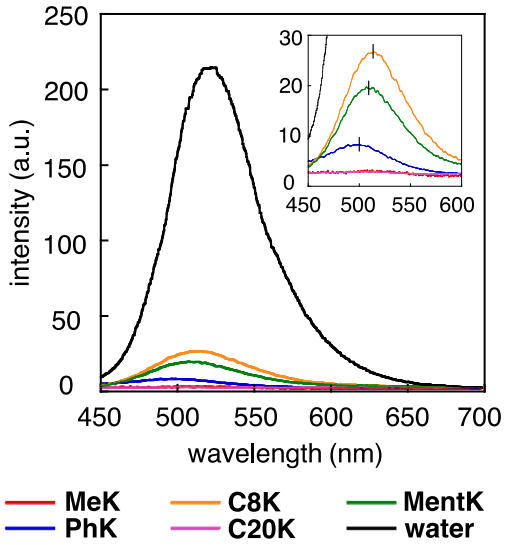

Figure 2-6. Fluorescence spectra of prodan loaded in various vesicles (λ_{ex} = 366 nm). The spectrum of prodan in 1.25% methanol in water (black line) is shown as a reference.

To probe the binding site for aromatic and aliphatic small molecules, the maximum loading capacity of naphthalene **1** ($\log P_{ow}$ = 3.36)[15] and *trans*-decalin **2** ($\log P_{ow}$ = 4.82)[11] was measured by the reported procedure[16], and the data are shown in Figure 2-7. The incorporation ratio of molecule per fullerene amphiphile was calculated from the amount of guest solubilized in the vesicle solution (determined by GC analysis), after consideration of the water solubility of the guest molecules. The **MeK** and **PhK** vesicles bind naphthalene

molecules better than *trans*-decalin. This preference does not reflect the logP_{ow} values, and suggests that the naphthalene binding occurs because of an aromatic–fullerene interaction, as it was found for the prodan binding. On the other hand, the **C8K** and **C20K** vesicles bind *trans*-decalin better than naphthalene, suggesting that the primary binding site is the alkyl chains.

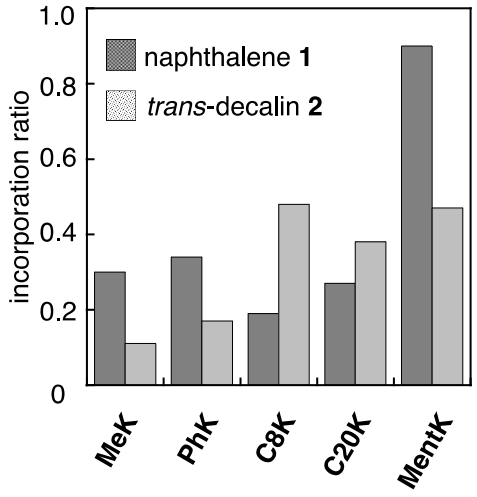

Figure 2-7. Loading of hydrophobic molecules in fullerene vesicles. Mole ratio of naphthalene **1** and *trans*-decalin **2** per fullerene amphiphile.

The loading profile of the **MentK** vesicle is very similar to those of **MeK** and **PhK**, and it is much larger, which we ascribe to the flexibility of this vesicle. The loading capacity of 0.9 naphthalene molecule/fullerene is remarkably higher than the reported loading capacity of cholesterol into lipid bilayer membranes (< 0.1 cholesterol molecule/lipid molecule) [17].

2.4 Selective binding of aromatic molecules in the fullerene membrane

The binding ability of the fullerene-rich interior of the fullerene membrane was further investigated with larger aromatic molecules of planar and three-dimensional structures, phenanthrene **3**, biphenyl **4** and *p*-terphenyl **5**. As for the smaller guests, there was little correlation between the loading amount and logP_{ow} indicating that the incorporation occurred not only by hydrophobic effect, but also fullerene-aromatic interactions. It is clear in Figure 2-8 that the loading of phenanthrene **3** (logP_{ow} = 4.49)[15] monotonically increased in the order **MeK**, **PhK**, **C8K**, **C20K**, and **MentK**. The loading of biphenyl **4** (logP_{ow} = 4.02)[18] also increased in the same order as **3**, but was far

smaller. The loading of *p*-terphenyl **5** ($\log P_{ow}$ = 5.51)[11] was the smallest of the three molecules. Therefore, the vesicles take up the planar phenanthrene molecule **3** very well but not bulky aromatic molecules. An attempted loading of pyrene, which is a planar molecule, resulted in precipitation of the vesicles suggesting strong interaction with the fullerene membrane. Note that control experiments indicated that a phosphatidyl choline vesicle is incapable of taking up these molecules under the same experimental conditions, supporting the unique molecular recognition property of fullerene vesicles. The lower stiffness of the lipid bilayer and the hydrophilic group exposed on the vesicle surface may have hindered the diffusion loading of the aromatic molecules to the alkyl interior of the membrane.[19]

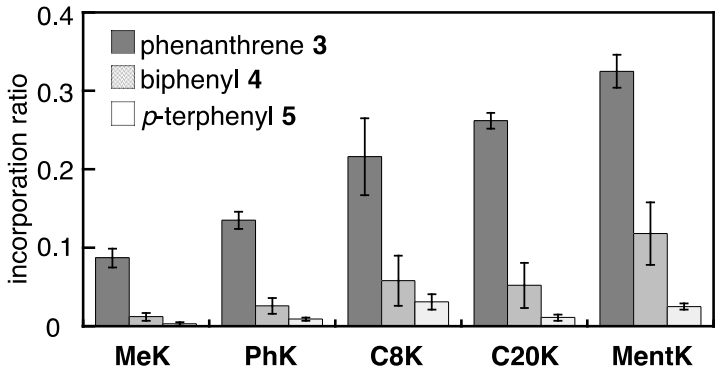

Figure 2-8. Loading of aromatic molecules in various vesicles. Mole ratio of phenanthrene **3**, biphenyl **4** and *p*-terphenyl **5** per fullerene amphiphile.

The effect of the binding of aromatic molecules to the vesicle structure was investigated by DLS and electron microscopy. The hydrodynamic diameter and size distribution of the vesicles are good indicators for the incorporation of extraneous molecules.[20] Upon the binding of aromatic molecules **3–5**, the diameter of the vesicles slightly changed (from –16 to +35%), without significant change to the size distribution (Figure 2-9a). Aggregates of the aromatic molecules were also not detected in the vesicle solution, strongly supporting the incorporation of the molecules in the fullerene membrane.

One may expect that the vesicle size would increase as the loading amount increases from **MeK** to **MentK** (e.g., phenanthrene **3**), but this was not the case (Figure 2-9b); the diameter increased from **MeK**, **PhK** to **MentK** except

for **C8K** and **C20K**. In the latter, the diameter increase is partially or entirely compensated by the collapse of the alkyl chains, so that the surface energy of the vesicle is minimized. Similarly, one would expect that loading of phenanthrene **3** would increase the size of the vesicles the most, followed by biphenyl **4** and terphenyl **5**. However, the loading of **3** caused as little change as that of **5** for all vesicles; that is, the bilayer loaded with a saturating amount of **3** remains rather compact. One possible reason could be that the planar aromatic molecule is π–sandwiched between the fullerene molecules and tightens the bilayer.

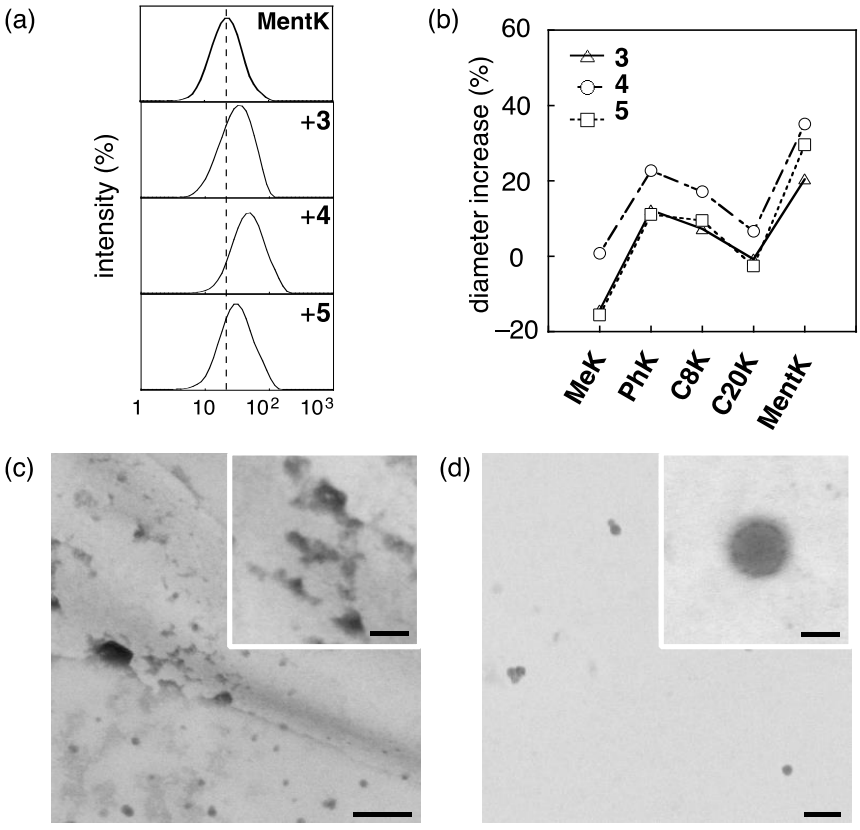

Figure 2-9. Effect of loading of aromatic molecules in the vesicle structure. (a) Size distribution of **MentK** vesicle upon loading of various molecules (data for other vesicles is shown in **Figure 2-12**). (b) Diameter change of the vesicle upon guest loading as measured by DLS. (c,d) STEM images of **MentK** and **C8K** vesicles after loading of **3** on an amorphous carbon film under 10^{-5} Pa. **MentK** collapses but **C8K** maintains the spherical structure. Scale bars are 100 nm and 20 nm for inset images.

The loading of aromatic molecules did not change too much the stability of the vesicles under vacuum. **MentK** vesicle loaded with **3** still collapsed on a carbon film and completely lost its spherical shape (Figure 2-9c). On the other

hand, **C8K** vesicle loaded with **3** maintained its spherical structure (Figure 2-9d). Note that in both samples, crystalline objects of **3** were not observed, supporting the incorporation of **3** in the vesicle membrane.

2.5 Conclusion

In conclusion, the fullerene bilayer made of $R_5C_{60}^-K^+$ binds an aromatic molecule primarily in its fullerene-rich interior and an aliphatic molecule in the exterior hydrophobic region if R bears a long alkyl chain. The fullerene interior preferentially binds a planar aromatic molecule over bulky molecules, and the molecular-loading capacity is much larger than for lipid vesicles. The present study revealed another unique feature of the fullerene vesicles in addition to the previously reported characteristics, such as robustness, water-tightness and the ability to display proteins on the surface[21].

The ability to design the hydrophobic spaces formed by bilayer membranes in water is a property exclusive to fullerene bilayer membranes. In chapter 3, I made use of this finding to control a polymerization reaction confined in the interior of the fullerene bilayer membrane.

2.6 Experimental Section

2.6.1 General

All reactions dealing with air- or moisture-sensitive compounds were carried out in a dry reaction vessel under nitrogen or argon. The water content of the solvent was confirmed with a Karl-Fischer Moisture Titrator (MKC-210, Kyoto Electronic Company) to be less than 100 ppm. Analytical thin-layer chromatography was performed on glass plates coated with 0.25 mm 230-600 mesh silica gel containing a fluorescent indicator (Merck). Gas-liquid chromatography (GLC) analysis was performed on a Shimadzu 14A or 14V machine equipped with glass capillary column HR-1 (0.25-nm i.d. 25 m) or CP-Chirasil-Dex CB (0.25-nm i.d. 25 m). Analysis with high pressure liquid chromatography (HPLC) was performed on JASCO HPLC system equipped with a BuckyPrep column (Nacalai Tesque Cosmosil® BuckyPrep, 4.6 x 250 mm; column temperature at 40 ^oC). Flash silica gel column chromatography was performed on silica gel 60N (Kanto, spherical and neutral, 140-325 mesh) as described by Still.[22] Gel permeation column chromatography was performed

on a Japan Analytical Industry LC-908 (eluent: chloroform) with JAIGEL 1H and 2H polystyrene columns. Melting points of solid materials were determined on a Mel-Temp capillary melting-point apparatus and were uncorrected. Infrared (IR) spectra were recorded on an ASI Applied Systems React IR1000 equipped with an attenuated total reflection (ATR) instrument or JASCO FT/IR-420 and are reported as wavenumbers (ν) in cm^{-1} with band intensities indicated as s (strong), m (medium), and w (weak). NMR spectra were measured on JEOL ECA-500 spectrometers and reported in parts per million from tetramethylsilane. ^{1}H NMR spectra in $CDCl_3$ were referenced internally to tetramethylsilane as a standard, and ^{13}C NMR spectra to the solvent resonance. Methyl, methylene, and methyne signals in ^{13}C NMR spectra were assigned by DEPT spectra. Routine mass spectra were acquired by atmospheric pressure ionization (APCI) using a quadrupole mass analyzer on Shimadzu QP-8000 or Waters ZQ-S spectrometer, and high resolution spectra by APCI or electrospray ionization (ESI) using a time-of-flight mass analyzer on JEOL JMS-T100LC (AccuTOF) spectrometer with a calibration standard of [60]fullerene. Distilled water was further deionized with Millipore Milli-Q. Dynamic laser light scattering (DLS) study was carried out on a Malvern Zetasizer Nano ZS machine. Atomic force microscopy (AFM) measurement was performed on a JEOL JSPM-4200 with a silicon cantilever (NSC-35, resonant frequency 120-190 kHz). Scanning transmission electron microscopy (STEM) observations were performed on a JEOL JEM-2100F at 294 K, with a spherical aberration coefficient Cs = 1.0 mm and acceleration voltage of 200 kV, under reduced pressure of 1.0×10^{-5} Pa in the sample column. The current density was ca. 0.5 pA cm^{-2}. The imaging instrument used was an ultrascan charge-coupled device (CCD) camera (512 × 512 pixels). The UV-Visible spectra were recorded on a JASCO V-570 UV/VIS/NIR Spectrophotometer. Fluorescence spectra were recorded on a HITACHI F-4500 Fluorescence Spectrophotometer.

2.6.2 Materials

Unless otherwise noted, materials were purchased from Tokyo Kasei Co., Aldrich Inc., and other commercial suppliers and used after appropriate purification before use. Anhydrous ethereal solvents (stabilizer-free) were

purchased from WAKO Pure Chemical and purified by a solvent purification system (GlassContour)[23] equipped with columns of activated alumina and supported copper catalyst (Q-5) prior to use. All other solvents were purified by distillation and stored over molecular sieves 4Å. Water enriched in ^{17}O (20.0–24.9 atom%) was purchased from Isotec and used as received. **MeK**, **PhK**, **C8K** and **C20K** were prepared by the reported procedures.[9,24]

2.6.3 Synthesis

1-Bromo-4-[(L-menthoxy)methyl]benzene

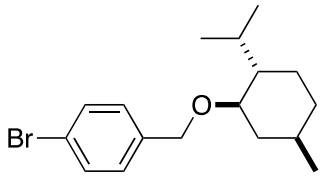

A dispersion of sodium hydride in mineral oil (2.48 g, 60%) was washed with 30 mL of dry hexane in a 300 mL three neck flask under nitrogen and dried under vacuum to yield sodium hydride as a white powder (1.52 g, 65.2 mmol). After redispersion of sodium hydride in 90 mL of THF, L-menthol (8.78 g, 56.2 mmol) in THF (45 mL) was added dropwise to the sodium hydride suspension for 10 min at 25 °C. After warming the reaction mixture to 50 °C, a solution of 4-bromobenzyl bromide (9.39 g, 37.5 mmol) in THF (25 mL) was added dropwise for 10 min. The reaction mixture was stirred for 1.5 h at reflux temperature and quenched into 50 mL of ice water. The crude was extracted in diethyl ether (100 mL × 3), dried over sodium sulfate and concentrated under reduced pressure. Purification was performed by column chromatography (silica gel) using hexane/ethyl acetate (95:5) as an eluent to give the product (10.1 g, 31.4 mmol, 83%) as a white crystal. Mp 53-54 °C; IR (KBr) 2950 (s), 2924 (s), 2866 (s), 1900 (m), 1782 (w), 1636 (m), 1591 (w), 1572 (w), 807 (s); ^1H NMR (500 MHz, $CDCl_3$) δ 0.71 (d, *J* = 6.9 Hz, 3H), 0.82-1.01 (m, 9H), 1.26-1.40 (m, 2H), 1.61-1.68 (m, 2H), 2.14-2.18 (m, 1H), 2.23-2.29 (m, 1H), 3.16 (dd, *J* = 4.6, 10.6 Hz, 1H), 4.34 (d, *J* = 11.5 Hz, 1H), 4.60 (d, *J* = 11.5 Hz, 1H), 7.21-7.23 (m, 2H), 7.44-7.64 (m, 2H); ^{13}C NMR (125 MHz, $CDCl_3$) δ 16.08, 20.99, 22.34, 23.24, 25.56, 34.53, 40.28, 48.30, 69.62, 78.97, 121.18, 129.40, 131.36, 138.21; anal. calcd for $C_{17}H_{25}BrO$: C, 62.77; H: 7.75; found: C, 62.58; H, 7.58.

6,9,12,15,18-Penta[4-(L-menthoxy)methylphenyl]-1,6,9,15,18-hexahydro(C_{60}-I_h)[5,6]fullerene (MentH)

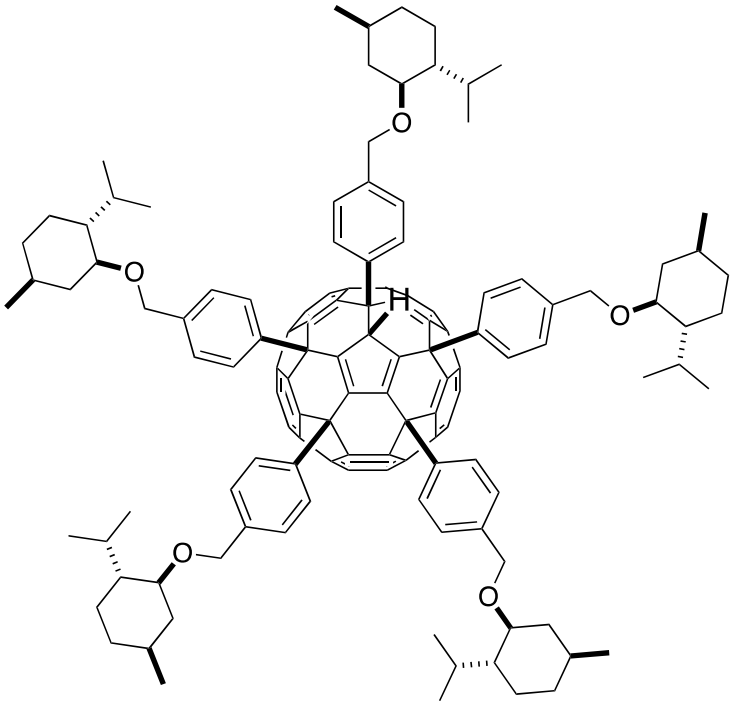

A solution of 4-[(L-menthoxy)methyl]phenylmagnesium bromide in THF (34.5 mL, 0.38 M, 13 mmol), was added to a suspension of CuBr・SMe_2 (2.77 g, 13.5 mmol) in THF (5 mL) and stirred for 10 min at 35 °C. [60]Fullerene (651 mg, 0.904 mmol) was dissolved in ODCB (40 mL) and added to the organocopper reagent suspension. The reaction mixture was stirred for 1.5 h at 40 °C and quenched with a saturated aqueous solution of ammonium chloride (5 mL). After removal of THF and Me_2S under reduced pressure, the reaction mixture was filtered through a pad of silica gel (eluent: hexane, then toluene). The obtained mixture was concentrated under reduced pressure, dissolved in diethyl ether, precipitated by gentle addition of an excessive amount of methanol and collected by filtration through a membrane filter (PTFE, pore size: 0.4 μm). The product was dried under vacuum to yield a red powder (1.75 g, 98%). IR (KBr) 2955 (s), 2922 (s), 2869 (s), 1894 (w), 1797 (w), 1714 (w), 1612 (w), 808 (m); ^{1}H NMR (500 MHz, $CDCl_3$) δ 0.67-0.73 (m, 15H), 0.87-0.98 (m, 45H), 1.25-1.36 (m, 10H), 1.58-1.66 (m, 10H), 2.16-2.29 (m, 10H), 3.13-3.20 (m, 5H), 4.35-4.38 (m, 2H), 4.42-4.44 (m, 2H), 4.56-4.58 (m, 2H), 4.62-4.64 (m, 2H), 4.68-4.70 (m, 2H), 5.22 (s, 1H), 7.11-7.12 (m, 2H), 7.17-7.18 (m, 4H), 7.30-7.32 (m, 4H), 7.34-7.36 (m, 2H), 7.54-7.57 (m, 4H), 7.73-7.75 (m, 4H); ^{13}C NMR (125 MHz, $CDCl_3$) δ 14.14, 16.17, 16.24, 16.30, 20.71, 21.02, 22.39, 22.42, 22.62, 22.66, 23.27,

23.38, 25.28, 25.29, 25.52, 25.60, 25.64, 25.66, 31.59, 34.20, 34.54, 34.58, 34.66, 40.27, 40.31, 40.34, 48.25, 48.32, 48.34, 69.85, 69.90, 78.76, 78.87, 78.89, 78.93, 78.99, 127.68, 127.86, 127.88, 127.98, 128.06, 128.13, 128.24, 128.30, 138.05, 138.44, 138.48, 138.66, 138.68, 138.79, 138.83, 143.10, 143.14, 143.69, 143.75, 144.02, 144.12, 144.22, 144.31, 144.33, 144.39, 144.44, 144.50, 144.75, 145.39, 145.44, 145.62, 145.68, 145.78, 145.86, 146.07, 146.25, 146.93, 147.11, 147.21, 147.74, 147.78, 147.88, 148.08, 148.24, 148.39, 148.67, 148.69, 148.74, 151.46, 151.60, 152.18, 152.18, 152.30, 152.60, 152.65, 156.09, 156.21; HRMS (APCI–) calcd for $C_{145}H_{125}O_5^-$ 1945.9527, found 1945.9480.

2.6.4 Methods

Preparation of fullerene vesicles

The vesicle solutions used for this study were prepared as reported.[10] As an example, **MentK** vesicles were prepared as follows. A solution of ^{t}BuOK in THF (1.00 M, 52 μL, 52 μmol, 1.5 equivalents) was added to a solution of **MentH** (68.1 mg, 35 μmol) in THF (2.8 mL) and the reaction mixture was stirred under argon for 3 h. A portion of the solution of **MentK** (12.5 mM, 0.80 mL, 10 μmol) was slowly injected into ultrapure water (4.2 mL) under stirring at 400 rpm over 1 min using a syringe pump (ISIS Co.) to obtain a vesicle solution of **MentK** (2.0 mM) in 16% THF/water. THF and water were removed by evaporation at ca. 7 kPa. The concentration of **MentK** was determined by UV absorption at 352 nm of wavelength and adjusted to 0.500 mM.

DLS analysis showed that the average diameter of a series of vesicles may vary in the range of 20 – 60 nm, depending on the conditions of the preparation, but generally falls in the range of 25–40 nm.

^{1}H NMR measurement of MentK vesicle

A solution of ^{t}BuOK in THF (1.0 M, 19 μL, 19 μmol) was added to a solution of **MentK** (24.4 mg, 12.5 μmol) in THF (1.0 mL) and the reaction mixture was stirred under nitrogen. After 3 h, a portion of the solution of **MentK** (12.5 mM, 0.8 mL, 10 μmol) was slowly injected into D_2O (4.2 mL) under stirring at 400 rpm over 1 min using a syringe pump (ISIS Co.) to obtain a vesicle solution of **MentK** (2.0 mM) in 16% THF/D_2O. THF was removed by evaporation at ca. 7 kPa. The concentration of **MentK** was determined by UV

absorption at 352 nm of wavelength and adjusted to 2.00 mM. The ^{1}H NMR of the D_2O solution of **MentK** vesicle was measured on JEOL ECA-500 at 20 °C.

Preparation of liposomes

The solution of lipid vesicles was prepared by a standard procedure.[25] Egg lecithin (132 mg, 0.180 mmol) was dissolved in $CHCl_3$/MeOH (1:1, 1.30 mL) and exposed to argon flow until an orange film was obtained. The film was then dried under reduced pressure overnight and hydrated by MilliQ (2.00 mL). In order to reduce the size of the particles, the solution was treated with a probe sonicator for one hour. The hydrodynamic diameter was determined as 197 ± 6 nm (DLS, Figure 2-10).

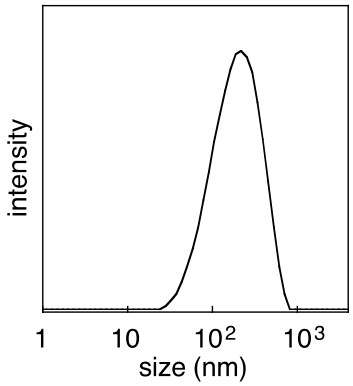

Figure 2-10. Size distribution of lipid vesicles prepared from phosphatidyl choline measured in water at 25 ºC by DLS.

DLS analysis

Dynamic light scattering (DLS) measurements were performed using a Malvern Zetasizer Nano ZS instrument equipped with a He–Ne laser operating at 4 mW power and 633 nm wavelength, and a computer-controlled correlator, at a 173° accumulation angle. Measurements were carried out in a polystyrene or glass cuvette. The sample was equilibrated for 5 min at the set temperature each time. The data were processed by Dispersion Technology software version 5.10 to give *Z*-average particle size and polydispersity index by cumulant analysis, and the particle size distribution by CONTIN analysis.

Determination of permeability coefficient by NMR relaxation time measurement.

The permeability coefficient (P) was determined by the NMR method established in the studies of lipid vesicles.[26] Aqueous solutions of $MnCl_2$ (0.50 mM, 200 μL) and the fullerene vesicles (200 μL) were mixed to give vesicle solutions containing 0.25 mM $MnCl_2$. The average hydrodynamic radius (R_h) of the vesicles was determined by DLS analysis, and the radius did not change (±13.2%) from 10 to 80 °C. Aqueous solutions of the fullerene vesicles in ^{17}O-enriched water were prepared in the same manner on a smaller scale using the same vesicle solutions (20 μL) and an aqueous solution of $MnCl_2$ (0.50 mM, 20 μL) in water containing 20 atom% of ^{17}O. The sample solution was transferred to a capillary NMR tube (Nihon Seimitsu Kagaku N-502B, tube diameter 2 mm). The NMR probe temperature was calibrated using methanol (10–30 °C) and ethylene glycol (40–80 °C) before the measurement.[27] The transverse relaxation time of the vesicle solution was measured from 10 °C to 80 °C in steps of 10 °C. The sample was equilibrated for 5 min at the set temperature each time, and the relaxation time was recorded three times at that temperature. The transverse relaxation time (T_2) of ^{17}O was recorded three times without spinning the sample tube. The transverse relaxation time of the interior water (T_{2i}) was measured, and, as a reference, the transverse relaxation time of blank water (T_{2ref}) was also measured at each temperature. The permeability coefficient (P) is obtained from Equation 2-1, where R is the radius of the vesicles obtained from the DLS analysis at each temperature.

$$P = \frac{R}{3}\left(\frac{1}{T_{2i}} - \frac{1}{T_{2ref}}\right) \quad \text{(Equation 2-1)}$$

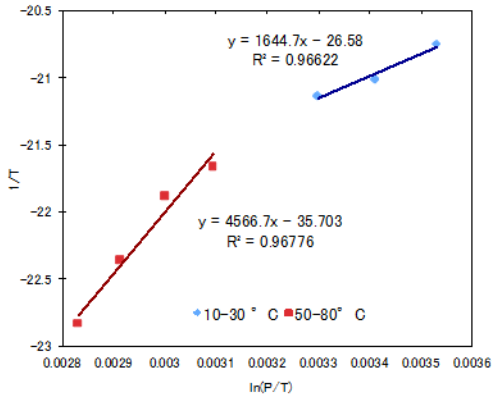

Figure 2-11. The Eyring plot [ln(P/T) vs. 1/T] of the permeability coefficients of **MentK** vesicles in water.

STEM measurement

STEM measurement was conducted on a JEOL JEM-2100F at 294 K with a spherical aberration coefficient Cs = 1.0 mm at an acceleration voltage of 200 kV under reduced pressure of 1.0×10^{-5} Pa in the sample column. The current density is ca. 0.5 pA cm^{-2}. The imaging instrument used was an ultrascan charge-coupled device (CCD) camera (512 × 512 pixels). 2 μL of **MentK** vesicle (1 μM) was deposited on a transmission electron microscopy (TEM) copper mesh coated with carbon film (Super Ultra High Resoluton Carbon film, thickness < 6 nm, Oken Shoji Co., Ltd.), then dried under reduced pressure (4×10^{-2} Pa) at room temperature for 18 h.

SEM measurement

SEM measurement was conducted on a FEI Magellan 400L. An aqueous solution of the vesicles (0.5 mM, 0.2 mL) was placed on an indium-tin oxide (ITO)/glass substrate, cleaned by UV/ozone treatment just before use, and spin-coated at 1500 rpm for 30 s. After drying under reduced pressure (5×10^{-2} Pa) for 10 min, the ITO substrate was subjected to SEM observation at an acceleration voltage of 1.5–2 kV under a vacuum of 5×10^{-5} Pa without any conductive coatings.

Loading of prodan in fullerene vesicles

Loading of prodan molecules in the bilayers was carried out as previously reported.[28] An aqueous solution of prodan (1.25 mL, 20 μM, 2.5% methanol) was added to an aqueous solution of $R_5C_{60}^-K^+$ (1.25 mL, 20 μM) and stirred for 12 hours. The sample was submitted for photoluminescence analysis (λ_{ex} = 366 nm).

Loading of aromatic molecules in fullerene vesicles

The aromatic compound (ca. 1 mg) was added to 2.00 mL of a 0.50 mM aqueous solution of fullerene vesicle. The suspension was vigorously stirred for 12 h and left to rest for 24 h. The remaining solid was removed by centrifugation (TOMY MC-150) of the supernatant at 5000 rpm for 30 min twice. 0.350 mL of the supernatant was collected and the aromatic compound was

extensively extracted from the vesicle solution with dichloromethane. The amount of aromatic molecule was determined by UV absorption at the wavelength of 250 nm for biphenyl, 283 nm for *p*-terphenyl, and 295 nm for phenanthrene. *Trans*-decalin was loaded by a similar procedure: *trans*-decalin (100 μL) was added to 4.50 mL of a 0.50 mM aqueous solution of fullerene vesicle. The mixture was stirred overnight for 12 h and left to rest for 24 h, which resulted in complete phase separation of the aqueous and organic layers. 0.500 mL of the aqueous phase was collected and *trans*-decalin was extracted from the vesicle solution with hexane. The amount of naphthalene and *trans*-decalin was determined by GC using *n*-dodecane as an internal standard. The number of molecules incorporated per fullerene monomer was calculated after consideration of the amount of compound solubilized in water, which was determined by an experiment carried out in parallel to the main experiment.

Table 2-1. Ratio of hydrophobic molecules incorporated per fullerene monomer.

vesicle	incorporation ratio	
	naphthalene **1**	*trans*-decalin **2**
MeK	0.30	0.11
PhK	0.34	0.17
C8K	0.19	0.48
C20K	0.27	0.38
MentK	0.90	0.47

Table 2-2. Ratio of aromatic molecules incorporated per fullerene monomer (or lipid molecule).

vesicle	incorporation ratio		
	phenanthrene **3**	biphenyl **4**	*p*-terphenyl **5**
MeK	0.09 ± 0.01	0.012 ± 0.005	0.003 ± 0.002
PhK	0.13 ± 0.01	0.03 ± 0.01	0.009 ± 0.002
C8K	0.22 ± 0.05	0.06 ± 0.03	0.03 ± 0.01
C20K	0.26 ± 0.01	0.05 ± 0.03	0.011 ± 0.004
MentK	0.32 ± 0.02	0.12 ± 0.04	0.025 ± 0.004
Reference (liposome)	0.003 ± 0.002	0.0020 ± 0.0009	–0.002 ± 0.005

Table 2-3. Change of the hydrodynamic diameter (%) of the vesicles after incorporation of aromatic molecules. Determined in water at 25 ºC by DLS.

vesicle	size increase (%)		
	phenanthrene	biphenyl	*p*-terphenyl
MeK	–14.30 ± 0.04	1 ± 3	–15.60 ± 0.03
PhK	12.25 ± 0.05	22.7 ± 0.1	11.1 ± 0.1
C8K	7.3 ± 0.4	17.2 ± 0.2	9.4 ± 0.3
C20K	–1 ± 2	6.6 ± 0.2	–2.6 ± 0.6
MentK	20.50 ± 0.06	35.10 ± 0.04	29.57 ±0.07

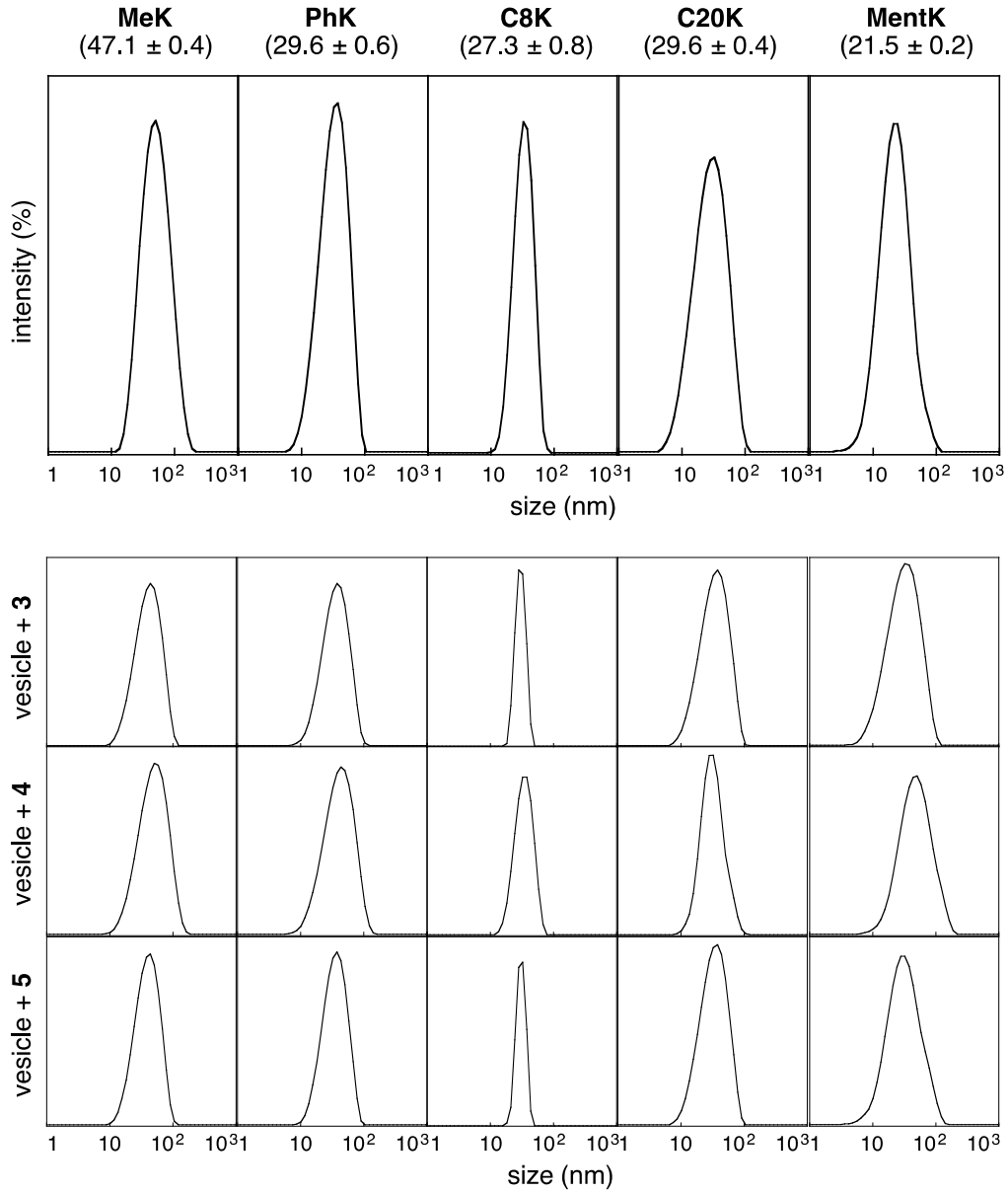

Figure 2-12. Size distribution of fullerene vesicles (top) before and (bottom) after loading of aromatic molecules determined in water at 25 ºC by DLS. The hydrodynamic diameter of the vesicles is shown inside the parenthesis. Error shows the standard deviation of the mean from three measurements.

2.7 References

[1] *Vesicles*, ed. by M. Rosoff, Marcel Dekker, New York, 1996.

[2] Nagle, J. F. & Tristram-Nagle, S. Structure of lipid bilayers. *Biochim. Biophys. Acta.* **1469**, 159–195 (2000).

[3] Voskuhl, J. & Ravoo, B. J. Molecular recognition of bilayer vesicles. *Chem. Soc. Rev.* **38**, 495–505 (2009).

[4] Doval, D. A., Areephong, J., Bang, E.-K., Bertone, L., Charbonnaz, P., Fin, A., Lin, N.-T., Lista, M., Matile, S., Montenegro, J., Orentas, E., Sakai, N., Tran, D.-H. & Jentzsch, A. V. Recent progress with functional biosupramolecular systems. *Langmuir* **27**, 9696–9705 (2011).

[5] Sawamura, M., Nagahama, N., Toganoh, M., Hackler, U. E., Isobe, H., Nakamura, E., Zhou, S. Q. & Chu, B. Pentaorgano[60]fullerene $R_5C_{60}^-$. A water soluble hydrocarbon anion. *Chem. Lett.* **29**, 1098–1099 (2000).

[6] Zhou, S., Burger, C., Chu, B., Sawamura, M., Nagahama, N., Toganoh, M., Hackler, U. E., Isobe, H. & Nakamura, E. Spherical bilayer vesicles of fullerene based surfactants in water: a laser light scattering study. *Science* **291**, 1944–1947 (2001).

[7] Isobe, H., Homma, T. & Nakamura, E. Energetics of water permeation through fullerene membrane. *Proc. Natl. Acad. Sci. U.S.A.* **104**, 14895–14898 (2007).

[8] Homma, T., Harano, K., Isobe, H. & Nakamura, E. Nanometer-sized fluorous fullerene vesicles in water and on solid surfaces. *Angew. Chem. Int. Ed.* **49**, 1665–1668 (2010).

[9] Homma, T., Harano, K., Isobe, H. & Nakamura, E. Preparation and properties of Vesicles made of nonpolar/polar/nonpolar fullerene amphiphiles. *J. Am. Chem. Soc.* **133**, 6364–6370 (2011).

[10] Burger, C., Hao, J., Ying, Q., Isobe, H., Sawamura, M., Nakamura, E. & Chu, B. Multi-layer vesicles and vesicle clusters formed by fullerene-based surfactant $C_{60}(CH_3)_5K$. *J. Colloid Interface Sci.* **275**, 632–641 (2004).

[11] Calculated using Advanced Chemistry Development (ACD/Labs) Software V11.02 (© 1994–2013 ACD/Labs).

[12] Junquera, E., del Burgo, P., Boskovic, J. & Aicart, E. Self-organization of the ternary didecyldimethylammonium bromide/octyl-β-*D*-glucopyranoside/water system. *Langmuir* **21**, 7143–7152 (2005).

[13] Matsuo, Y., Morita, K. & Nakamura, E. Penta(pyrenyl)[60]fullerenes: pyrene-pyrene and [60]fullerene-pyrene interactions in the crystal and in solution. *Chem. – Asian J.* **3**, 1350–1357 (2008).

[14] Artukhov, V. Y., Zharkova, O. M. & Morozova, J. P. Features of absorption and fluorescence spectra of prodan. *Spectrochim. Acta A* **68**, 36–42 (2007).

[15] Brown, R. S., Akhtar, P., Åkerman, J., Hampel, L., Kozin, I. S., Villerius, L. A. & H. Klamer, J. C. Partition controlled delivery of hydrophobic substances in toxicity tests using poly(dimethylsiloxane) (PDMS) films *Environ. Sci. Technol.* **35**, 4097–4102 (2001).

[16] Polak, J. & Lu, B. C. Mutual solubilities of hydrocarbons and water at 0 and 25 °C *Can. J. Chem.* **51**, 4018–4023 (1973).

[17] Lee, S.-M., Chen, H., Dettmer, C. M., O'Halloran, T. V. & Nguyen, S. T. Polymer-caged lipsomes: A pH-responsive delivery system with high stability *J. Am. Chem. Soc.* **129**, 15096–15097 (2007).

[18] Lodge, K. B. & Egyepong, E. J. Evidence for self-association of nonionic and other organic solutes in liquid phases comprising 1-octanol and water. *J. Phys. Chem. A*, **114**, 5132–5140 (2010).

[19] Kim, M. D., Dergunov, S. A., Richter, A. G., Durbin, J., Shakov, S. N., Jia, Y., Kenbeilova, S., Orazbekuly, Y., Kengpeiil, A., Lindner, E., Pingali, S. V., Urban, V. S., Weigand, S. & Pinkhassik, E. Facile directed assembly of hollow polymer nanocapsules within spontenously formed catanionic surfactant vesicles. *Langmuir* **30**, 7061–7069 (2013).

[20] Harano, K., Yamada, J., Mizuno, S. & Nakamura, E. High-density display of protein ligands on self-assembled capsules via noncovalent fluorous interactions. *Chem. Asian. J.* in press (2014). DOI: 10.1002/asia.201403144.

[21] Harano, K., Minami, K., Noiri, E., Okamoto, K. & Nakamura, E. Protein-coated nanocapsules via multilevel surface modification. Controlled preparation and microscopic analysis at nanometer resolution. *Chem. Commun.* **49**, 3525–3527 (2013).

[22] Still, W. C., Kahn, M. & Mitra, A. Rapid chromatographic technique for preparative separations with moderate resolution. *J. Org. Chem.* **43**, 2923–2925 (1978).

[23] Pangborn, A. B., Giardello, M. A., Grubbs, R. H., Rosen, R. K. & Timmers, F. J. Safe and convenient procedure for solvent purification. *Organometallics* **15**, 1518–1520 (1996).

[24] Sawamura, M., Iikura, H. & Nakamura, E. The first pentahaptofullerene metal complexes. *J. Am. Chem. Soc.* **118**, 12850–12851 (1996).

[25] Szoka Jr., F. Compartive properties and methods of preparation of lipid vesicles (liposomes). *Ann. Rev. Biophys. Bioeng.* **9**, 467–508 (1980).

[26] Haran, N. & Shporer, M. Study of water permeability through phospholipid vesicle membranes by ^{17}O NMR. *Biochim. Biophys. Acta* **426**, 638–646 (1976). Shchori, E., Jagur-Grodzinski, J., Luz, Z. & Shporer, M. Kinetics of complexation of macrocyclic polyethers with alkali metal ions. I. Sodium-23 nuclear magnetic resonance of sodium dibenzo-18-crown-6 in N,N-dimethylformamide. *J. Am. Chem. Soc.* **93**, 7133–7138 (1971).

[27] Raiford, D. S., Fisk, C. L. & Becker, E. D. Calibration of methanol and ethylene glycol nuclear magnetic resonance thermometers. *Anal. Chem.* **51**, 2050–2051 (1979).

[28] Barnejee, A., Sengupta, B., Chaudhuri, S., Basu, K. & Sengupta, P. K. Encapsulation of Prodan in beta-cyclodextrin environments: A critical study via electronic spectroscopy and molecular mechanics. *J. Mol. Struc.* **794**, 181–189 (2006).

— Chapter 3 —
Polymer growth in nm-thick fullerene bilayer membranes

3.1 Introduction: Confinement of polymerization reaction in bilayer membranes

Living cells have mastered the chemistry in bilayer membranes, where a complex system of lipid molecules and transmembrane proteins regulates the transport of substances and reactions in the membrane for maintenance of life.[1,2] Interest in biological and material applications have motivated scientists to develop the chemistry of bilayer membranes in a flask; however, some topics were particularly challenging. For instance, attempts to utilize lipid membranes for the control of polymerization have seen only partial success because of the structural instability of the lipid bilayer. In most of the reports, the polymer phase separates from the membrane during polymer growth, creating large nodules on the vesicle surface, the so-called parachute structure.[3,4,5] In a few examples, the reaction could be confined inside the membrane, but the structure of the polymeric objects obtained was not uniform, because of the intrinsic properties of lipid vesicles.[6,7,8,9,10,11] Up to date, only catalyst-free radical polymerization of styrene and methacrylate derivatives have been reported, probably due to the limitation of the lipid membrane in incorporating large catalyst molecules. On the other hand, high control of polymerization reactions has been demonstrated in more robust assemblies, such as porous coordination polymers.[12]

In contrast to a lipid membrane that is a fluidic liquid crystal whose structural integrity is maintained largely by a hydrophobic interaction[13,14], the fullerene bilayer made of $(R\text{-}C_6H_4)_5C_{60}^{-}K^{+}$ amphiphiles (R = $^{n}C_8H_{17}$, $^{n}C_{20}H_{41}$, $^{n}C_8F_{17}$, Figure 3-1a)[15,16,17] is a structurally robust liquid crystal. The fullerene vesicle has a ternary architecture where the fullerene core is located in the interior, the (perfluoro)alkyl groups are exposed to an aqueous environment, and the anionic part is located in the middle. As a result, the fullerene bilayer gains its stability from mutually orthogonal forces, π–π and hydrophobic (or fluorous) interactions, and creates three regions in water: fullerene-rich core, (perfluoro)alkyl-rich interior and exterior. Inspired by the results in chapter 2, I thought of the fullerene membrane as a prospective environment for polymerization reactions, which can be tuned by the R substituent group on fullerene.

In this chapter, the control of the morphology of polymeric objects

prepared in fullerene vesicles is described. Ring-opening metathesis polymerization (ROMP) of a norbornene dicarboxylate ester (**1a**) in the membrane of fullerene vesicles produces a polyester **2a** of the same molecular weight but in two different nm-scale morphologies, a capsule or a particle, depending on the R group on the surface of the vesicle template (Figure 3-1b). The different location of the polymer chains in the bilayer, determined by fluorescence probe, water permeation and electron microscopic studies of the vesicle/polymer composites, was found to be the origin of the different morphologies of the polymeric objects.

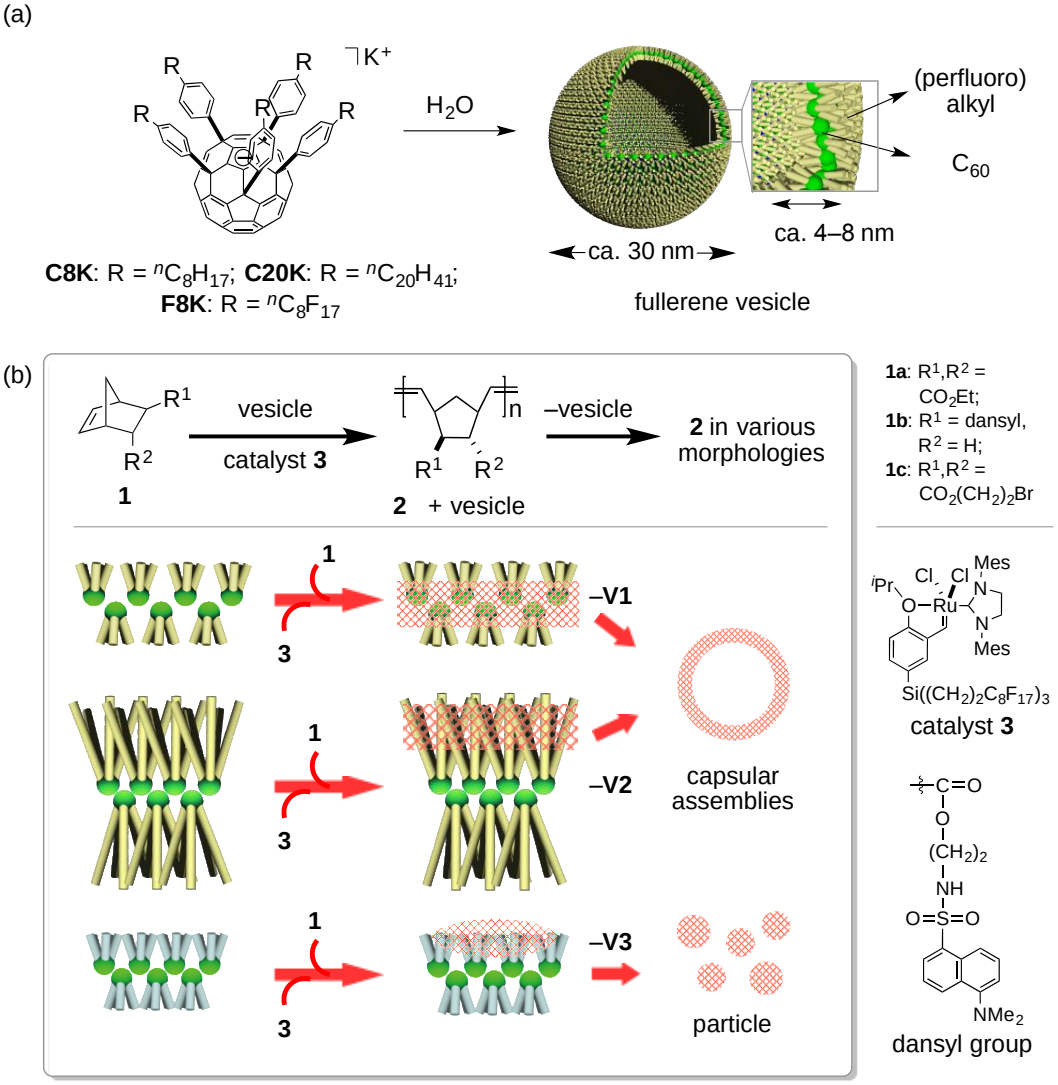

Figure 3-1. Control of polymer growth in fullerene bilayer membranes. (a) The bilayer vesicles made of fullerene amphiphiles, **C8K**, **C20K**, and **F8K**. (b) ROMP of **1a–c** with a Hoveyda–Grubbs-type catalyst **3** loaded in a fullerene bilayer. The bilayer consists of three regions, fullerene-rich core, (perfluoro)alkyl-rich interior and surface, and polymerization in the membrane produces a capsule and a particle after removal of the vesicles using methylene chloride extraction. Note that in the absence of vesicles, the same reaction produces ill-defined structures.

3.2 Catalyst loading in fullerene membranes

In this study, ROMP was investigated as the polymerization reaction because it is known to be tolerant to harsh conditions and compatible to many functional groups.[18] ROMP of hydrophobic norbornene derivative **1a** (water solubility of ca. 14.9 mM)[19] on fullerene vesicles catalyzed by a Hoveyda–Grubbs catalyst bearing a tris[(perfluorooctyl)ethyl]silyl group **3**[20,21], which was loaded on the vesicles formed by spontaneous self-assembly of the fullerene amphiphiles in water (0.30 mM)[22], was chosen as a model reaction. The catalyst loading was achieved by addition of a dichloromethane solution of **3** (0.50 mM) to the aqueous solution of vesicles, followed by removal of the organic solvent. The diameter of the pristine vesicle was 27–31 nm and unimodal (dynamic light scattering (DLS), Figure 3-2a), and increased by 10–17% upon catalyst loading (ca. 200 catalyst molecules/vesicle; 2 mol% for monomer **1a**). The size distribution obtained by DLS also indicated the absence of either catalyst monomers or aggregates in solution, as observed in the case of incomplete catalyst incorporation in a vesicle without alkyl chains on the surface, **PhK** (R = H, Figure 3-2a).

Loading of the catalyst molecules in the fullerene membranes was further supported by electron microscopy studies. The vesicle impregnated with the catalyst was placed on a thin carbon film and imaged simultaneously by SEM and STEM. Catalyst aggregates, which were observed in a sample of **PhK** (Figure 3-13), were found nowhere. Upon catalyst loading, vesicles of **C8K** and **C20K** maintained their spherical shape and smooth surface, suggesting the catalyst molecules were uniformly distribute in the membrane (Figure 3-2b,c). Interestingly, the catalyst molecules loaded on the fluorous vesicle **F8K** are phase-segregated in the fluorous interior and seen as bulges on the surface (3.4 ± 0.6 nm in diameter; Figure 3-2d) when analyzed using a low-landing voltage scanning electron microscope (SEM)[23]. The bulges are seen as dark spots upon scanning transmission electron microscopy (STEM) analysis of the same sample (Figure 3-2e). Thus, these bulges were assigned as aggregates of the catalyst, which were formed by phase segregation in the fluorous fullerene bilayer as illustrated in Figure 3-2f. An EDX signal due to the ruthenium atoms was not detected since the concentration (ca. 200 Ru atoms/vesicle) was below the detection limit.

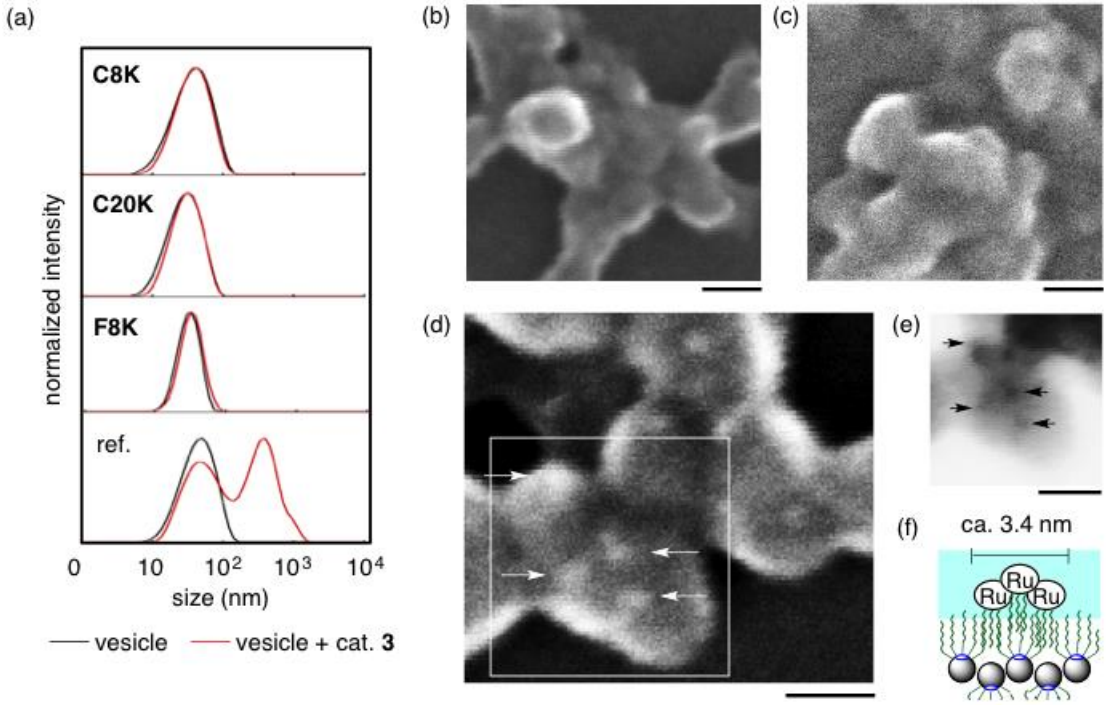

Figure 3-2. Loading of the catalyst **3** on the vesicles. (a) Size distribution of fullerene vesicles before (black line) and after (red line) loading of catalyst **3** measured by DLS at 25 ºC. **PhK** (R = H) is given as a reference of vesicle without any alkyl substituent on the surface. (b, c) SEM images of **C8K** and **C20K** impregnated with the catalyst **3**. (d,e) SEM and STEM images of **F8K** impregnated with **3**. Black arrows indicate bulges caused by aggregates of **3**, which are seen as black dots in the STEM image. (f) Schematic image of a catalyst bulge on the **F8K** membrane. The number of ruthenium atoms was too small to identify them by energy dispersive X-ray analysis (EDX). The scale bars are 20 nm.

3.3 Ring-opening metathesis polymerization (ROMP) in fullerene bilayers

Monomer **1a** was loaded to the catalyst-loaded vesicles in a monomer/fullerene ratio of five and monomer/catalyst ratio of fifty. The polymerization of **1a** catalyzed by **3** (2 mol% to monomer) on the vesicle was extremely slow at room temperature but rapid at 60°C for 2 h with >97% conversion (determined by ^{1}H NMR). This observation stands in contrast to the fact that the reaction in a homogenous organic medium or in water without vesicles occurs rapidly at room temperature, and supports the expected low fluidity of the interior of the bilayer.[24]

After the reaction, the hydrodynamic diameter of the vesicles increased 15–31% without significant change to the size distribution (DLS, Figure 3-3a,b). Note that aggregates of polymers that could have been dissociated from the

fullerene membrane were not detected, strongly supporting that the polymer chains were formed in the fullerene membrane.

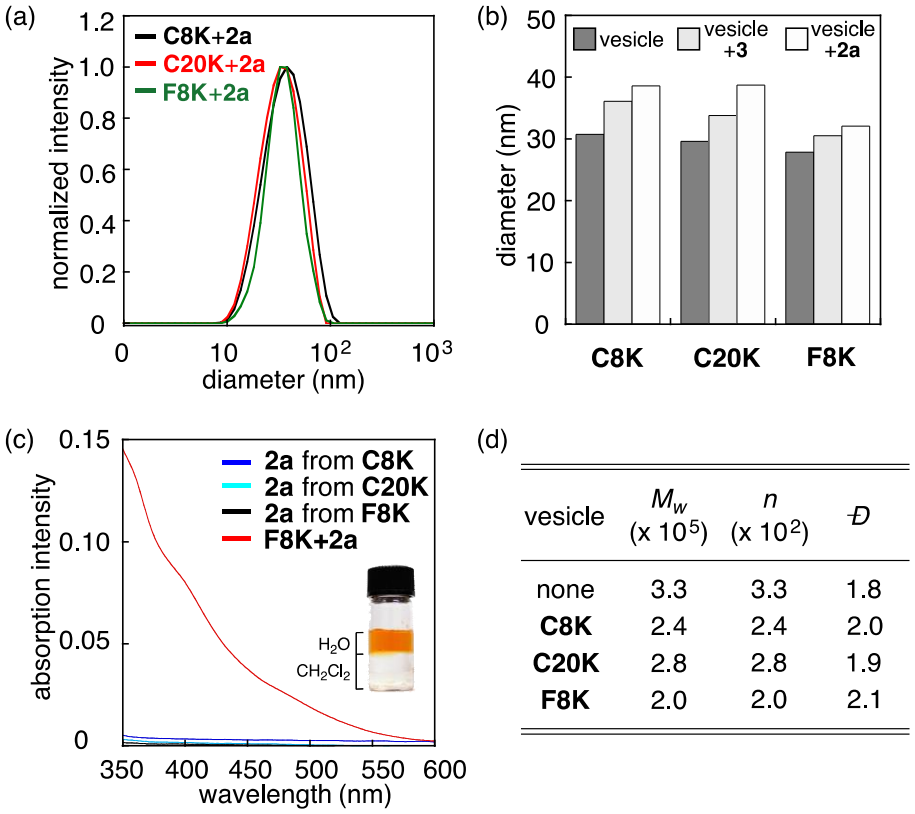

vesicle	M_w (x 10^5)	n (x 10^2)	$Đ$
none	3.3	3.3	1.8
C8K	2.4	2.4	2.0
C20K	2.8	2.8	1.9
F8K	2.0	2.0	2.1

Figure 3-3. ROMP in fullerene membranes. (a,b) Size distribution and hydrodynamic diameter of vesicles after polymerization of **1a** determined by DLS in water at 25 ºC. (c) UV absorption spectra of polymer **2a** after removal of fullerene vesicles by dichloromethane extraction, as shown by the lack in absorption at longer wavelengths. Absorption spectrum in water of **F8K+2a** prior extraction is given as a reference. (d) Molecular weight of polymer **2a** obtained from vesicles was measured in THF at 40 ºC by GPC. A polymer prepared under the same conditions in water without vesicles was investigated as a reference.

The molecular weights, M_w, of the polymer extracted from the reaction mixture with methylene chloride (UV analysis indicated the absence of the fullerene ($R_5C_{60}^-K^+$, which is anionic) in the polymer extract, Figure 3-3c) were 2.42×10^5 (polydispersity index ($Đ$) = 1.98), 2.80×10^5 (1.87) and 2.04×10^5 (2.11) g mol^{-1} for **C8K**, **C20K** and **F8K**, respectively. The molecular weight of a reference polymer obtained in water without the vesicle showed a similar value of 3.33×10^5 (1.83) g mol^{-1}. The similarity in the molecular weight and dispersity indicates that the reaction environment did not affect much the nature of the polymerization. Given the monomer/fullerene ratio of five and the average

number of vesicles in the solution (6–10 × 10^{16} L^{-1}), it was estimated that each vesicle contains ca. 20–30 polymer chains. The sluggish reaction and a relatively high molecular weight of the polymer suggests that only a small portion of the catalyst (ca. 10%) was active even at 60 °C.

3.4 Location of the polymer chains in the fullerene bilayer determined by a fluorescence probe and water permeation profile

Fluorescence quenching and shift measurements for fluorescent dyes loaded in vesicles provide information on their location in the fullerene bilayer.[25,26,27] I thus copolymerized **1a** and a dansyl ester **1b** (95:5) in catalyst-loaded vesicles (Figure 3-4a), and compared the fluorescence intensity of the resulting vesicle/polymer composite. As summarized in Figure 3-4b, the fluorescence of the copolymer in **C8K** vesicle (black line) was quenched by the fullerene molecule, while the copolymer in the fluorous vesicle **F8K** (blue) was much less, and the copolymer in **C20K** (green) was the least. Furthermore, a red shift of the fluorescence maximum (λ_{max}) of the dansyl dye toward λ_{max} of 550 nm for the monomer **1b** in water (orange) is a measure of the hydrophilicity of the environment. The λ_{max} value of 471 nm for the copolymer in **F8K** (cf. 445 nm for monomer **1b** in perfluorohexane, Figure 3-4c) moved to 525 nm for the copolymer in **C20K** (cf. 519 nm in methanol). Therefore, ROMP in **C8K**, which bears shorter alkyl chains, occurred in the fullerene core region, while ROMP in **C20K** occurred in the $C_{20}H_{41}$-chain region and in **F8K** occurred in the fluorous region.

After extraction of copolymer **2b** in dichloromethane, the fluorescence maximum shifted to 502 nm for all three cases (Figure 3-4d), confirming that the fluorescence shifts of dansyl observed in the vesicles in water was originated from the different locations of the copolymer chains in the bilayers.

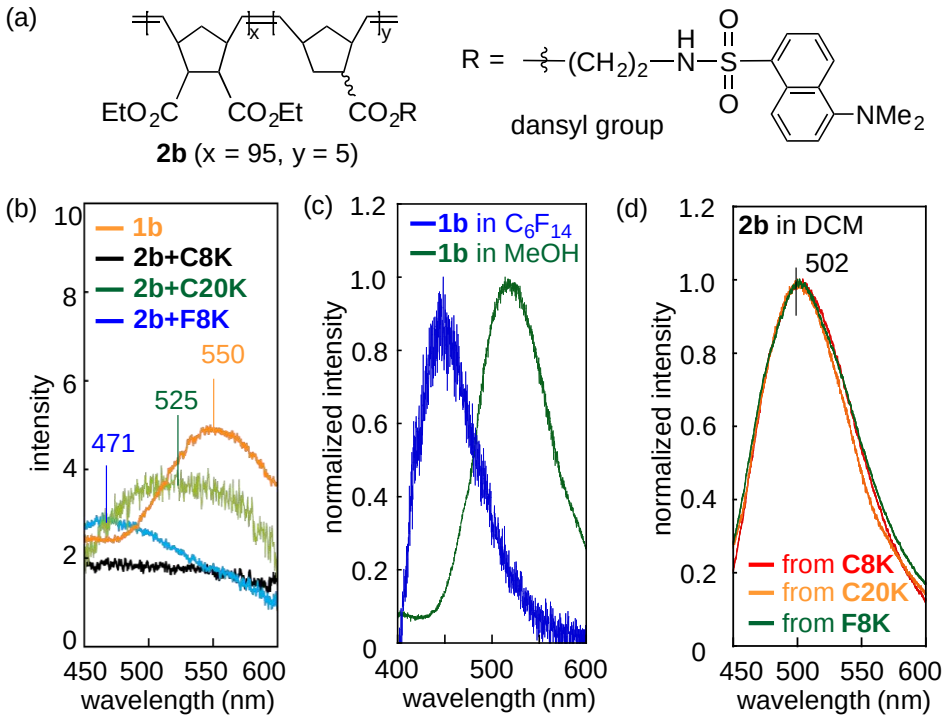

Figure 3-4. Investigation of the location of polymer chains in the vesicle membrane via a solvatochromic probe, dansyl amide. (a) Chemical structure of copolymer **2b** that contains dansyl. (b) Fluorescence spectrum (λ_{ex} = 350 nm) of the dansyl group in different environments: **2b** in **C8K** (black line), **2b** in **C20K** (green), **2b** in **F8K** (blue) and the monomer **1b** in water (orange). The concentration of the dansyl group is 1.0 μM. (c) Fluorescence spectrum of monomer **1b** in perfluorohexane (blue line) and methanol (green). (d) Fluorescence spectrum of **2b** after removal of vesicles by dichloromethane extraction.

Water permeation through a fullerene bilayer is a unique process because the permeation barrier originates from water–fullerene interactions and is controlled by an entropy term, unlike an aliphatic lipid bilayer whose permeation is controlled largely by the enthalpy term because the permeation is limited by liquid-to-gas phase change in the hydrocarbon interior (Figure 3-5a). The water permeation was measured by ^{17}O NMR experiments, as previously reported.[28] The polymerization on the vesicle increased water permeation through the fullerene bilayer as much as 12 times (e.g., for **C8K** vesicle at 80°C; Figure 3-5b), and affected the permeation kinetics in each vesicle differently.

Kinetics of water permeation provided structural information on the interior of the bilayer containing polymer **2a**. As shown in Figure 3-5c, column **C8K+2a**, polymerization on vesicle **C8K** entirely changed the kinetic profile: The entropy loss ($-T\Delta S^{\ddagger}$) decreased from 47.1 to 22.1 kJ/mol while the enthalpy

cost ($\Delta H^{\ddagger}$) increased from 3.0 to 24.0 kJ/mol. This value of enthalpy cost is very similar to the one reported for a phosphatidylcholine bilayer (column **liposome**)[29]. Therefore, the permeation is controlled equally by the entropy and the enthalpy terms, that is, equally by the properties of the fullerene and the aliphatic side chains. I considered that the polymer chains were located in the fullerene-core region and disrupted fullerene-fullerene interactions (cf. Figure 3-1), because the octyl chains are too short to accommodate the polymer chains alone.

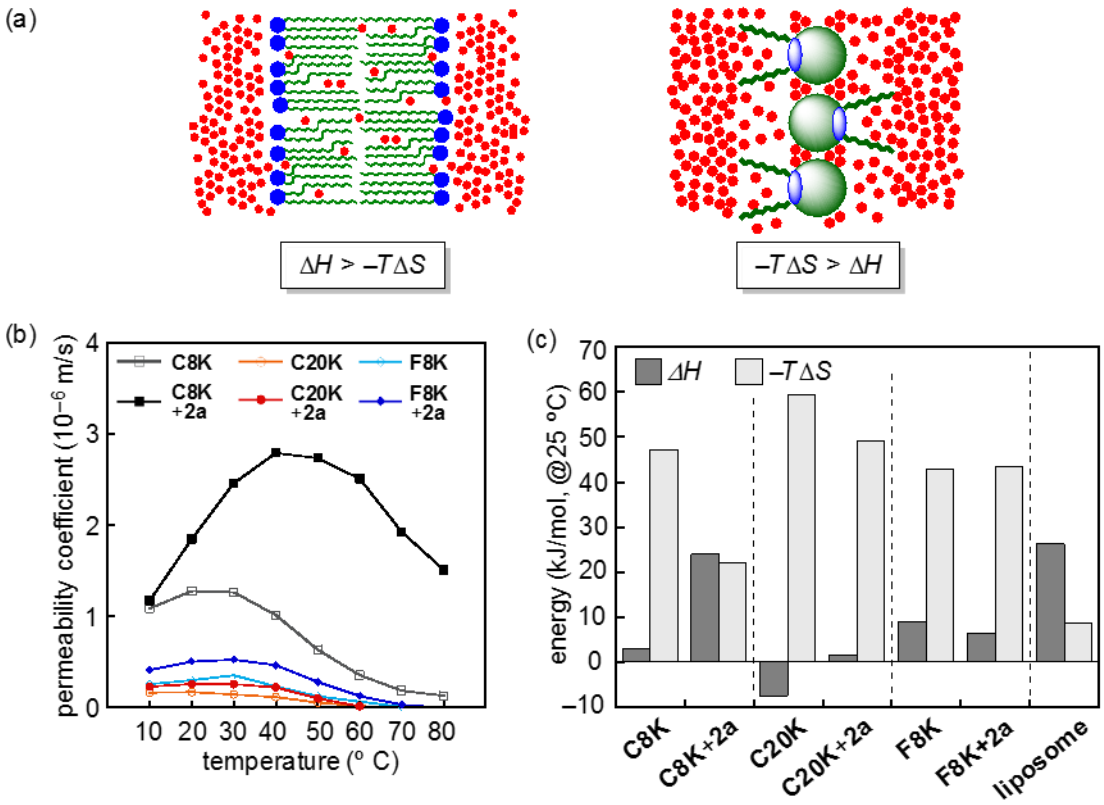

Figure 3-5. Investigation of the polymer location in the vesicle membrane via water permeation through fullerene membranes before and after polymerization measured by ^{17}O NMR experiments. (a) Schematic image of water permeation through lipid and fullerene bilayers. (b) Temperature dependence of the water permeability coefficient. (c) Activation enthalpy ($\Delta H^{\ddagger}$) and activation entropy ($-T\Delta S^{\ddagger}$) values for water permeation at 25 °C. Data for pristine vesicles were taken from ref. 28. Data for a liposome made of a phosphatidylcholine bilayer were taken from ref. 29.

As shown in column **C20K+2a**, polymerization on **C20K** vesicle did not much affect the kinetic profile. The entropy loss ($-T\Delta S^{\ddagger}$) decreased from 59.5 to 49.2 kJ/mol while the enthalpy cost ($\Delta H^{\ddagger}$) increased from –7.5 to 1.5 kJ/mol. As

shown in columns **F8K** and **F8K+2a**, polymerization change little the kinetics of the fluorous vesicle. The entropic term for **C20K** and **F8K** continues to dominate after polymerization, indicating that the polymer is located not in the fullerene core but in the periphery of the bilayer—a conclusion fully consistent with the fluorescence quenching.

3.5 Morphology of fullerene vesicles containing polymers chains observed by electron microscopy

Further investigation of the vesicles by electron microscopy provided preliminary information on how the different locations of the polymerization reaction in the fullerene membrane affected the polymer morphology.

The vesicle containing the polymer was placed on an indium zinc oxide (IZO) on glass and imaged as such with a high-resolution SEM using an electron beam current of 3.1–6.3 pA and beam landing voltage of 200 V (Figure 3-6). This analytical method was recently shown to be a powerful approach for analysis of the surface morphology of organic molecular assemblies including nm-sized proteins,[30] and IZO that has a very smooth surface was found to be suitable for the present purpose. The SEM images of the polymer-containing vesicles (e.g., vesicle **C8K+2a**) on IZO revealed an intriguing surface morphology. The vesicles **C8K** and **C20K** containing the polymer **2a** were spherical and their surface was smooth (Figure 3-6a,c,d). The vesicle **F8K+2a** was also spherical but its surface had many bulges (Figure 3-6b,e). Taken together with the propensity of the catalyst **3** to phase-segregate on the fluorous surface of the **F8K** vesicle and the estimated numbers of polymer **2a** on a vesicle (vide supra), I consider that each bulge represents a small nodule of one or a few polymer chains formed on an individual catalyst molecule(s).

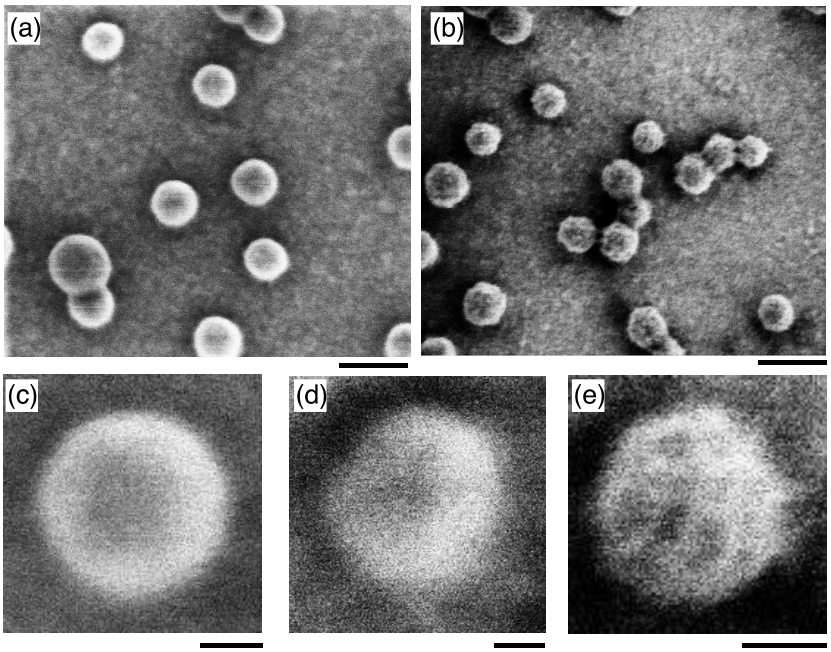

Figure 3-6. SEM images of **2a** on vesicles (a,c) **C8K**, (d) **C20K** and (b,e) **F8K**. Images were recorded on an IZO (indium-zinc oxide)/glass substrate at a landing voltage of 200 V under 10^{-5} Pa. The imaging under these conditions does not require the conventional metal coating of the sample. The scale bars are (a,b) 50 nm or (c,d,e) 10 nm.

The morphology of the composites observed by SEM was further supported by transmission electron microscopic images obtained on a thin carbon film (Figure 3-7). The polymer chains in alkylated membranes, **C8K** and **C20K**, enhanced the contrast of the vesicle shell, which usually cannot be observed because of the inner water content of the vesicles that do not leak under these conditions[31]. The composite was as thick as ca. 6 nm for **C8K** (membrane thickness of 4 nm) and ca. 4 nm for **C20K** (membrane thickness of 8 nm). The shell observed for **C20K** and **2a** composite is much thinner than the **C20K** membrane, strongly suggesting that the polymer chains were incorporated mainly on the periphery of the bilayer. In **F8K**, the polymer appeared as a heterogeneous coating on the vesicles (Figure 3-7c). The composite structure was not as stable as when observed on an IZO substrate, probably because of the strong interaction between the hydrophobic polymer bulges on the vesicles and the hydrophobic carbon film substrate.

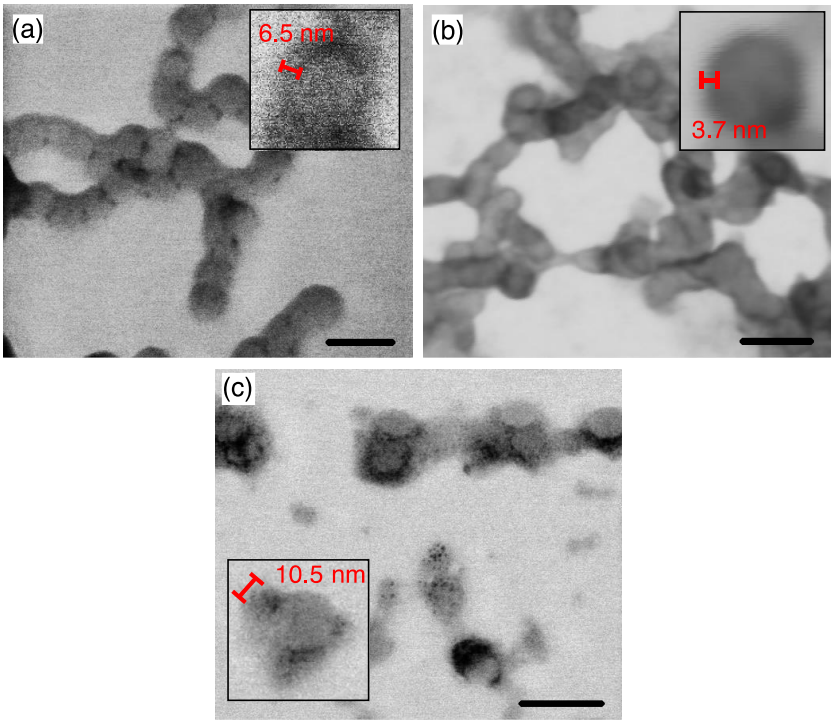

Figure 3-7. STEM images of **2a** on vesicles (a) **C8K**, (b) **C20K** and (c) **F8K**. Images were recorded on an amorphous carbon film substrate under 10^{-5} Pa. The vesicles aggregate during the preparation of the sample by the drop-casting method. The scale bars are 50 nm.

3.6 Control of polymer morphology by location in the fullerene membrane

As suggested by the different morphologies of the polymer-vesicle composites, the location of the polymer chains in the fullerene membrane strongly affected the morphology of the polymeric objects obtained after removal of the vesicles templates.

The polymer chains of **2a** grew and folded together tightly in **C8K**, which allowed the isolation of the polymer as a structurally stable capsule after removal of the water-soluble vesicles by methylene chloride extraction (confirmed by the disappearance of the absorption of the pentasubstituted fullerenes in UV-Vis spectrum, Figure 3-3c). The isolated hollow capsule has a shell thickness of ca. 2 nm (Figure 3-8a) and an average diameter of 35 ± 10 nm (estimated by STEM images, Figure 3-8i). This diameter agrees well with the average of the parent vesicle (30.7 ± 0.6 nm by DLS). The capsule was seen as a pancake object with an average height of 12.9 ± 3.5 nm (AFM, Figure 3-8d), which then collapsed into a ring structure after repeated AFM scans, suggesting that the shell is rather hard and fragile (Figure 3-8g). The

polymerization of **1a** on **C20K**, on the other hand, occurred in the structurally mobile $C_{20}H_{41}$ region to produce a much softer and sticky capsule as analyzed by STEM and AFM (Figure 3-8b,e). This capsule grown on **C20K** was not as well defined structurally as the capsule formed on **C8K**, but was far better defined than the entirely amorphous polymer prepared in water without the vesicle template (Figure 3-8h).

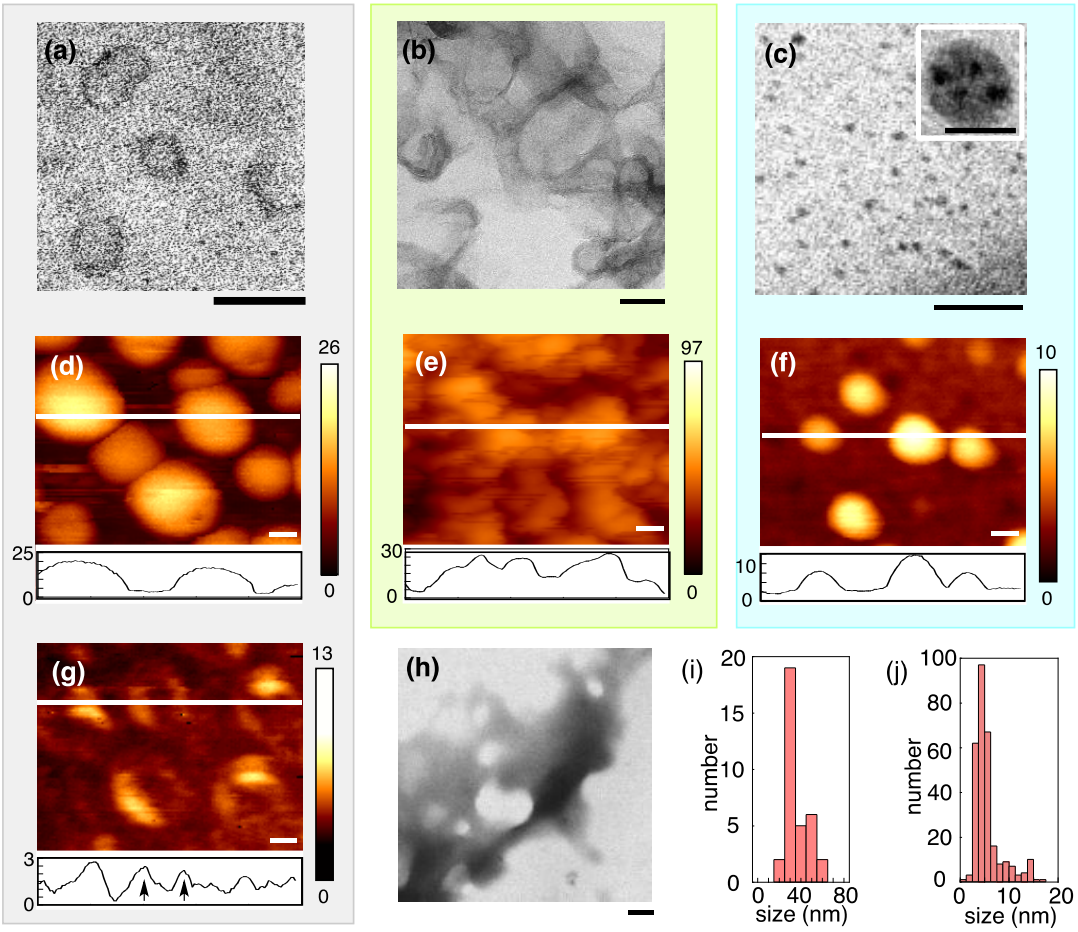

Figure 3-8. Microscopic analysis of the morphology of polymer **2a** prepared on **C8K**, **C20K**, and **F8K** vesicles. (a–c) STEM images of **2a** after removal of the vesicles by extraction. (a) Hollow capsular structure from **C8K**. (b) Deformed capsular structure from **C20K**. (c) Particular objects from **F8K**. Images were taken on a thin carbon substrate under 10^{-5} Pa. The scale bars are 50 nm and 10 nm for inset image. In a large particle shown in the inset of Fig. 4c, we see a few dark spots that may be ruthenium termini of the polymer chains. (d–f) AFM images of **2a** on mica after extraction from (d) **C8K**, (e) **C20K** and (f) **F8K** vesicles. The units of the numbers are nm. (g) AFM image of collapsed capsular assemblies of Fig. 3-8d after repetitive scans. The scale bars are 50 nm. (h) STEM image of **2a** prepared in water. (i,j) Histogram of the size of polymers extracted from (i) **C8K** and (j) **F8K** obtained from the STEM images.

As the catalyst agglomerates on the surface of the fluorous vesicle **F8K**

(Figure 3-2d), the polyester on **F8K** also agglomerated as nm-sized bulges on the surface (Figure 3-6b). The bulges on **F8K** were isolated as particle objects of 5.5 ± 2.9 nm in diameter after removal of the vesicle templates using methylene chloride extraction (STEM and AFM; Figure 3-8c,f,j). The particle diameter increased from 4.7, 5.5 to 19 nm as the monomer/catalyst ratio was decreased from 10, 2 to 1 mol% (Figure 3-9). The fluorescence quenching, water permeation, SEM images and particle sizes taken together, we consider that the polymer chains grew and folded tightly together to form the particular object in the fluorous surface, where the polyester chains and the C_8F_{17} chains were phase-separated from each other.

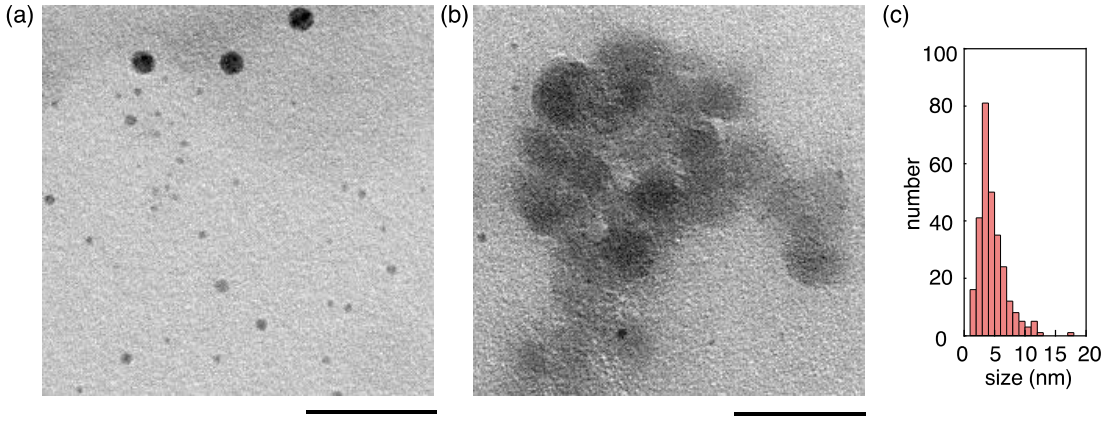

Figure 3-9. STEM images of **2a** prepared with (a) 10 and (b) 1 mol% catalyst loading on a thin carbon film. Scale bars are 50 nm. (c) Size distribution of polymer particles obtained from 10 mol% loading.

3.7 Synthesis of functionalized polymers in fullerene bilayers

The synthesis of functionalized polymers in fullerene bilayers was achieved by using functionalized norbornenes as monomers for the reaction. In addition to the copolymer **2b** which contains dansyl, a bromide functionalized polymer, **2c**, was synthesized by ROMP of di(bromoethyl)norbornene dicarboxylate **1c** on **F8K**. Attempt of polymerization of the hydrophilic norbornene dicarboxylic acid **1d** and the hydrophobic (water-insoluble) diphenylnorbornene dicarboxylate **1e** (Scheme 3-1) in **F8K** failed, suggesting that successful loading of the monomer in the bilayer is crucial for the reaction to proceed.

Scheme 3-1. Functionalized norbornenes.

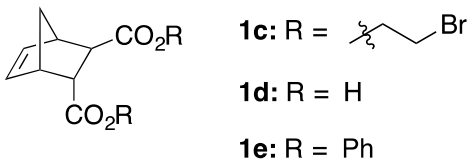

The polymer **2c** was also observed as bulges on **F8K** (Figure 3-10a). These nodules could be extracted in dichloromethane as particles a few nm thick upon STEM and AFM analyses, demonstrating the generality of polymer synthesis in fullerene bilayers (Figure 3-10b,c). EDX analysis of the polymer/vesicle composite showed the signals expected for carbon, fluorine and bromine atoms (Figure 3-10d), confirming the formation of the polymer / vesicle composite.

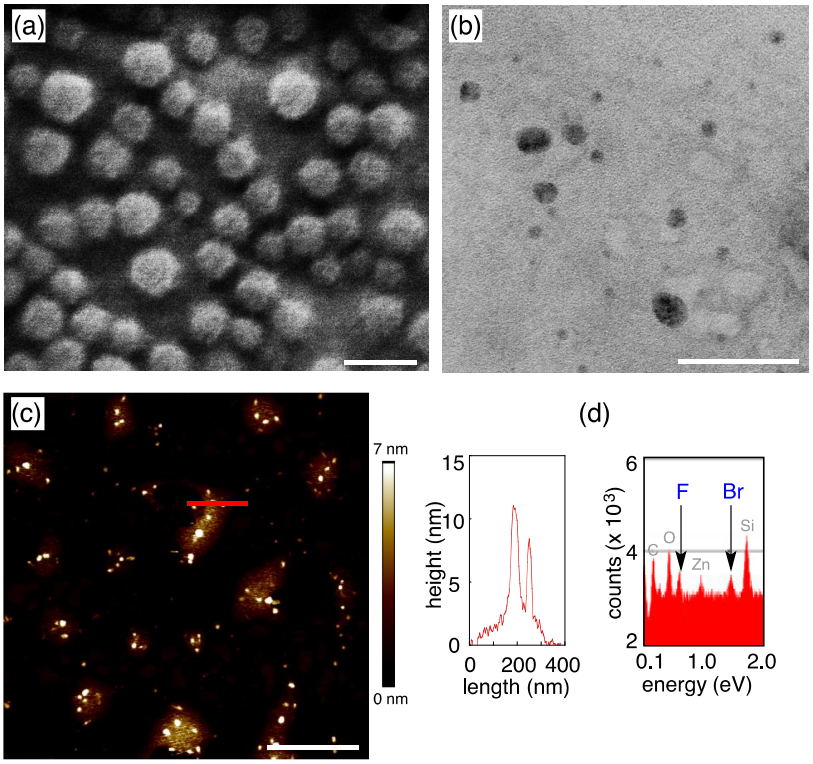

Figure 3-10. Microscopic analysis of the morphology of polymer **2c** prepared on **F8K** vesicles. (a) SEM image of **2c** on **F8K**. Image was obtained on an IZO/glass substrate under a pressure of 10^{-5} Pa. EDX spectrum is shown in (d). (b) STEM image of **2c** after removal of **F8K** by dichloromethane extraction. The image was obtained on a carbon film substrate under 10^{-5} Pa. Scale bars are 50 nm. (c) AFM image of **2c** on mica. Scale bar is 500 nm.

3.8 Conclusion

In this chapter, the robustness of the fullerene bilayers as soft assemblies

of rigid framework was demonstrated in a catalytic polymerization reaction. The fullerene bilayer vesicles possessing different internal structures serve as a nanoreactor to control the way the polymer chains grow and fold together (Figure 3-11). When polymer chains grew in the narrow interior of the bilayer, they are folded together tightly and afforded nanoscale polymer capsules after removal of the template. When polymer chains grew in a fluorous bilayer, the catalyst and the polymers are phase-segregated to form domain structures on the vesicle surface and formed particle objects. The SEM pictures of the bulges on **F8K** vesicles, because of agglomeration of the catalyst and of the polymer chains, illustrate the high potential of the low-landing voltage SEM for the surface analysis of insulating organic assemblies at high resolution[32]. Given the functional group tolerance of ROMP, I expect the vesicle-templated polymerization to be further exploited as a new tool for the preparation of nm-sized functional polymers for materials and biological applications[33,34,35,36].

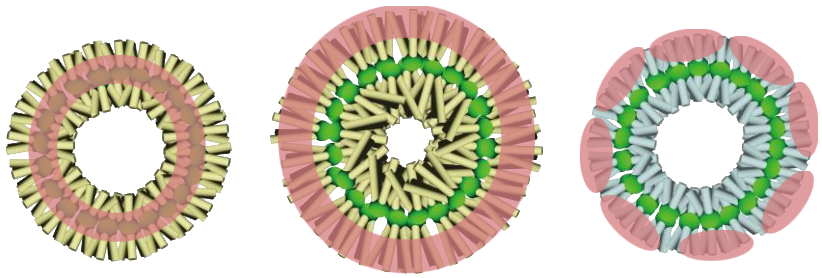

Figure 3-11. Schematic image of fullerene vesicles and polymer composites.

In chapter 4, the ability of fullerene vesicles to bear different hydrophobic groups on the surface is further explored in the assembly of hierarchical structures with metal nanoparticles.

3.9 Experimental section

3.9.1 General

All reactions dealing with air- or moisture-sensitive compounds were carried out in a dry reaction vessel under nitrogen or argon. The water content of the solvent was confirmed with a Karl-Fischer Moisture Titrator (MKC-210, Kyoto Electronic Company) to be less than 100 ppm. Analytical thin-layer chromatography was performed on glass plates coated with 0.25 mm 230-600 mesh silica gel containing a fluorescent indicator (Merck). Size exclusion chromatography (SEC) analyses were carried out at 40 °C with a GL Sciences or Shimadzu instrument equipped with an refractive-index detector and

column Shodex KF-804L by eluting tetrahydrofuran (THF) at 1 mL min^{-1}. The molecular weight was calibrated against standard polystyrene samples. Flash silica gel column chromatography was performed on silica gel 60N (Kanto, spherical and neutral, 140-325 mesh) as described by Still.[37] NMR spectra were measured on JEOL ECA-500 or JEOL ECX-400 spectrometers and reported in parts per million from tetramethylsilane. ^{1}H NMR spectra in $CDCl_3$ were referenced internally to tetramethylsilane as a standard, and ^{13}C NMR spectra to the solvent resonance. High-resolution mass spectra were acquired by electrospray ionization (ESI) using a time-of-flight mass analyzer on Bruker micrOTOF II spectrometer with a calibration standard of reserpine. IR spectra were recorded on JASCO FT-IR-6100 equipped with attenuated total reflection (ATR) and are reported as wavenumber in cm^{-1}. Distilled water was further deionized with Millipore Milli-Q. Dynamic laser light scattering (DLS) study was carried out on a Malvern Zetasizer Nano ZS machine. Atomic force microscopy (AFM) measurement was performed on a JEOL JSPM-4200 with a silicon cantilever (NSC-35, resonant frequency 120-190 kHz) or a Bruker Multimode 8 AFM with a silicon cantilever (ScanAsyst-Air, resonant frequency 45-95 kHz). High-resolution scanning transmission electron microscopy (STEM) observations were performed on a JEOL JEM-2100F at 294 K, with a spherical aberration coefficient Cs = 1.0 mm and acceleration voltage of 200 kV, under reduced pressure of 1.0×10^{-5} Pa in the sample column. The current density was ca. 0.5 pA cm^{-2}. The imaging instrument used was an ultrascan charge-coupled device (CCD) camera (512 × 512 pixels). Scanning electron microscopy (SEM) with energy dispersive X-ray analysis (EDX) was performed on FEI Magellan 400L equipped with AMETEK/EDAX Genesis APEX4. UV-Visible spectra were recorded on a JASCO V-570 UV/VIS/NIR Spectrophotometer. Fluorescence spectra were recorded on a HITACHI F-4500 Fluorescence Spectrometer.

3.9.2 Materials

Unless otherwise noted, materials were purchased from Tokyo Kasei Co., Aldrich Inc., and other commercial suppliers and used after appropriate purification before use. Anhydrous ethereal solvents (stabilizer-free) were purchased from WAKO Pure Chemical and purified by a solvent purification

system (GlassContour)[38] equipped with columns of activated alumina and supported copper catalyst (Q-5) prior to use. All other solvents were purified by distillation and stored over molecular sieves 4Å. Water enriched in ^{17}O (20.0–24.9 atom%) was purchased from Isotec and used as received. Pentaorganofullerenes (**C8K**, **C20K**, **F8K**), [17] diethyl bicyclo[2.2.1]hept-5-ene-2,3-dicarboxylate (**1a**) [39] and Hoveyda-Grubbs catalyst bearing tris[(perfluorooctyl)ethyl]silyl (**3**) [20] were prepared by the reported procedures. The aqueous solution of vesicles was prepared by the reported procedure.[24]

3.9.3 Synthesis

Synthesis of norbornene 1b (adapted from ref. 40).

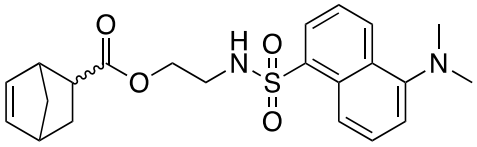

2-Dansylaminoethanol (127 mg, 0.432 mmol) was added to a suspension of 5-norbornene-2-carboxylic acid (223 mg, 1.62 mmol, endo/exo (71/29) mixture), DCC (98.9 mg, 0.479 mmol) and DMAP (1.86 mg, catalytic amount) in dichloromethane (20 mL) at room temperature. After 2 h, the solvent was removed under reduced pressure. The product was obtained as an endo/exo mixture (43/57) after purification by column chromatography (eluent: hexane/AcOEt = 70/30) and gel permeation chromatography (eluent: chloroform) as a yellow oil (31.5 mg, 18%). IR 3295, 3059, 2963, 2870, 2788, 1726, 1613, 1588, 1573, 1505, 1456, 1407, 1324, 1263, 1231, 1160, 1142, 1093, 1062, 1044, 941, 905, 863, 838, 789, 713, 683, 623, 569 cm^{-1}. ^1H NMR (500 MHz, $CDCl_3$) δ 1.18–1.30 (m, 2H), 1.31–1.35 (m, exo, 0.6H), 1.35–1.39 (m, endo, 0.4H), 1.70–1.73 (m, 1H), 1.95–2.00 (m, exo, 0.6 H), 2.66–2.68 (m, endo, 0.4 H), 2.81 (s, exo, 0.6 H), 2.85 (s, 1H), 2.89 (s, 6H), 2.97 (s, endo, 0.4 H), 3.94–4.01 (m, 2H), 5.02–5.06 (m, 1H), 5.71 (dd, *J* = 3.0, 6.0 Hz, endo, 0.4 H), 6.03 (dd, *J* = 3.0, 5.5 Hz, exo, 0.6 H), 6.09–6.11 (m, 1H), 7.17–7.20 (m, 1H), 7.26–7.29 (m, 2H), 8.25–8.29 (m, 2H), 8.55 (d, *J* = 8.5 Hz, 1H). ^{13}C NMR (125 MHz, $CDCl_3$) δ 29.15, 30.29, 41.54, 42.43, 42.55, 42.57, 42.74, 42.96, 45.38, 45.64, 46.26, 46.46, 49.60, 62.29, 62.53, 115.22, 118.48, 118.51, 123.17, 128.47, 128.50, 129.51, 129.53, 129.65, 129.67, 129.94, 130.69, 132.05, 134.46, 134.50, 135.55, 137.83, 138.04, 152.11, 175.91. HRMS (ESI+) calcd for $C_{22}H_{26}N_2O_4SK^+$ $[M+K]^+$ 453.1245, found 453.1257.

Synthesis of norbornene 1c (adapted from ref. 41).

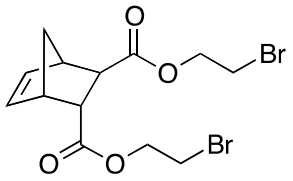

2-Bromoethanol (153 mg, 1.25 mmol) was added to a solution of *trans*-5-norbornen-endo-2,3-dicarboxylid acid (91.5 mg, 0.500 mmol) and diphenylammonium triflate (37.8 mg, 125 μmol) in toluene (1.0 mL) and the mixture was heated to 80 °C. After 12 h, the mixture was cooled to room temperature, concentrated and purified by column chromatography (silica gel, eluent: hexane/AcOEt = 10/90) to yield the product as a colorless liquid (29.3 mg, 15%). IR 3853, 3734, 3648, 3067, 2977, 2878, 2360, 2341, 1726, 1540, 1507, 1455, 1426, 1379, 1358, 1332, 1308, 1263, 1244, 1158, 1110, 1068, 1005, 953, 917, 863, 831, 722, 700, 668, 570 cm^{-1}. ^1H NMR (400 MHz, $CDCl_3$) δ1.48–1.51 (m, 1H), 1.61–1.64 (m, 1H), 2.74–2.77 (m, 1H), 3.20 (s, 1H), 3.33 (s, 1H), 3.41–3.45 (m, 1H), 3.49–3.56 (m, 4H), 4.29–4.52 (m, 4H), 6.12 (dd, J = 3.2 Hz, 5.8 Hz, 1H), 6.31 (dd, J = 3.2 Hz, 6.4 Hz, 1H). ^{13}C NMR (100 MHz, $CDCl_3$) δ 28.77, 45.72, 47.08, 47.33, 47.71, 47.80, 63.90, 64.05, 135.21, 137.65, 172.62, 173.78. Anal Calcd for $C_{13}H_{16}Br_2O_4$: C, 39.42; H: 4.07. Found: C, 39.14; H, 4.07.

Synthesis of norbornene 1e

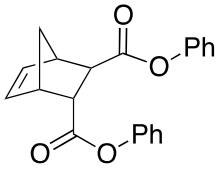

Phenol (210 mg, 2.23 mmol) was added to a suspension of *trans*-5-norbornen-endo-2,3-dicarboxylid acid (184 mg, 1.01 mmol), DCC (453 mg, 2.22 mmol) and DMAP (50.1 mg, 0.410 mmol) in dichloromethane (4.0 mL) at room temperature. After 2 h, the solvent was removed and the product was obtained after purification by column chromatography (eluent: hexane/AcOEt = 90/10) as a colorless solid (292 mg, 86%). Mp 111–113 °C. IR 2360, 2341, 1749, 1489, 1457, 1299, 1262, 1190, 1137, 1104, 958, 927, 861, 839, 769, 737, 702, 686 cm^{-1}. ^1H NMR (500 MHz, $CDCl_3$) δ1.61–1.64 (m, 1H), 1.79–1.80 (m, 1H), 3.09 (dd, J = 1.2 Hz, 4.3 Hz, 1H), 3.41 (m, 1H), 3.53 (m, 1H), 3.78 (dd, J = 4.0 Hz, 4.0 Hz, 1H), 6.29

(dd, *J* = 2.3 Hz, 5.4 Hz, 1H), 6.44 (dd, *J* = 3.5 Hz, 5.4 Hz, 1H), 7.05–7.07 (m, 2H), 7.12–7.13 (m, 2H), 7.22–7.26 (m, 2H) 7.37–7.47 (m, 4H). ^{13}C NMR (100 MHz, $CDCl_3$) δ 46.04, 47.37, 47.43, 48.12, 48.19, 121.40, 125.80, 125.87, 129.38, 129.42, 135.09, 137.92, 150.66, 150.74, 171.61, 172.89. Anal Calcd for $C_{21}H_{18}O_4$: C, 75.43; H: 5.43. Found: C, 75.21; H, 5.54.

Procedure of catalyst loading in the fullerene bilayer

A solution of catalyst **3** in dichloromethane (60 μL, 0.500 mM) was added dropwise to an aqueous solution of vesicles (1.00 mL, 0.300 mM) while stirring. The solution was stirred for 2 hours at 25 °C and dichloromethane was completely removed before it was used in the polymerization reaction.

General procedure for polymerization of 1 in fullerene vesicles loaded with catalyst

An aqueous solution of fullerene vesicles (0.30 mM, 5.00 mL) loaded with catalyst **3** (fullerene/catalyst ratio of 5) was added to a thin film of diethyl bicyclo[2.2.1]hept-5-ene-2,3-dicarboxylate (**1a**) (monomer catalyst ratio of 50) prepared from evaporation of a dichloromethane solution (20.0 mM, 375 μL). The reaction mixture was stirred for 2 hours at 60 °C. After cooling to room temperature, the aqueous solution was extracted with dichloromethane (3 × 10 mL). Removal of the organic solvent under reduced pressure gave polyester **2a** as a white solid (yield: 60–98%). ^{1}H NMR (400 MHz, $CDCl_3$) δ 1.21–1.32 (m, 6H), 1.37–1.66 (m, 1H), 1.77–2.12 (m, 1H), 2.40–3.40 (m, 4H), 3.98–4.32 (m, 4H), 5.14–5.73 (m, 2H). ^{13}C NMR (100 MHz, $CDCl_3$) δ 14.2–14.3, 39.3–41.7, 44.6–46.6, 51.6–53.4, 60.4–60.8, 129.5–130.5, 132.5–133.6, 172.8–173.9.

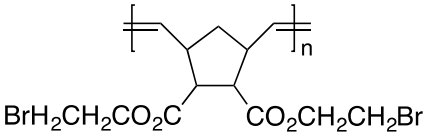

2c (1.43 mg) was obtained from **1c** in the same procedure. Yield: 43%. ^{1}H NMR ($CDCl_3$, 500 MHz) δ 0.70–0.81 (m, 1H), 1.85–2.18 (m, 1H), 2.78–3.81 (m, 8H), 4.37–4.41 (m, 4H), 5.27–5.56 (m, 2H).

Table 3-1. Molecular weight of **2b** and **2c** measured at 40 ºC in THF by GPC.

polymer	template	M_w (x 10^3)	M_n (x 10^3)	$Đ$
2b	**C8K**	200	110	1.81
2b	**C20K**	120	81	1.48
2b	**F8K**	277	163	1.70
2c	**F8K**	113	54	2.08

3.9.4 Methods

Procedure for dynamic light scattering analysis

Dynamic light scattering (DLS) measurement was performed on a Malvern Zetasizer Nano ZS equipped with an He-Ne laser operating at 4 mW power and 633 nm wavelength, and a computer-controlled correlator, at a 173 ^{o} accumulation angle. Measurement was carried out at 25 ^{o}C in a polystyrene or glass cuvette. The data were processed using dispersion technology software version 5.10 to give Z-average particle size and polydispersity index (PdI) value by cumulant analysis, and particle size distribution by CONTIN analysis.

Table 3-2. Size of pristine vesicles, catalyst-loaded vesicles and composites of vesicles and **2a** determined in water at 25 ºC by DLS. Error is the standard deviation of three consecutive measurements of the same sample.

Vesicle	Pristine Vesicle		Vesicle + **3**		Vesicle + **2a**	
	z-ave. (nm)	PdI	z-ave. (nm)	PdI	z-ave. (nm)	PdI
C8K	30.7 ± 0.6	0.31 ± 0.01	36.1 ± 0.3	0.36 ± 0.00	38.6 ± 0.1	0.38 ± 0.00
C20K	29.6 ± 0.4	0.43 ± 0.01	33.8 ± 0.4	0.41 ± 0.00	38.7 ± 0.1	0.42 ± 0.00
F8K	27.8 ± 0.5	0.13 ± 0.01	30.5 ± 0.1	0.15 ± 0.01	32.0 ± 0.6	0.16 ± 0.00

Measurement of water permeability of fullerene vesicles after polymerization

A 0.50 mM solution of $MnCl_2$ in MilliQ (0.25 mL) was added slowly to 0.25 mL of a solution of fullerene vesicle after the polymerization procedure. The hydrodynamic radius of the vesicle was determined by dynamic light scattering in different temperatures, from 10 ^{o}C to 80 ^{o}C in intervals of 10 ^{o}C. For the water permeability experiment, 30 μL of 0.50 mM solution of $MnCl_2$ in

water containing 20% of $H_2{}^{17}O$ was slowly added to 30 μL of the vesicle solution after polymerization. The sample solution was transferred to a N-502B capillary NMR tube (tube diameter, 2 mm; Nihon Seimitsu Kagaku, Tokyo, Japan). The transverse relaxation time (T_2) of ^{17}O was recorded three times without spinning the sample tube. The transverse relaxation time of the interior water (T_{2i}) was measured, and as a reference, the transverse relaxation time of blank water (T) also was measured. The permeability coefficient was obtained from Equation 3-1.

$$P = \frac{R}{3}\left(\frac{1}{T_{2i}} - \frac{1}{T_{2ref}}\right) \quad \text{(Equation 3-1)}$$

Relaxation time measurement by variable temperature NMR

The NMR probe temperature was calibrated using methanol (10–30 °C) and ethylene glycol (40–80 °C) before the measurement. The transverse relaxation time of the vesicle solution was measured from 10 to 80 °C in steps of 10 °C. The sample was equilibrated for 5 min at the set temperature each time, and the relaxation time was recorded three times at that temperature.

Eyring analysis of the water permeability

Thermodynamic parameters of the water permeability were obtained by the method developed by Eyring.[42] The Eyring equation is shown in Equation 3-2.

$$P = \frac{\lambda^2 kT}{Lh}\exp\left(\frac{\Delta S^{\ddagger}}{R}\right)\exp\left(\frac{\Delta H^{\ddagger}}{RT}\right) \quad \text{(Equation 3-2)}$$

λ is the distance between successive equilibrium positions of permeating species and was assumed to be 0.5 nm, k is the Boltzmann constant, L is the thickness of the membrane and it was estimated from a molecular model, h is the Planck constant, R is the universal gas constant, T is the absolute temperature, $\Delta S^{\ddagger}$ is the entropy of activation for permeation, and $\Delta H^{\ddagger}$ is the enthalpy of activation for permeation.

The permeability coefficients were thus plotted as $\ln(P/T)$ vs. $1/T$. Two lines were respectively obtained from 10–30 °C and 50–80 °C (for the intact vesicle) by least-squares fitting of the above equation to obtain $-\Delta H^{\ddagger}/R$ as the slope and $\ln(\lambda^2 k/Lh) + \Delta S^{\ddagger}/R$ as the intercept. The value of λ (the distance

between successive equilibrium positions of permeating species) is in the range of 0.3–1.1 nm. The variation in the entropy of activation in this range of λ is ca. ± 5%. λ was assumed to be 0.5 nm, following the discussion of Eyring. The thickness of the fullerene membrane (L) was estimated by molecular modeling of fullerene membrane structure.

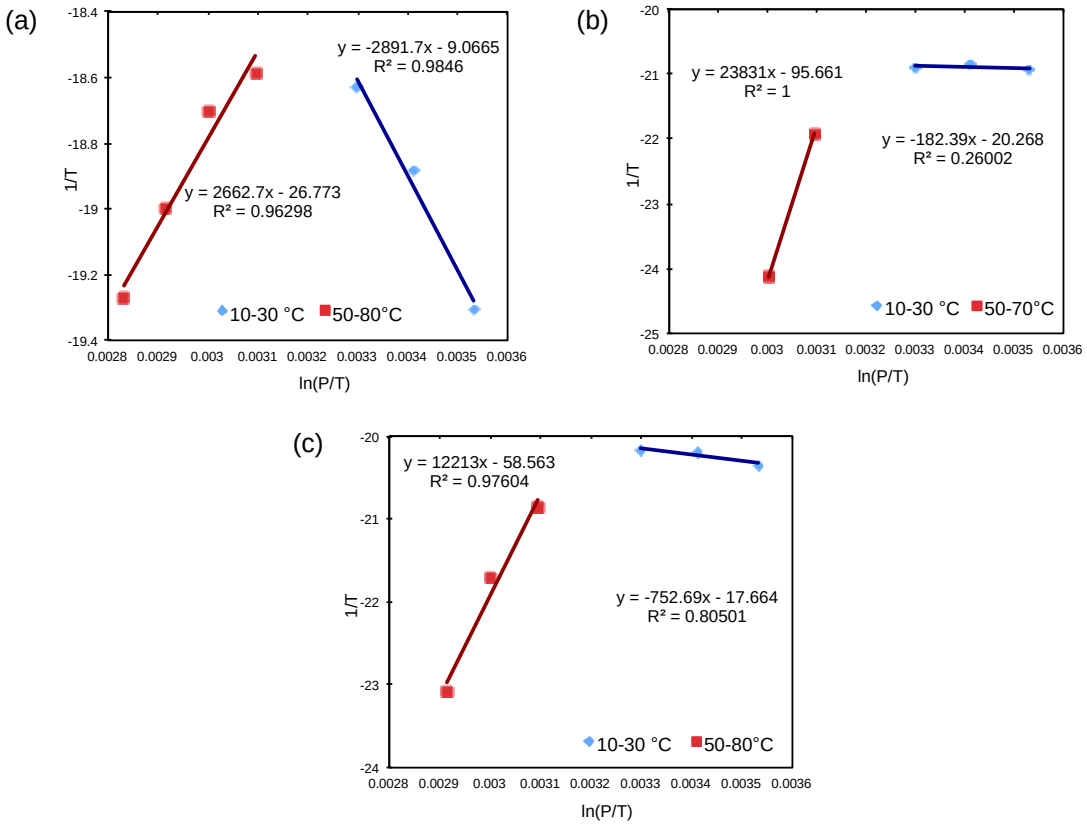

Figure 3-12. The Eyring plot [ln(*P*/*T*) vs. 1/*T*] of the permeability coefficients of (a) **C8K+2a**, (b) **C20K+2a**, and (c) **F8K+2a**.

3.9.5 Microscopic analysis and images

Sample preparation for high-resolution SEM

0.5 mL of fullerene vesicle solution was deposited on the surface of an IZO/glass substrate treated by UV/O_3 and spin coated at 500 rpm for 3 s and 1500 rpm for 30 s. The sample was dried under reduced pressure (10^{-2} Pa) at room temperature for several hours prior to the measurement.

Procedure for high-resolution SEM observation

SEM observation was performed on a FEI Magellan 400L instrument at

5 x 10^{-5} Pa. The working distance was set to 0.6–2.0 mm. Secondary electrons were collected with a through-lens detector. Observation at a beam landing voltage of 200 V was performed using beam deceleration, where 800 V of beam deceleration bias was applied to the primary electron beam accelerated at a voltage of 1 kV.

Sample preparation for simultaneous SEM/STEM analysis

The aqueous solution of catalyst-loaded vesicles (2 µL, 1 µM) was put on a transmission electron microscopy (TEM) copper mesh coated with carbon film (Super Ultra High Resolution Carbon film, thickness < 6 nm, Oken Shoji Co., Ltd.); then dried under reduced pressure (10^{-2} Pa) at room temperature for several hours prior to the measurement.

Procedure for simultaneous SEM/STEM observation

Simultaneous SEM/STEM observation was performed on a FEI Magellan 400L instrument at 5 x 10^{-5} Pa by using a retractable STEM detector with BF/DF/HAADF segment. The working distance was set to 4.0 mm. Secondary electrons were collected with a through-lens detector. Observation was performed at beam landing voltage of 25 kV and electron beam current of 0.80 nA.

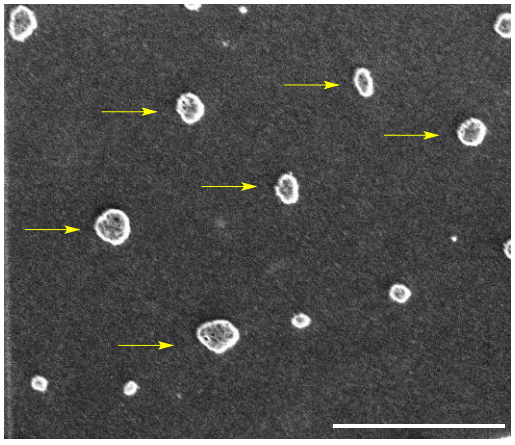

Figure 3-13. STEM image of catalyst aggregates (shown by yellow arrows) found in a sample of **PhK** vesicle. Scale bar is 500 nm.

Sample preparation for high-resolution STEM

A dichloromethane solution of **2** (2 µL, 1 µM) was put on a transmission electron microscopy (TEM) copper mesh coated with carbon film (Super Ultra High Resolution Carbon film, thickness < 6 nm, Oken Shoji Co., Ltd.); then

dried under reduced pressure (10^{-2} Pa) at room temperature for several hours prior to the measurement.

Procedure for atomic force microscopy analysis

Atomic force microscopy analysis (AFM) measurement was conducted on a JEOL JSPM-4200 with a silicon cantilever (NSC-350, resonant frequency 120-190 kHz) or a Bruker Multimode 8 AFM with a silicon cantilever (ScanAsyst-Air, resonant frequency 45-95 kHz). Samples were deposited on a mica substrate (5 × 5 mm^2) in aliquot of 2 μL under air. After drying the sample by blowing air for 10 sec and under reduced pressure (5 × 10^{-2} Pa), the AFM images were obtained by non-contact mode.

3.10 References

[1] Alberts, B., Johnson, A., Lewis, J., Raff, M., Roberts, K. & Walter, P. *Molecular Biology of the Cell*, 5th Edition, (Garland Science, New York, 2008).

[2] van Meer, G., Voelker, D. R. & Feigenson, G. W. Membrane lipids: where they are and how they behave. *Nat. Rev. Mol. Cell Biol.* **9,** 112–124 (2008).

[3] Jung, M., Hubert, D. H. W., van Veldhoven, E., Frederik, P., van Herk, A. M. & German, A. L. Vesicle-polymer hybrid architectures: a full account of the parachute architecture. *Langmuir* **16,** 3165–3174 (2000).

[4] Jung, M., Hubert, D. H. W., Bomans, P. H. H., Frederik, P., van Herk, A. M. & German, A. L. A topology map for novel vesicle–polymer vesicle architectures. *Adv. Mater.* **12,** 210–213 (2000).

[5] Jarroux, N., Keller, P., Mingotaud, A.-F., Mingotaud, C. & Sykes, C. Shape-tunable polymer nodules grown from liposomes via ring-opening metathesis polymerization. *J. Am. Chem. Soc.* **126,** 15958–15959 (2004).

[6] Meier, W. Polymer nanocapsules. *Chem. Soc. Rev.* **29,** 295–303 (2000).

[7] Hubert, D. H. W., Jung, M. & German, A. L. Vesicle templating. *Adv. Mater.* **12,** 1291–1294 (2000).

[8] Dergunov, S. A., Kesterson, K., Li, W., Wang, Z. & Pinkhassik, E. Synthesis, characterization, and long-term stability of hollow polymer nanocapsules with nanometer-thin walls. *Macromolecules* **43,** 7785–7792 (2010).

[9] Schulz, M., Olubummo, A. & Binder, W. H. Beyond the lipid-bilayer: interaction of polymers and nanoparticles with membranes. *Soft Matter* **8,** 4849–4864 (2012).

[10] Spangler, E. J., Kumar, P. B. S. & Laradji, M. Anomalous freezing behavior of nanoscale liposomes. *Soft Matter* **8,** 10896–10904 (2012).

[11] Gomes, J. F. P. d. S., Sonnen, A. F.-P., Kronenbergerm A., Fritz, J., Coelho, M. Á. N., Fournier, D., Fournier-Nöel, C., Mauzac, M. & Winterhalter, M. Stable polymethacrylate nanocapsules from ultraviolet light-induced template radical polymerization of unilamellar liposomes. *Langmuir* **22**, 7755–7759 (2006).

[12] Distefano, G., Suzuki, H., Tsujimoto, M., Isoda, S., Bracoo, S., Comotti, A., Sozzani, P., Uemura, T. & Kitagawa, S. *Nat. Chem.* **5**, 335–341 (2013).

[13] Cullis, P. R. & De Kruijff, B. Lipid polymorphism and the functional roles of lipids in biological membranes. *Biochim. Biophys. Acta* **559,** 399–420 (1979).

[14] Rosoff, M. *Vesicles* (Marcel Dekker, 1996).

[15] Sawamura, M. *et al.* Pentaorgano[60]fullerene $R_5C_{60}^-$. A water soluble hydrocarbon anion. *Chem. Lett.* **9,** 1098–1099 (2000).

[16] Zhou, S. *et al.* Spherical bilayer vesicles of fullerene-based surfactants in water: a laser light scattering study. *Science* **291,** 1944–1947 (2001).

[17] Homma, T., Harano, K., Isobe, H. & Nakamura, E. Preparation and properties of vesicles made of nonpolar/polar/nonpolar fullerene amphiphiles. *J. Am. Chem. Soc.* **133,** 6364–6370 (2011).

[18] Dubois, P., Coulembier, O. & Raquez, J.-M. Eds. *Handbook of ring-opening polymerization* (Wiley-VCH, 2009)

[19] Svirbely, W. J., Eareckson, W. M., Matsuda, K., Pickard, H. B., Solet, I. S. & Tuemmler, W. B. Physical properties of some organic insect repellents. *J. Am. Chem. Soc.* **71,** 507–509 (1949).

[20] Michalek, F. & Bannwarth, W. Application of a Grubbs–Hoveyda metathesis catalyst noncovalently immobilized fluorous–fluorous interactions. *Helv. Chim. Acta* **89,** 1030–1037 (2006).

[21] Hesle, E. M., Tobis, J., Tiller, J. C. & Bannwarth, W. Ring-closing olefin metathesis in the aqueous phase of amphiphilic conetworks consisting of fluorophilic and hydrophilic compartments. *J. Fluorine Chem.* **129,** 968–973 (2008).

[22] Homma, T., Harano, K., Isobe, H. & Nakamura, E. Nanometer-sized fluorous fullerene vesicles in water and on solid surfaces. *Angew. Chem. Int. Ed.* **49,** 1665–1668 (2010).

[23] Harano, K., Minami, K., Noiri, E., Okamoto, K. & Nakamura, E. Protein-coated nanocapsules via multilevel surface modification. Controlled preparation and microscopic analysis at nanometer resolution. *Chem. Commun.* **49,** 3525–3527 (2013).

[24] Lenaz, G. Lipid fluidity and membrane protein dynamics. *Biosci. Rep.* **11**, 823–837 (1987).

[25] Harano, K., Gorgoll, R. M. & Nakamura, E. Binding of aromatic molecules in the fullerene-rich interior of a fullerene bilayer vesicle in water. *Chem. Commun.* **49,** 7629–7631 (2013).

[26] Matsuo, Y., Morita, K., Nakamura, E. Penta(pyrenyl)[60]fullerenes: pyrene–pyrene and [60]fullerene–pyrene interactions in the crystal and in solution. *Chem.–Asian J.* **3,** 1350–1357 (2008).

[27] Holmes-Farley, S. R., Whitesides, G. M. Fluorescence properties of dansyl groups covalently bonded to the surface of oxidatively functionalized low-density polyethylene film. *Langmuir* **2,** 266–281 (1986).

[28] Isobe, H., Homma, T. & Nakamura, E. Energetics of water permeation through fullerene membrane. *Proc. Natl. Acad. Sci. U.S.A.* **104,** 14895–14898 (2007).

[29] Reeves, J. P. & Dowben, R. M. Water permeability of phospholipid vesicles *J. Membr. Biol.* **3,** 123–141 (1970).

[30] Harano, K.; Minami, K.; Noiri, E.; Okamoto, K.; Nakamura, E. Protein-coated nanocapsules via multilevel surface modification. Controlled preparation and microscopic analysis at nanometer resolution. *Chem. Commun.* **49**, 3525–3527 (2013).

[31] Homma, T. Solution and electron microscopic studies of chemically modified carbon nanoclusters (Ph.D. Thesis). The University of Tokyo, Tokyo (2011). The water content the vesicle can be leaked after destabilization of the fullerene membrane by additive molecules.

[32] Yabu, H. *et al.* Polymer Janus particles containing block-copolymer stabilized magnetic nanoparticles. *ACS Appl. Mater. Interfaces* **5,** 3262–3266 (2013).

[33] Such, G. K., Johnston, A. P. R. & Caruso, F. Engineered hydrogen-bonded polymer multilayers: from assembly to biomedical applications. *Chem. Soc. Rev.* **40,** 19–29 (2011).

[34] Kim, D. *et al.* Direct synthesis of polymer nanocapsules: self-assembly of polymer hollow spheres through irreversible covalent bond formation. *J. Am. Chem. Soc.* **132,** 9908–9919 (2010).

[35] Maeda-Mamiya, R. *et al. In vivo* gene delivery by cationic tetraaminofullerene. *Proc. Natl. Acad. Sci. U.S.A.* **107,** 5339–5344 (2010).

[36] Minami, K. *et al.* siRNA delivery targeting to the lung via agglutination-induced accumulation and clearance of cationic tetraamino fullerene. *Sci. Rep.* **4,** 4916 (2014).

[37] Still, W. C., Kahn, M. & Mitra, A. Rapid chromatographic technique for preparative separations with moderate resolution. *J. Org. Chem.* **43**, 2923–2925 (1978).

[38] Pangborn, A. B., Giardello, M. A., Grubbs, R. H., Rosen, R. K. & Timmers, F. J. Safe and convenient procedure for solvent purification. *Organometallics* **15**, 1518–1520 (1996).

[39] Polo, E.; Forlini, F.; Bertolasi, V.; Boccia, A. C. & Sacchi, M. C. Self-immobilizing precatalysts: Norbornene-bridged zirconium ansa-metallocenes. *Adv. Synth. Catal.* **350**, 1544–1556 (2008).

[40] Brambilla, D., Nicolas, J., Droumaguet, B. J., Andrieux, K., Marsaud, V., Couraud, P.–O. & Couvreur, P. Design of fluorescently tagged poly(alkyl cyanoacrylate) nanoparticles for human brain endothelial cell imaging. *Chem. Commun.* **46**, 2602 (2010).

[41] Wakasugi, K., Misaki, T., Yamada, K. & Tanabe, Y. Diphenylammonium triflate (DPAT): efficient for esterification of carboxylic acids and for transesterification of carboxylic esters with nearly equimolar amounts of alcohols. *Tetrahedron Lett.* **41**, 5249–5252 (2000).

[42] Zwolinski, B. J., Eyring, H. & Reese, C. E. Diffusion and membrane permeability. *J. Phys. Chem.* **53**, 1426–1453 (1949).

— Chapter 4 —
Cooperative self-assembly of gold nanoparticles on the hydrophobic surface of fullerene vesicles in water

4.1 Introduction: Assemblies of plasmonic nanoparticles

Nanoparticles of noble metals (e.g. silver, gold) exhibit collective properties when interparticle distance is sufficiently small for the surface plasmon resonance of individual particles to couple.[1] These collective properties, such as increased light absorption and scattering, can be tuned for the construction of smart materials in mesoscopic assemblies.[2,3] In particular, the association of the collective properties of nanoparticles with a vesicle morphology has been investigated in assemblies of potential biological use with applications such as light-triggered release of inner contents and cell imaging.[4,5]

However, the construction of vesicles containing a large amount of metal nanoparticles is not a simple task and research for an efficient method is in progress. The methods reported until the present moment can be classified in two categories: ligand-mediated assembly of nanoparticles into vesicles and decoration of surfactant vesicles with nanoparticles. The former requires the synthesis of complex ligands and relies on serendipity for the formation of the desired vesicles.[6,7] In the latter, the adsorption of nanoparticles on soft surfactant assemblies often results in destabilization of the vesicle membrane, limiting the amount of nanoparticle that can be loaded without destruction of the vesicle structure.[8] Moreover, electrostatic interaction that is the main tool for the decoration of vesicles is far from ideal. It is difficult to control the assembly process and repulsion between neighboring charged particles prohibits the construction of decorated vesicles with dense nanoparticle coverage.[9,10]

As demonstrated in chapter 3, orthogonal π-π and hydrophobic (or fluorous) interactions strongly stabilizes a 30 nm vesicle made of $R_5C_{60}^-K^+$ amphiphiles.[11,12,13] The unique ternary architecture of the fullerene bilayer grants the vesicle a hydrophobic surface, creating an interface in water. By using interfacial adsorption as the main driving force for nanoparticle adsorption instead of electrostatic interaction, I expected to reduce interparticle repulsion and produce hybrids of fullerene vesicles and gold nanoparticles where interparticle coupling would be possible.

In this chapter, the decoration of a fullerene bilayer vesicle made of fullerene pentaadduct amphiphiles was achieved by interfacial adsorption of

neutral oligo(ethylene oxide) (OEO)-coated gold nanoparticles (Figure 4-1). Adsorption of 3.5 nm tetraethylene oxide(TEO)-coated nanoparticles (**NP-1**) on the fluorinated vesicles produced densely-coated vesicles in a cooperative manner without aggregation or fusion, as commonly occurs in the case of electrostatic adsorption. The nanoparticle created a network on the vesicle surface, making stable hybrids that withstand chromatography purification. The robustness of the assembly was further demonstrated by in situ growth of the particles to up to twice of their original size, 7.2 nm, in which interparticle coupling was detected.

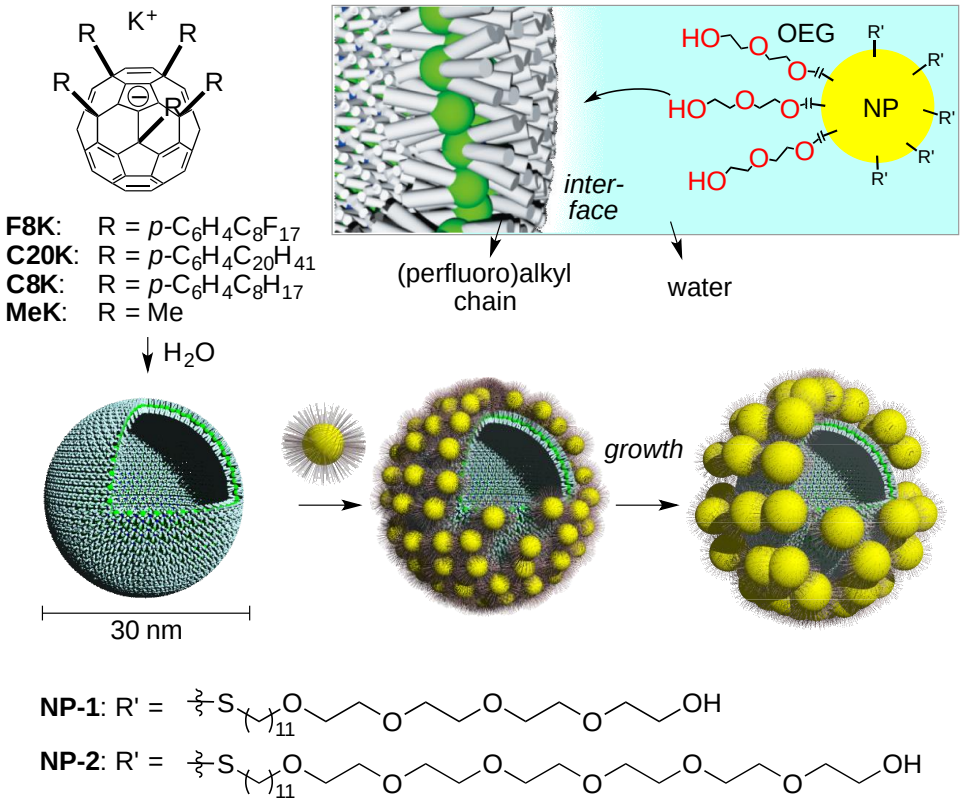

Figure 4-1. Self-assembly and growth of gold nanoparticles on the hydrophobic surface of fullerene vesicles in water.

4.2 Adsorption of surface-active gold nanoparticles on fullerene vesicles

The adsorption of gold nanoparticles coated with (11-mercaptoundecyl)tetra(ethylene oxide) (**NP-1**) was investigated because they were reported to assemble on the water/oil interface in a Pickering emulsion.[14] These particles are highly stable and their use in the biological applications has also been reported.[15, 16] **NP-1** was synthesized by a standard procedure

following the Brust method[17,18] and water-soluble particles of 3.5 ± 1.0 nm in diameter, as determined from STEM images, were obtained (details in section 4.8, Figure 4-13). The adsorption of **NP-1** at the air/water interface was confirmed by decrease of the surface tension of a water droplet in air from 70.7 to 46.8 mN m^{-1} (ca. 3.6 mM) measured by the pendant droplet method in a tensiometer. Four vesicles containing surface substituents of different hydrophobicity (**MeK**, **C8K**, **C20K**, and **F8K**; Figure 4-1) were prepared by spontaneous assembly of $R_5C_{60}^-K^+$ amphiphiles upon injection into water. The hydrodynamic diameter, determined by DLS, was 27–47 nm.

Surface tension measurement of a water droplet containing **NP-1** and vesicles indicated a particularly high affinity of **NP-1** to the surface of **F8K** vesicles (Figure 4-2). The fullerene vesicle does not have surface activity (Figure 4-2a, red line)[19]; therefore, the change in the surface tension can be assigned exclusively to the adsorption of nanoparticles at the air/water interface. The initial surface tension of the solution after droplet formation (t = 0 min) was similar to the one of water in air (70.7–71.6 mN m^{-1}) for all vesicles, but gradually decreased with time at ca. 11 particles per vesicle. This result was interpreted as desorption of nanoparticles from the vesicle surface and readsorption at the air/water interface (Figure 4-2d). After 15 minutes, the surface tension decreased to 70.3 ± 0.3 mN m^{-1} for **F8K**, 69.0 ± 1.9 for **C20K**, 58.6 ± 0.3 for **C8K**, and 50.1 ± 2.8 for **MeK** (Figure 4-2b), suggesting that the nanoparticle adsorption was stronger in the order of (**F8K**, **C20K** > **C8K** > **MeK**). This result correlates well with the length of the alkyl chain on fullerene, and thus, the hydrophobicity of the fullerene membrane, supporting the hypothesis of interfacial adsorption of the nanoparticles on the vesicle surface. The difference between **F8K** and **C20K** vesicles was clarified by increasing the number of particles per vesicle to ca. 22, and adsorption on **F8K** was found to be the most stable (Figure 4-2c). Based on this result, **F8K** vesicle was further investigated for the fabrication of hybrids with gold nanoparticles.

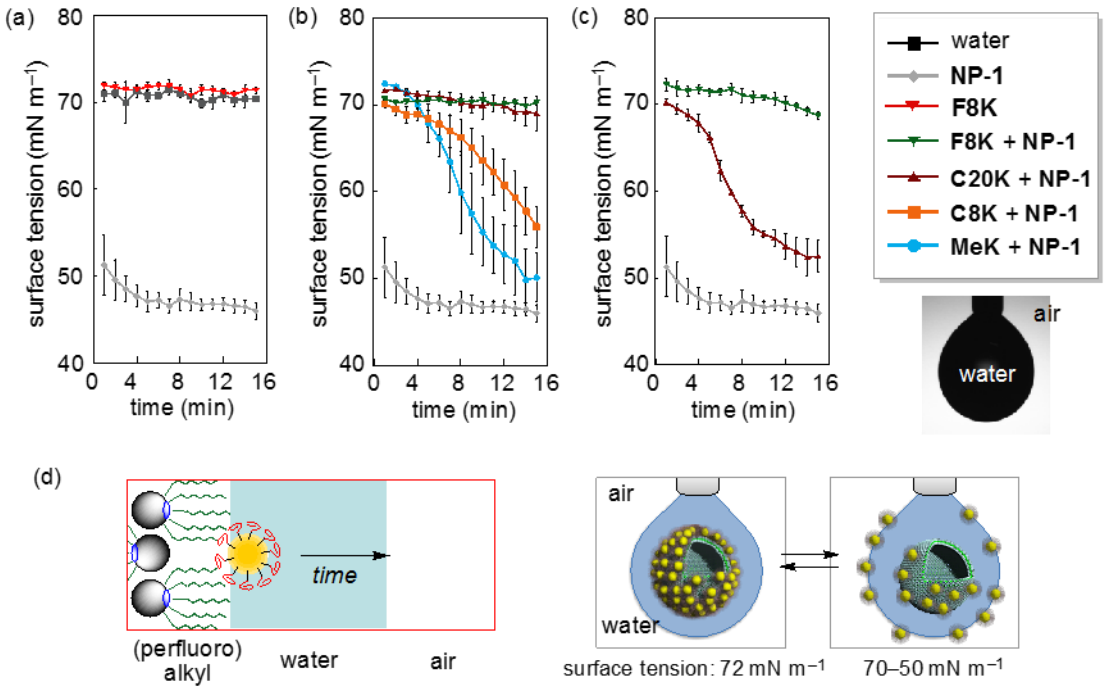

Figure 4-2. Adsorption of gold nanoparticles **NP-1** at interfaces. Time evolution of the surface tension of a water droplet in air. Error bar is the standard error calculated from three measurements. (a) Effect of **NP-1** and **F8K** in the surface tension of water in air. Effect of fullerene vesicles in the adsorption of **NP-1** at the water/air interface when (b) ca. 11 and (c) ca. 22 particles per vesicle are used. (d) Schematic image of desorption of **NP-1** from the surface of fullerene vesicles and readsorption at the water/air interface.

4.3 Decoration of F8K vesicle with gold nanoparticle NP-1

Adsorption on vesicles of **F8K** was achieved by simply adding the aqueous solution of nanoparticles to vesicles (Figure 4-3). The hybrids were structurally stable to be separated from the excessive amount of gold nanoparticles by filtration of the solution through a Sephacryl (dextran/bisacrylamide) size-exclusion column (Figure 4-3a). The hydrodynamic diameter of the composite, 49.4 ± 0.2 nm (DLS), is 19 nm larger than of the vesicle template, which is close to twice of the hydrodynamic diameter of **1**, 8.2 ± 0.1 nm (Figure 4-3b). The ζ-potential of the vesicles, –45.6 ± 2.4 mV (pH = 7.0), increased to –13.7 ± 0.8 mV, which is the same as that of nanoparticles, –14.9 ± 3.1 mV (Figure 4-3c). The absorption peak at 510 nm from the surface plasmon resonance of **NP-1** was also identified in the solution of decorated vesicles (Figure 4-3d).

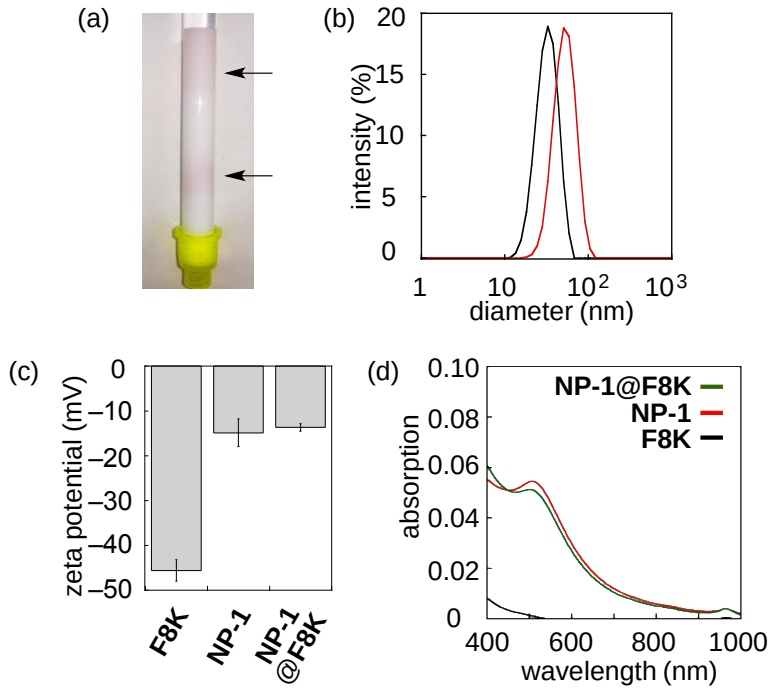

Figure 4-3. Adsorption of gold nanoparticles **NP-1** on fluorous **F8K** vesicles in water. (a) Clear separation of non-adsorbed particles (top band) from decorated vesicles (bottom band) by gel permeation chromatography in a Sephacryl (dextran/bisacrylamide) size-exclusion column. (b) Size distribution of **F8K** vesicles before (black line) and after (red line) nanoparticle decoration measured by DLS at 25 ºC. (c,d) ζ-potential and absorption spectra of **F8K** before and after decoration.

The attachment of the nanoparticles on the vesicle surface was robust enough to be observed under electron microscopy conditions after removal of water under 10^{-5} Pa (Figure 4-4). The decorated vesicles were casted on a carbon film and characterized by STEM. All the nanoparticles were attached on the vesicle surface (Figure 4-4a,b). The surface morphology of decorated vesicles, investigated by high-resolution SEM on an IZO/glass substrate, showed that the particles were tightly packed completely covering the vesicle surface (Figure 4-4c). The size of the vesicles, as determined from STEM images, increased from 30.8 ± 5.2 nm to 37.7 ± 4.0 nm after adsorption of **NP-1**, an increase of 6.9 nm, which corresponds to twice the size of the nanoparticle core (Figure 4-4d).

Although fullerene vesicles immediately precipitate under high concentrations of salt, the hybrids were stable in phosphate buffer saline showing a small size increase of 10% after 8 h (Figure 4-5). On the other hand, acidic conditions (pH) still protonates the fullerene amphiphile, which destroys

the vesicle structure immediately (Figure 4-5c).

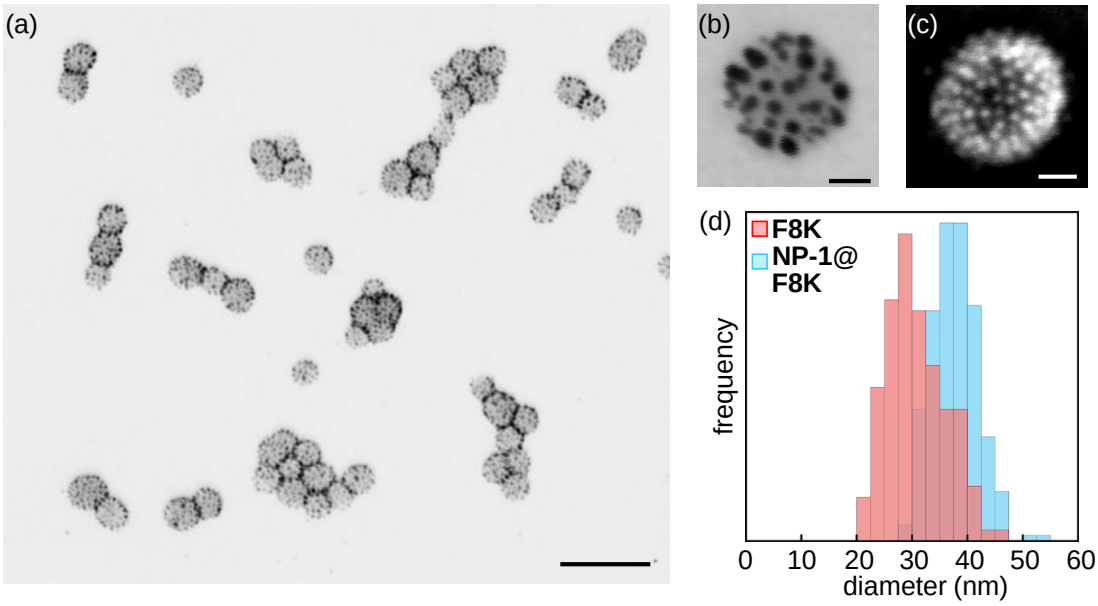

Figure 4-4. Microscopic analysis of assemblies of **NP-1** on **F8K** vesicles under 10^{-5} Pa. (a) STEM image of decorated vesicles. Scale bar is 100 nm. (b,c) STEM and SEM images of a decorated vesicle. STEM images were obtained on an amorphous carbon film. SEM image was obtained on an IZO/glass substrate. Scale bar is 10 nm. (d) Size distribution of **F8K** vesicle before (red bars, n = 136) and after (blue bars, n = 258) decoration with **NP-1** determined from STEM images.

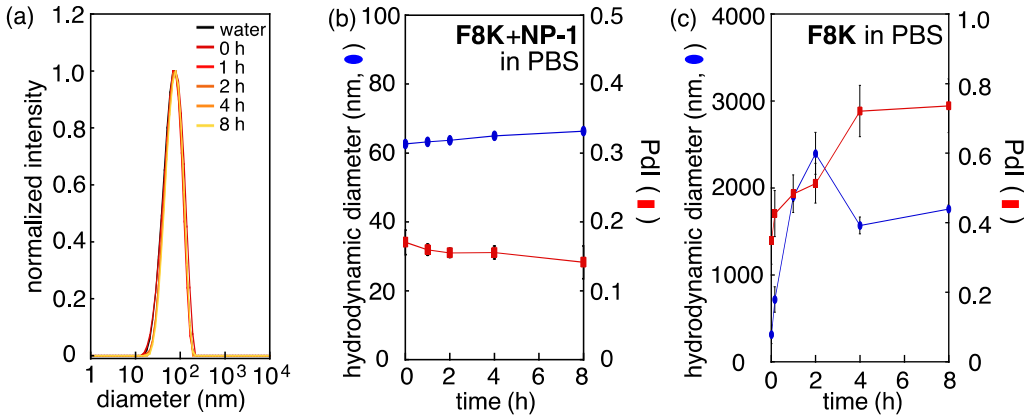

Figure 4-5. Time-evolution of the hydrodynamic diameter of **F8K** vesicles in phosphate buffer saline (PBS: 137 mM NaCl, 2.7 mM KCl, $Na_2HPO_4 \cdot H_2O$ 10 mM, KH_2PO_4 2 mM; pH = 7.4) after decoration with **NP-1**. (a) Size distribution. (b,c) Time-evolution of diameter (blue line) and PdI (red line) of decorated and non-decorated vesicles. An error bar shows the standard deviation of three measurements at 25 ºC measured by DLS.

4.4 Cooperative assembly of gold nanoparticles on fullerene vesicles

To clarify the origin of the high stability of the adsorption of **NP-1** on **F8K** vesicles, the mechanism of the nanohybrid formation was investigated.

When the ratio of gold nanoparticles per vesicle was reduced to an amount insufficient to completely coat all vesicles, mainly only two types of structures in STEM images: completely coated vesicles and vesicles without any particles on the surface (Figure 4-6). This observation is quantified for the correlation shown in Figure 4-6c (for [Au]/[**1**] = 2.25), which indicates that the number of vesicles bearing NPs decreases for n = 1 to 7 and then increases above n = 13–ca. 25. The percentage of coated vesicles in the sample was proportional to the concentration of gold nanoparticles and the average number of gold nanoparticles per vesicle in hybrids was 22.6 ± 1.7 and showed only a small correlation to the mole ratio of gold atoms per fullerene amphiphile, which therefore can be characterized as a cooperative process (Figure 4-6d, blue and red lines).

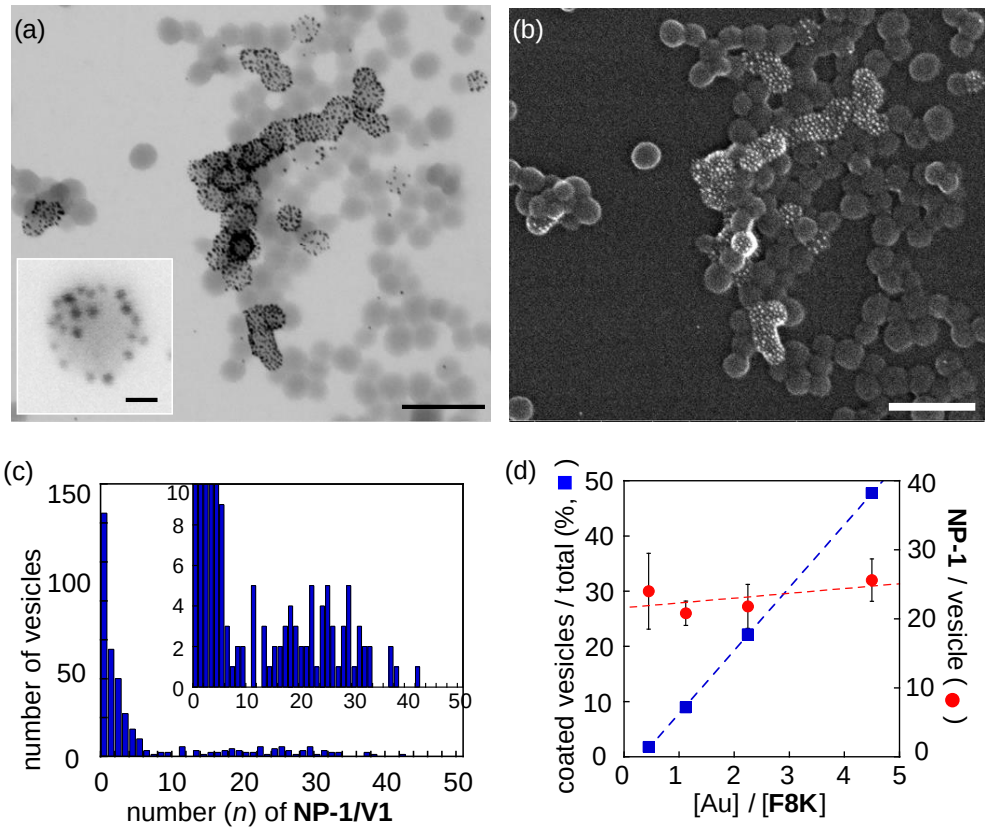

Figure 4-6. Mechanistic investigation of adsorption of nanoparticles on fullerene vesicles. (a,b) STEM and SEM images of cooperative adsorption of **NP-1** on **F8K** vesicles obtained on an amorphous carbon film under 10^{-5} Pa. Scale bars are 100 nm. Inset image shows the formation of a nanoparticle domain on the surface of a **F8K** vesicle. Scale bar is 10 nm. (c) The number of vesicles bearing an n number of NP-1/vesicle examined for 339 vesicles. Inset shows a magnified histogram. (d) Concentration dependence in the formation of decorated vesicles (blue square) and number of particles per vesicle (red circle).

Some hybrids in the middle of the formation process were also observed in the STEM images (Figure 4-6a, inset). The particles clearly attaches near to other particles rather to a separate position, forming domains on the vesicle surface. This structure suggests the existence of interparticle interactions.

The interparticle interaction was investigated by ^{1}H NMR of the nanoparticle in D_2O using (3-(trimethylsilyl)-2,2',3,3'-tetradeuteropropionic acid (TMSP-d_4) as an external standard (Figure 4-7). The fullerene vesicle exhibits no ^{1}H NMR signal and thus only the signal from the capping ligand of the nanoparticle was detected (Figure 4-7a, top). The signal intensity decreased proportionally to the amount of nanohybrid formed (Figure 4-7b). When all gold nanoparticles were adsorbed on the surface of fullerene vesicles, the signal decreased to 40% of the initial value. This large decrease in the signal intensity is explained by the reduction of the mobility of surface ligands in the vesicle-particle and particle-particle interfaces. The linearity between the signal intensity and amount of free particles suggests that attractive interaction only occurs on the vesicle surface and multiple nanoparticle layers are not likely to be formed. This was confirmed by electron microscope images of the vesicles in the presence of a large excess amount of nanoparticles (Figure 4-16).

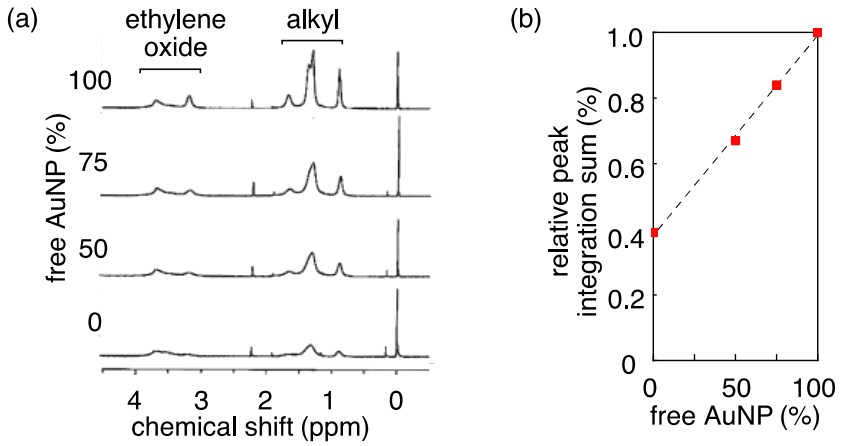

Figure 4-7. Effect of nanoparticle adsorption in the mobility of the capping ligand. (a) ^{1}H NMR spectra and (b) signal intensity of **NP-1** in D_2O after addition of different amounts of vesicles **F8K** vesicles until all nanoparticles were adsorbed on the vesicle surface. 3-(trimethylsilyl)-2,2',3,3'-tetradeuteropropionic acid (TMSP-d_4) was used as an external standard. The percentage of free nanoparticles was calculated from a calibration curve obtained from STEM images.

Comparison of SEM and STEM images of a same vesicle (Figure 4-8a,b),

allowed us to determine the distance of neighbouring particles on the top of a vesicle as 1.7–2.4 nm (Figure 4-8c), which is much less than the length of the surface ligand in a linear conformation, 2.9 nm (Figure 4-8d). This result further supports the existence of an interparticle interaction mediated by the capping ligands on the nanoparticle, as suggested by the ^{1}H NMR experiments.[7]

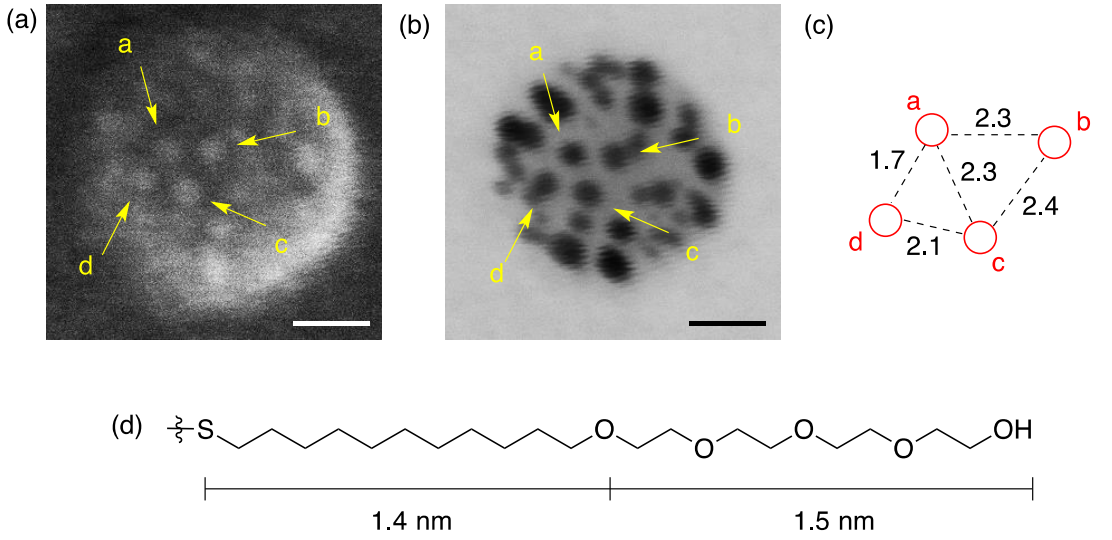

Figure 4-8. Interparticle distance of **NP-1** on a vesicle of **F8K**. (a,b) SEM and STEM images of a same hybrid structure obtained by simultaneous scan. A set of nanoparticles on the top of the vesicle is shown by yellow arrows. Measured on an amorphous carbon film under 10^{-5} Pa. Scale bars are 10 nm. (c) Schematic image of interparticle distance determined from b. (d) Length of the linear form of tetra(ethylene oxide)undecylthiol ligand calculated from a molecular model.

The adsorption of OEG-capped nanoparticles at water/oil interfaces has been previously reported to induce conformational changes of the OEG moiety, that tend to occupy as much interfacial area as possible by assuming stretched conformations that are more elongated than those in bulk water.[20] This phenomenon was observed indirectly by the enhancement of the catalytic activity of the nanoparticles after adsorption on **F8K** vesicles (Figure 4-9).

In the case of free **NP-1**, the steric hindrance of the OEG moiety on the particle surface prevents a *p*-nitrophenol substrate to reach the surface of the nanoparticle (Figure 4-9b, black line). Upon adsorption of **NP-1** on the vesicle surface, the conformational change of the OEG moiety allowed the substrate to reach the nanoparticle surface and it was reduced to *p*-aminophenol (red line). An induction time of 600 seconds was observed before the reaction began. This induction time is typical for a heterogeneous catalytic reaction and is related to

the activation or restructuration of the metal surface by *p*-nitrophenol molecule before the reaction could start.[21] Note that the potassium ions did not activate **NP-1** neither pristine vesicles were catalytic active (green and blue lines, respectively).

NP-1 was also activated by lipid vesicles made of phosphatidyl choline (d_{hyd} = 197 ± 6 nm, Figure 4-9c, grey line).

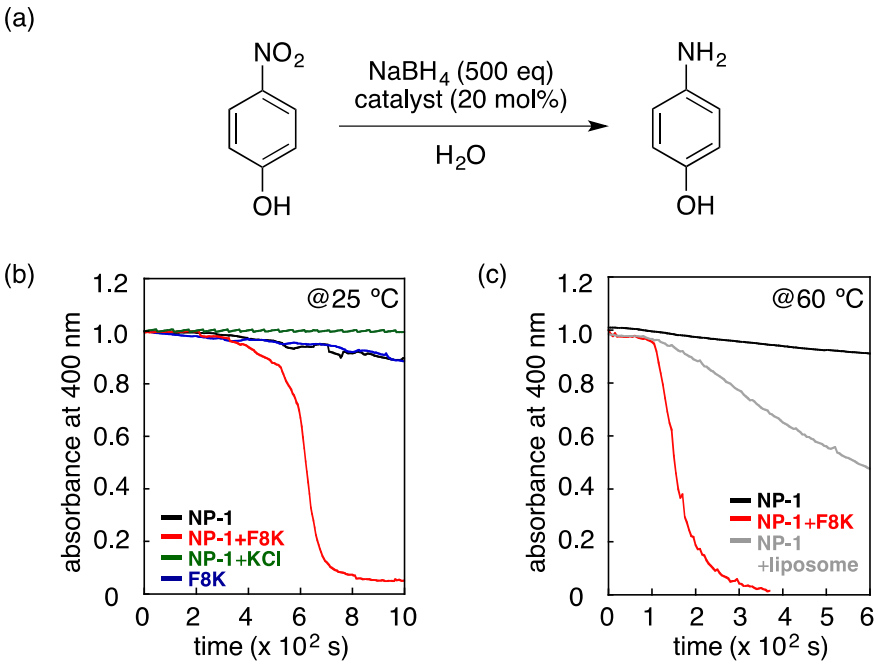

Figure 4-9. Reduction reaction of *p*-nitrophenol catalyzed by **NP-1** adsorbed on **F8K** vesicles. (a) Scheme of the catalytic reaction. (b,c) The reaction was monitored by absorption at 400 nm of *p*-nitrophenolate that was formed *in situ* from *p*-nitrophenol. The reduction reaction only proceeds in the case **NP-1** is adsorbed on **F8K** vesicles (red line) or liposomes (grey).

The results obtained by electron microscopy, NMR and catalysis studies, suggest that upon adsorption on the surface of **F8K** vesicles, the conformation of the capping ligand of **NP-1** changes and intermediates interparticle interaction, strongly stabilizing the supramolecular structure.

4.5 *In situ* growth of gold nanoparticles on fullerene vesicles for interparticle coupling

The hybrids served as a platform for *in situ* deposition of gold atoms on the adsorbed **NP-1** without destruction of the vesicle structure. Thus, the diameter of **NP-1** was increased from 3.5 ± 1.0 nm to 7.2 ± 1.4 nm by adding a

solution of $HAuCl_4/K_2CO_3$ (1:3) and formaldehyde (excess) to a solution of **NP-1** on **V1** (2 h at room temperature, Figure 4-10).[22] The excessive reagents were removed by dialysis of the solution in water. Note that attempts to adsorb large gold NPs (6.7 nm in diameter) on **F8K** failed.

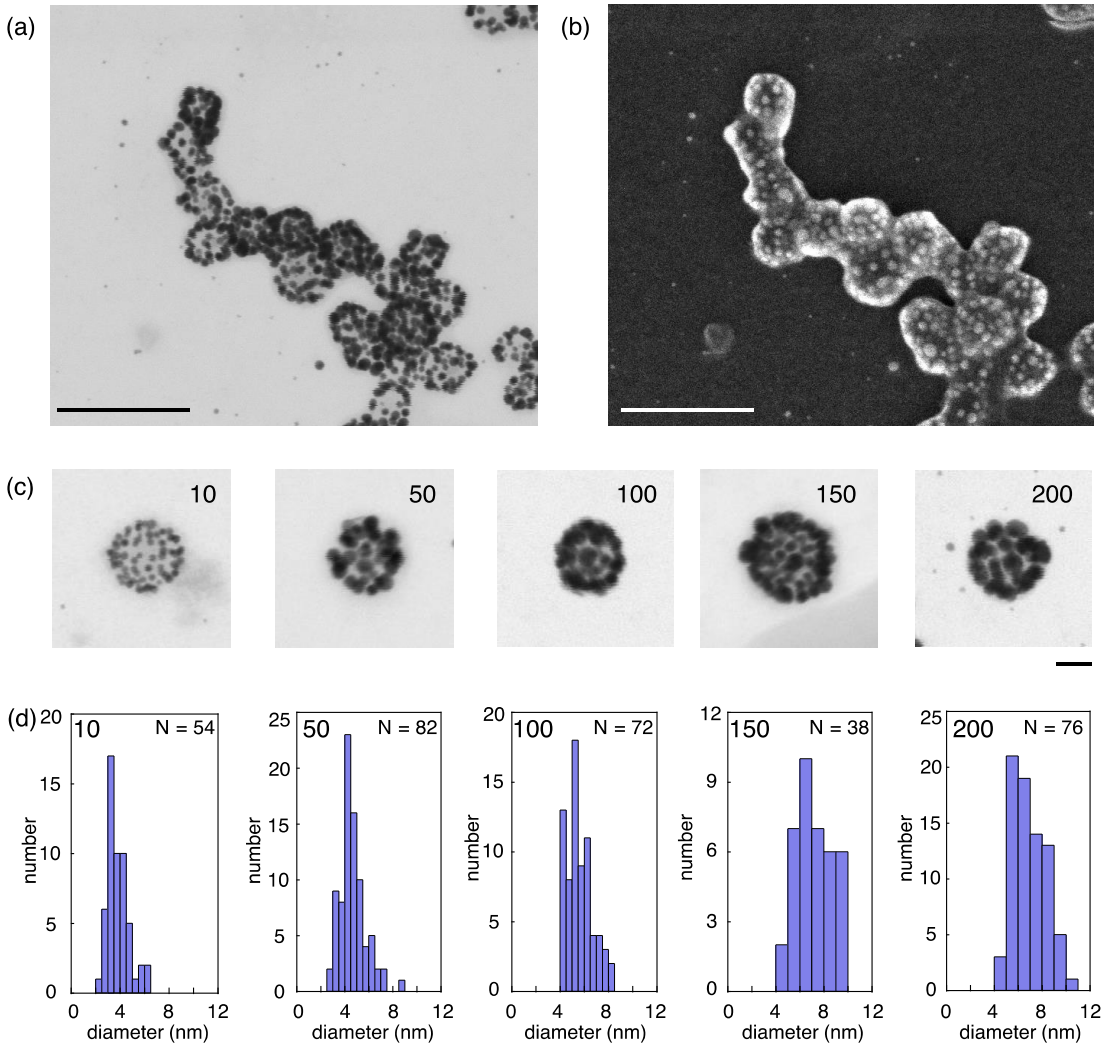

Figure 4-10. *In situ* growth of gold nanoparticles on the surface of fullerene vesicles. (a,b) STEM and SEM images of nanohybrids after growth of gold nanoparticles. (c) A series of TEM images illustrating the growth of **NP-1** on **F8K** after addition of different amounts of growth solution, referred as the ratio of gold atoms per fullerene in the numbers. Scale bar are 100 nm or 20 nm for magnified images. (d) Histogram of diameter of nanoparticles after growth.

The light absorption of the vesicle conjugates increased with the size of the nanoparticles (Figure 4-11a). The absorption peak wavelength of the solution also shifted considerably from 520 nm to 537 nm (Figure 4-11b) when the size of the nanoparticle became larger than 4.6 ± 1.1 nm. Further increase of the nanoparticle size resulted in a smaller shift, up to 544 nm, at a size of 7.2

nm (Figure 4-11c). After collapse of the vesicles by protonation of the fullerene amphiphile by addition of HCl and neutralization with NaOH, the absorption maximum shifted back to 517 nm, which is the value expected for nanoparticles of 7 nm (Figure 4-11d).[23] Therefore, the large absorption shift observed after growth of the nanoparticles was originated from interparticle coupling of **NP-1** on the surface of **F8K** vesicles.

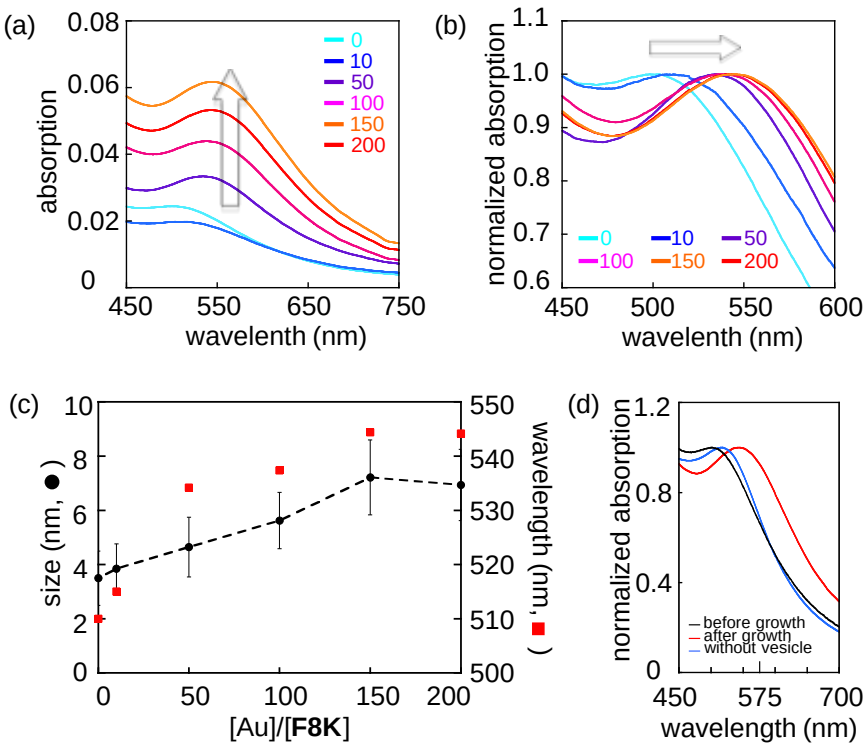

Figure 4-11. Surface plasmon resonance absorption of **NP-1** after *in situ* growth on **F8K** vesicles. (a,b) Absorption spectra and normalized absorption spectra. Numbers show the ratio of gold atoms per fullerene amphiphile. (c) Relationship between size of nanoparticles and absorption maximum of the solution. (d) Absorption spectra of nanoparticles (black line) and conjugates before (red) and after (blue) destruction of the vesicle structure.

4.6 Fusion of vesicles induced by non-cooperative adsorption of gold nanoparticles

The mild interaction between the vesicle surface and the tetra(ethylene oxide) capped-nanoparticle **NP-1**, which produced the unique cooperative adsorption, was found to be the key for the formation of stable 50 nm hybrids. The surface activity of nanoparticles can be regulated by the length of the capping ligands. [24] When nanoparticles coated with a longer (11-

mercaptoundecyl)hexa(ethylene oxide) (**NP-2**) were used, the interaction between the particle and the vesicle was enhanced and the process became isodesmic (Figure 4-12).

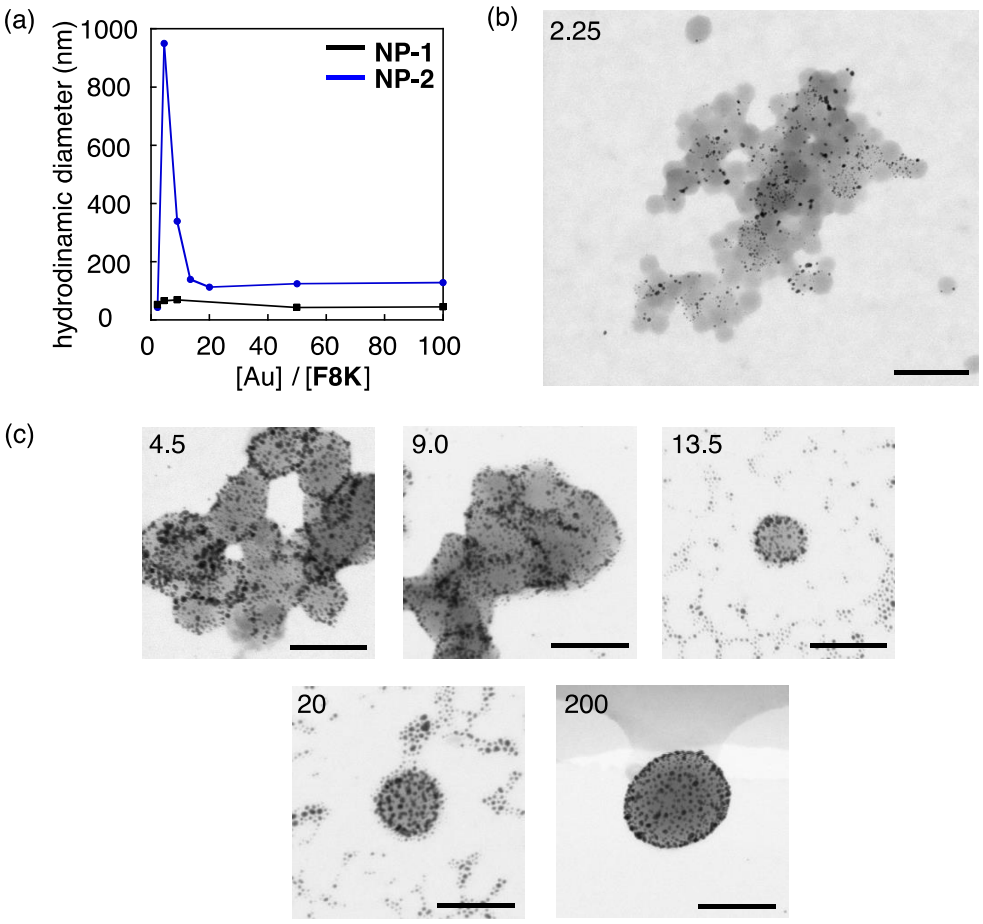

Figure 4-12. Fusion of **F8K** vesicles during the process of isodesmic adsorption of **NP-2**. (a) Hydrodynamic diameter of vesicle and particle assemblies in a cooperative process for **NP-1** (black line) and an isodesmic process for **NP-2** (blue line) measured in water at 25 ºC by DLS. (b,c) STEM images illustrating the isodesmic adsorption of **NP-2** on **F8K** and NP-mediated fusion. The numbers on the top of the images refer to the concentration ratio of gold atoms per fullerene amphiphile. Scale bars are 100 nm.

NP-2 mediated the interaction between vesicles forming large agglomerates (950 nm, DLS, Figure 4-12a,b). By using a large excessive amount of nanoparticles **NP-2,** isolable nanohybrids were obtained after purification using size exclusion chromatography. However, the hydrodynamics radius of the vesicle increased from 30.4 nm to 128 nm. STEM images showed that the introduction of the nanoparticles caused the fusion of vesicles into larger hybrids (Figure 4-12c). The fusion of vesicles was probably induced by

deformation of the vesicle membrane, as a similar phenomenon has been known for lipid vesicles.[8,25]

The results in this section suggest the interaction between the fullerene membrane and metal nanoparticles may be used to control the size of the hybrids via fusion of the vesicle structure.

4.7 Conclusion

In conclusion, decoration of vesicles by interfacial adsorption of OEO-coated gold nanoparticles on the hydrophobic surface of fullerene vesicles in water was demonstrated. The adsorption process can be controlled by the surface substituent on the vesicle surface, which produces an interface in water, and the capping ligands on the gold nanoparticle surface, which regulates the surface activity of the nanoparticles. Vesicle fusion or aggregation that has been previously reported by conjugates prepared via electrostatic interaction did not occur when the nanoparticle adsorption occurred via a cooperative process. The oligo(ethylene oxide) ligand promotes interparticle interaction on the vesicle surface that strongly stabilizes the decorated vesicles under biological conditions. The size of the nanoparticles can be controlled in a seed-and-growth process. The density of the nanoparticles on the vesicle surface was sufficiently high for coupling of the surface plasmon resonance to occur.

The result described in this chapter is another example of the use of the architecture of vesicles made of $R_5C_{60}^-K^+$ amphiphiles. The unique properties of fullerene vesicles together with the plasmonic properties of gold nanoparticles will allow the development of smart materials with potential biological applications.

4.8 Experimental Section

4.8.1 General

All reactions dealing with air- or moisture-sensitive compounds were carried out in a dry reaction vessel under nitrogen or argon. The water content of the solvent was confirmed with a Karl-Fischer Moisture Titrator (MKC-210, Kyoto Electronic Company) to be less than 100 ppm. Distilled water was further deionized with Millipore Milli-Q. Dynamic laser light scattering (DLS) study was carried out on a Malvern Zetasizer Nano ZS machine. Scanning electron microscopy (SEM) and scanning transmission electron microscopy

(STEM) were performed on FEI Magellan 400L equipped with a retractable STEM detector with BF/DF/HAADF segment. The UV-Visible spectra were recorded on a JASCO V-570 UV/VIS/NIR Spectrophotometer. The surface tension was measured in a Kyowa Dropmaster DM-300YC.

4.8.2 Materials

Unless otherwise noted, materials were purchased from Tokyo Kasei Co., Aldrich Inc., and other commercial suppliers and used after appropriate purification before use. Anhydrous ethereal solvents (stabilizer-free) were purchased from WAKO Pure Chemical and purified by a solvent purification system (GlassContour)[26] equipped with columns of activated alumina and supported copper catalyst (Q-5) prior to use. All other solvents were purified by distillation and stored over molecular sieves 4Å. $HAuCl_4 \cdot 4H_2O$ was purchased from Kanto Chemical Co., Inc. and used as received. (11-mercaptoundecyl)hexa(ethylene oxide) and fullerene derivatives **F8K**, **C20K**, **C8K**, and **MeK**, were synthesized by the reported procedures. [11,12,13,27]

4.8.3 Synthesis

Synthesis of gold nanoparticles capped with (11-mercaptoundecyl)tetra (ethylene oxide) (NP-1).

An aqueous solution of $HAuCl_4$ (3.0 mL, 30 mM) was added to a solution of tetraoctylammoniumbromide (219 mg, 0.401 mmol) in toluene (8.0 mL). The toluene phase was collected and reduced by rapid addition of a freshly prepared aqueous solution of $NaBH_4$ (38.7 mg, 1.02 mmol, 0.410 M) under vigorous stirring (vortex). A solution of (11-mercaptoundecyl)tetra(ethylene oxide) (12.4 mg, 32.6 μM) in toluene (4.0 mL) was added to the organic phase, and a black precipitate was formed. The precipitate was dissolved in water (5.0 mL), washed with diethyl ether (3 × 15 mL), and purified by centrifugation (10000 rpm, 30min; then 5000 rpm, 30 min). Dilution with water to 25 mL yielded the aqueous solution of gold nanoparticle capped with (11-mercaptoundecyl)tetra(ethylene oxide). The concentration of the solution was calculated from the amount of starting material as ca. 3.6 mM. The size of the nanoparticle core was determined from STEM images.

The synthesis of gold nanoparticles capped with (11-

mercaptoundecyl)hexa (ethylene oxide) (**NP-2**) was achieved by the same procedure as (11-mercaptoundecyl)tetra(ethylene oxide)-coated nanoparticles.

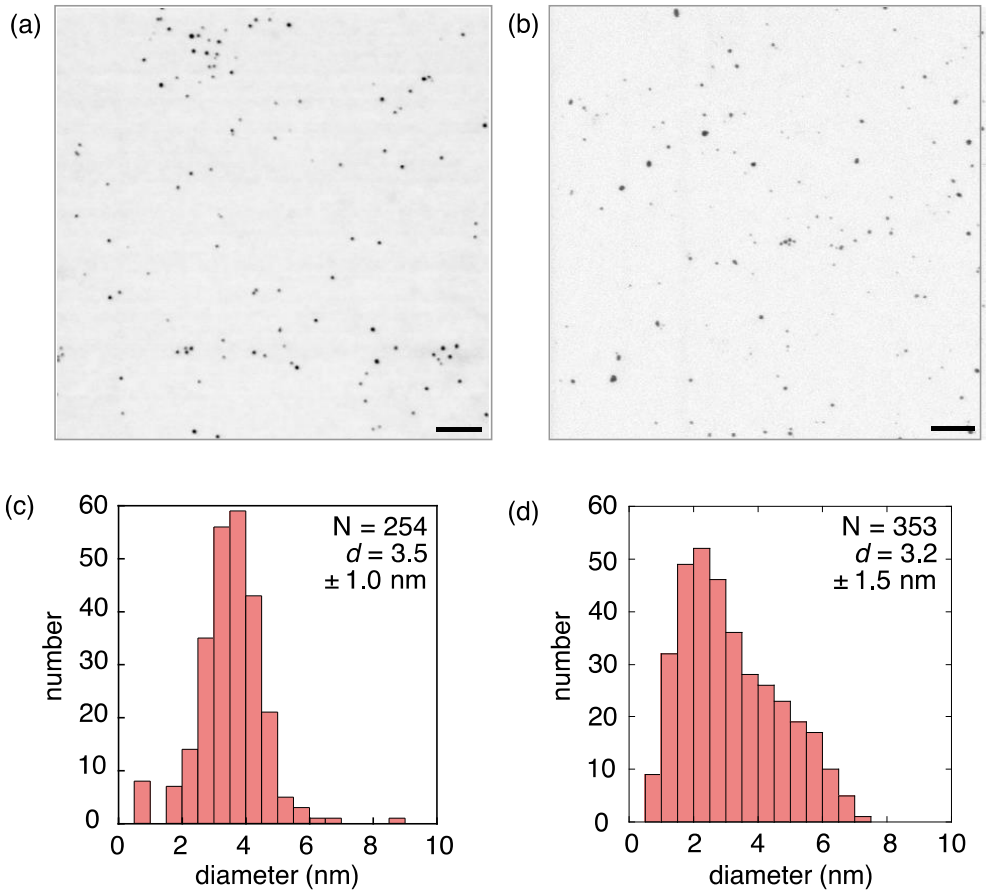

Figure 4-13. Characterization of **NP-1** and **NP-2**. (a,b) Representative STEM images of **NP-1** and **NP-2** on an amorphous carbon film under 10^{-5} Pa. Scale bars are 50 nm. (c,d) Size distribution of the core of **NP-1** and **NP-2** determined from STEM images. Error represents the standard deviation.

4.8.4 Methods

DLS analysis

Dynamic light scattering (DLS) measurement was performed on a Malvern Zetasizer Nano ZS equipped with an He-Ne laser operating at 4 mW power and 633 nm wavelength, and a computer-controlled correlator, at a 173 ^{o} accumulation angle. Measurement was carried out at 25 ^{o}C in a polystyrene or glass cuvette. The data were processed using dispersion technology software version 5.10 to give Z-average particle size and polydispersity index (PdI) value by cumulant analysis, and particle size distribution by CONTIN analysis.

Table 4-1. Hydrodynamic diameter of the fullerene vesicles used in this study determined in water at 25 ºC by DLS. The error represents the standard deviation of three measurements of the same sample.

Vesicle	**F8K**	**C20K**	**C8K**	**MeK**
diameter (nm)	30.4 ± 0.5	29.6 ± 0.4	27.3 ± 0.8	47.1 ± 0.4

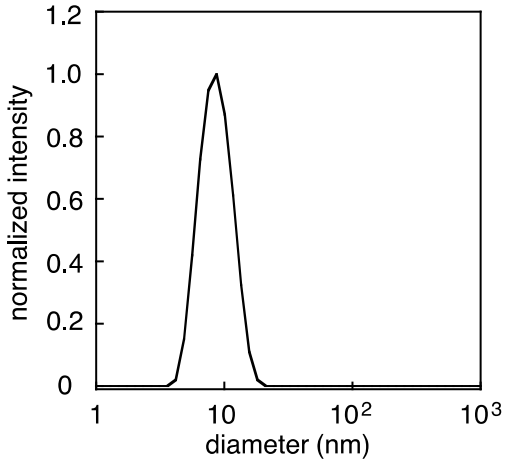

Figure 4-14. Size distribution of **NP-1** (d_{hyd} = 8.2 ± 0.1 nm) determined in water at 25 °C by DLS.

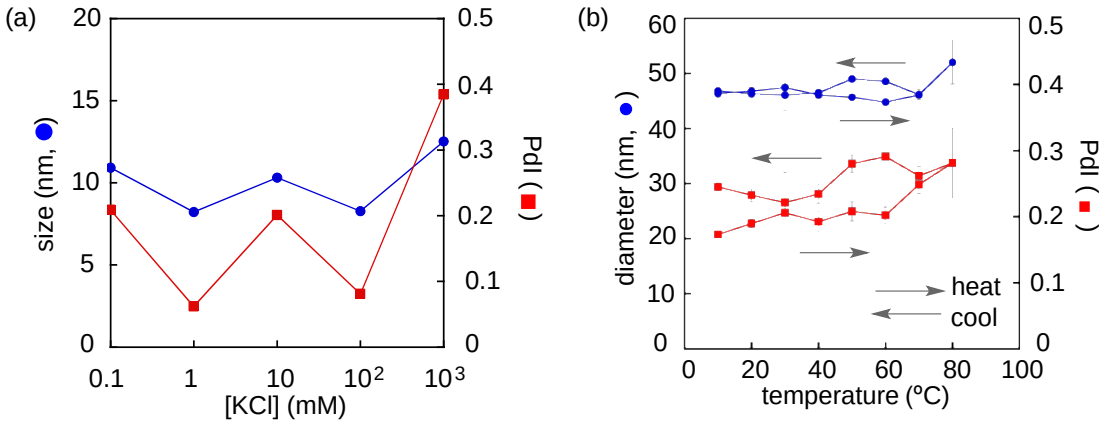

Figure 4-15. (a) The potassium cation did not affect the stability nor mediated the aggregation of **NP-1**. Hydrodynamic diameter (blue circles) and PdI (red squares) of **NP-1** under different concentration of KCl in water. Concentration of gold is 1.0 mM. (b) Thermostability of **F8K** vesicles decorated with **NP-1**. Hydrodynamic diameter (blue line) and PdI (red line). An error bar shows the standard deviation of three measurements.

General procedure for preparation of F8K vesicles decorated with NP-1

62.5 μL of an aqueous solution of **NP-1** ([Au] = ca 3.6 mM) was gently poured into 1.00 mL of an aqueous solution of vesicles of **F8K** (100 μM) in an eppendorf tube under stirring by vortex. After 30 minutes, the mixture was purified by size exclusion chromatography (Sephacryl® S-1000 SF, eluent: 10% ethanol / 90% water) to give the decorated vesicles.

General procedure for *in-situ* growth of gold nanoparticles

An aqueous solution of $HAuCl_4$ (0.59 mM) and K_2CO_3 (1.76 mM) was prepared at least 2 hours prior the experiment. 255 μL of the growth solution was added to 100 μL of **F8K** vesicles decorated with **NP-1** ([**1**] = 100 μM) and stirred for 10 minutes. To this solution, 1.27 mL of 37% formaldehyde was added and stirred for 2 hours at 25 ^{o}C. The growth reaction was terminated by dialysis of the excess reagents though a cellulose tubular membrane (Cellu Sep®) in water (1 L x 3, 12 hours), giving an aqueous solution of vesicles decorated with large gold nanoparticles.

Surface tension measurement

The surface tension γ was measured by the pendant droplet method in a contact angle meter Kyowa Dropmaster DM-300YS. The profile of a 3 μL droplet of an aqueous solution of the substrate was recorded and fitted with the Young-Laplace equation, extracting the value of the surface tension γ. The time evolution of the surface tension γ was measured every one minute for fifteen minutes. The measured was repeated three times and the standard deviation was calculated.

Table 4-2. Surface tension of aqueous solution of NP-1 with vesicles (11 particles per vesicle). Concentration of gold atoms is 0.36 mM and concentration of fullerene anions is 72 μM. Average (left) and standard deviation (right) of three measurements are given as mN m^{-1} (in each column). Time is given as minutes.

time	water (ref.)		**NP-1**		**F8K+NP-1**		**C20K+NP-1**		**C8K+NP-1**		**MeK+NP-1**	
1	71	0.9	51.3	3.5	70.7	0.1	71.6	0.2	70.1	0.5	72.5	0.4
2	71.1	0.6	49.6	2.3	70.3	0.1	71.8	0.1	69.5	0.7	72.1	0.2
3	70	2.4	48.5	1.5	70.4	0.3	71.4	0.5	68.9	0.9	71.4	0.3
4	71.3	0.8	47.7	1.3	70.4	0.1	71.2	0.4	68.9	0.8	70.1	0.6
5	70.8	0.6	47.1	1.2	70.6	0.1	71.0	0.6	68.4	0.9	67.9	2.2
6	70.8	0.4	47.2	0.9	70.6	0.1	71.0	0.5	67.8	1.3	66.1	2.0
7	71.5	0.6	46.5	0.8	70.2	0.3	70.8	0.6	67.0	1.8	63.4	3.5
8	71	0.5	47.3	1.3	70.5	0.4	70.3	1.0	66.3	2.1	59.9	4.8
9	70.7	0.6	47.0	1.0	70.4	0.1	70.0	0.9	65.1	2.2	57.5	4.7
10	69.9	0.5	46.7	0.7	70.6	0.3	69.9	1.5	63.6	2.8	55.4	3.9
11	70.3	1.1	46.8	0.6	70.1	0.1	70.2	0.9	62.3	2.7	53.8	3.3
12	70.9	0.7	46.8	0.8	70.1	0.0	69.9	0.9	60.8	3.0	52.8	3.4
13	70.3	0.7	46.6	0.8	70.3	0.4	69.2	1.0	59.3	3.2	52.0	4.0
14	70.4	1	46.5	0.7	69.9	0.1	69.2	1.6	57.8	2.7	49.8	3.6
15	70.4	0.3	46.0	1.0	70.3	0.3	69.0	1.9	56.0	2.4	50.1	2.8

Table 4-3. Surface tension of aqueous solution of NP-1 with vesicles (22 particles per vesicle). Concentration of gold atoms is 0.36 mM and concentration of fullerene anions is 36 μM. Average (left) and standard deviation (right) of three measurements are given as mN m^{-1} in each column. Time is given as minutes.

time	F8K+NP-1		C20K+NP-1	
1	72.3	0.7	70.2	0.4
2	71.8	0.8	69.5	0.6
3	71.6	0.6	68.8	0.7
4	71.8	0.6	67.8	1.1
5	71.4	0.5	66.2	0.6
6	71.5	0.4	62.4	1.2
7	71.7	0.7	59.8	0.3
8	71.1	0.8	57.7	0.7
9	70.9	0.6	55.8	0.9
10	70.8	0.3	55.1	0.4
11	70.6	0.7	54.6	1.0
12	70.1	0.8	53.6	1.5
13	69.8	0.4	53.0	1.7
14	69.2	0.5	52.4	2.1
15	68.7	0.4	52.5	1.9

Sample preparation for simultaneous SEM/STEM analysis

The aqueous solution of decorated vesicles (2 μL, 1 μM) was put on a transmission electron microscopy (TEM) copper mesh coated with carbon film (Super Ultra High Resolution Carbon film, thickness < 6 nm, Oken Shoji Co., Ltd.); then dried under reduced pressure (10^{-2} Pa) at room temperature for several hours prior to measure.

Procedure for simultaneous SEM/STEM observation

Simultaneous SEM/STEM observation was performed on a FEI Magellan 400L instrument at 5 x 10^{-5} Pa by using a retractable STEM detector with BF/DF/HAADF segment. The working distance was set to 4.0 mm. Secondary electrons were collected with a through-lens detector. Observation was performed at beam landing voltage of 25 kV and electron beam current of

0.80 nA.

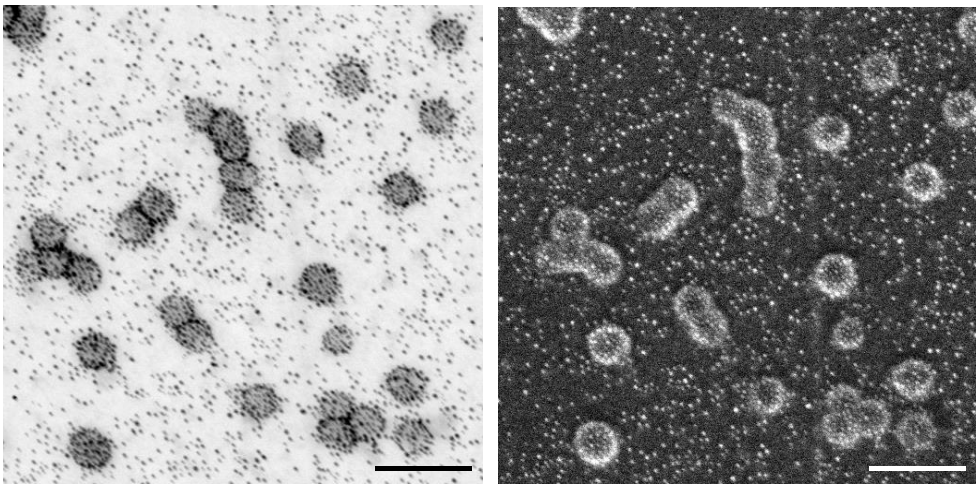

Figure 4-16. STEM and SEM images of **NP-1** and **F8K** vesicles before removal of the excess amount of nanoparticles by gel filtration. Notice that the nanoparticles do not seem to form bilayers on the vesicle surface, neither promote interaction between vesicles. Scale bars are 100 nm.

Sample preparation for high-resolution SEM

0.1 mL of decorated vesicle solution (10 μM) was deposited on the surface of an IZO/glass substrate treated by UV/O_3 and spin coated at 500 rpm for 3 s and 1500 rpm for 30 s. The sample was dried under reduced pressure (10^{-2} Pa) at room temperature for several hours prior to measurent.

Procedure for high-resolution SEM observation

SEM observation was performed on a FEI Magellan 400L instrument at 5 x 10^{-5} Pa. The working distance was set to 2.1 mm. Secondary electrons were collected with a through-lens detector. Observation at a beam landing voltage of 8.0 kV and current of 0.40 nA was performed.

Procedure for NMR experiment

A solution of gold nanoparticles **NP-1** in D_2O ([Au] = ca. 6.0 mM; 167, 167, 334, or 334 μL) was added to a solution of **F8K** in D_2O ([**F8K**] = 0.73 mM; 302, 156, 156, or 78 μL). The mixture was diluted with D_2O up to a total volume of 0.50 mL and transferred to an NMR tube. A capillary tube containing a solution of deuterated (3-(trimethylsilyl)-2,2',3,3'-tetradeuteropropionic acid

(TMSP-d_4) in D_2O (20 μL, 0.25 mM) was introduced prior the measurement as an external standard.

Reduction reaction of *p*-nitrophenol catalyzed by gold nanoparticles

A freshly prepared aqueous solution of sodium borohydride (1.0 mL, 100 mM) was added to a solution of *p*-nitrophenol (2.0 mL, 0.100 mM) in a UV cell. An aqueous solution of gold catalyst (20 mol%, calculated based on the amount of gold salt used in the preparation of the nanoparticles) was added under stirring to the cell in the UV-Vis spectrometer at 25 or 60 ^{o}C. Time-dependent absorption at a wavelength of 400 nm was measured to monitor the reaction.

4.9 References

[1] Jain, P. K., Huang, X., El-Sayed, I. H. & El-Sayed, M. A. Noble metals on the nanoscale: optical and photothermal properties and some applications in imaging, sensing, biology, and medicine. *Acc. Chem. Res.* **41**, 1578–1586 (2008).

[2] Wu, G., Mikhailovsky, A., Khant, H. A., Fu, C., Chiu, W. & Zasadzinski, J. A. Remotely triggered liposome release by near-infrared light absorption via hollow gold nanoshells. *J. Am. Chem. Soc.* **130**, 8175–8177 (2008).

[3] Mart, R. J., Liem, K. P. & Webb, S. Creating functional vesicle assemblies from vesicles and nanoparticles. *J. Pharm. Res.* **26**, 1701–1710 (2009).

[4] Leung, S. J. & Romanowski, M. Light-activated content release from liposomes. *Theranostics* **2**, 1020–1036 (2012).

[5] Jackson, J. B. & Halas, N. J. Surface-enhanced Raman scattering on tunable plasmonic nanoparticle substrates. *Proc. Natl. Acad. Sci. USA* **101**, 17930–17935 (2004).

[6] Song, J., Zhou, J. & Duan, H. Self-assembled plasmonic vesicles of SERS-encoded amphiphilic gold nanoparticles for cancer cell targeting and traceable intracellular drug delivery. *J. Am. Chem. Soc.* **134**, 13458–13469 (2012).

[7] Niikura, K., Iyo, N., Higushi, T., Nishio, T., Jinnai, H., Fujitani, N. & Ijiro, K. Gold nanoparticles coated with semi-fluorinated oligo(ethylene glycol) produce sub-100 nm nanoparticle vesicles without templates. *J. Am. Chem. Soc.* **134**, 7632–7635 (2012).

[8] Michel, R. & Gradzielski, M. Experimental aspects of colloidal interactions in mixed systems of liposome and inorganic nanoparticle and their applications. *Int. J. Mol. Sci.* **13**, 11610–11642 (2012).

[9] Volodkin, D. V., Skirtach, A. G. & Möhwald, H. Near-IR remote release from assemblies of liposomes and nanoparticles. *Angew. Chem. Int. Ed.* **2009**, *48*, 1807–1809.
[10] Zhang, L. & Granick, S. How to stabilize phospholipid liposomes (using nanoparticles). *Nano Lett.* **6**, 694–698 (2006).
[11] Homma, T., Harano, K., Isobe, H. & Nakamura, E. Nanometer-size fluorous fullerene vesicles in water and on solid surfaces. *Angew. Chem. Int. Ed.* **49**, 1665 (2010).
[12] Homma, T., Harano, K., Isobe, H. & Nakamura, E. Preparation and Properties of Vesicles Made of Nonpolar/Polar/Nonpolar Fullerene Amphiphiles. *J. Am. Chem. Soc.* **133**, 6364–6370 (2011).
[13] Burger, C., Hao, J., Ying, Q., Isobe, H., Sawamura, M., Nakamura, E. & Chu, B. Multilayer vesicles and vesicle clusters formed by the fullerene-based surfactant $C_{60}(CH_3)_5K$. *J. Colloid Interface S.* **275**, 632–641 (2004).
[14] Glogowski, E., Tangirala, R., He, J., Russel, T. P. & Emrick, T. Microcapsules of PEGylated gold nanoparticles prepared by fluid−fluid interfacial assembly. *Nano Lett.* **7**, 389–393 (2007).
[15] Simpson, C. A., Huffman, B. J., Gerdon, A. R. & Cliffel, D. E. Unexpected toxicity of monolayer protected gold clusters eliminated by PEG-thiol place exchange reactions. *Chem. Res. Toxicol.* **23**, 1608–1616 (2003).
[16] Alkilany, A. M. & Murphy, C. J. Toxicity and cellular uptake of gold nanoparticles: what we have learned so far? *J. Nanopart. Res.* **12**, 2131–2333 (2010).
[17] Brust, M., Bethell, D., Schiffrin, D. J. & Kiely, C. J. Novel gold-dithiol nano-networks with non-metallic electronic properties. *Adv. Mater.* **7**, 795–797 (1995).
[18] Kanaras, A. G., Kamounah, F. S., Schaumburg, K., Kiely, C. J. & Brust, M. Thioalkylated tetraethylene glycol: a new ligand for water soluble monolayer protected gold clusters. *Chem. Commun.* **2002**, 2294–2295.
[19] Harano, K., Yamada, J., Mizuno, S. & Nakamura, E. High-density display of protein ligands on self-assembled capsules via noncovalent fluorous interactions. *Chem. Asian. J.* in press (2014). DOI: 10.1002/asia.201403144.
[20] Isa, L., Calzolari, D. C. E., Pontoni, D., Gillich, T., Nelson, A., Zirbs, R., Sánchez-Ferrer, A., Mezzenga, R. & Reimhult, E. Core–shell nanoparticle monolayers at planar liquid–liquid interfaces: effects of polymer architecture on the interface microstructure. *Soft Matter* **9**, 3789–3797 (2013).
[21] Hervés, P., Pérez-Lorenzo, M., Liz-Marzán, L. M., Dzubiella, J., Lu, Y. & Ballauff, M. Catalysis by metallic nanoparticles in aqueous solution: model reactions. *Chem. Soc. Rev.* **41**, 5577–5587 (2012).
[22] Wang, X., Wang, C., Cheng, L., Lee, S.–T. & Liu, Z. Noble metal coated single-walled carbon nanotubes for applications in surface enhanced raman scattering imaging and photothermal therapy. *J. Am. Chem. Soc.* **134**, 7414–7422 (2012).

[23] Nguyen, N. D., Dang, V. P., Le, A. Q. & Nguyen, Q. H. Electron beam/γ-ray irradiation synthesis of gold nanoparticles and investigation of antioxidant activity. *Adv. Nat. Sci.* **5**, 045002 (2014).
[24] Isa, L., Amstad, E., Schwenke, K., Del Gado, E., Ilg, P., Kröger, M. & Reimhult, E. Adsorption of core-shell nanoparticles at liquid–liquid interfaces. *Soft Matter* **7**, 7663–7665 (2011).
[25] Harano, K., Narita, A. & Nakamura, E. Photo-cross-linking of exterior of fullerene bilayer that prevents vesicle aggregation. *Chem. Lett.* **43**, 877–879 (2014).
[26] Pangborn, A. B., Giardello, M. A., Grubbs, R. H., Rosen, R. K. & Timmers, F. J. Safe and convenient procedure for solvent purification. *Organometallics* **15**, 1518–1520 (1996).
[27] Chou, S. S., De, M., Kim, D., Byun, S., Dykstra, C., Yu, J., Huang, J. & Dravid, V. P. Ligand Conjugation of Chemically Exfoliated MoS_2. *J. Am. Chem. Soc.* **135**, 4584–4587 (2013).

— Chapter 5 —

Observation of dynamic conformational changes of single organic molecules on a carbon nanohorn under low-acceleration voltage TEM

5.1 Introduction: Experimental observation of the dynamics of single organic molecules

Unveiling of the dynamics of organic molecules at atomic resolution is fundamental to deepen our understanding of molecular functions and its relationship to macroscopic phenomena. Simulation studies have been the main tool for investigation of molecular dynamics as the environmental conditions can be precisely controlled;[1] only in recent years, microscopy techniques have improved so that we can experimentally observe the motion of single organic molecules in near-atomic resolution. For instance, scanning tunneling microscopy (STM) was used to simultaneously monitor and drive the motion of small organic molecules in metal substrates.[2,3,4] However, the high complexity of STM imaging and the limited target scope (e.g. molecules of high planarity) have impeded its application for prospect biological molecules, which are the main subject of molecular dynamic studies.

On the other hand, transmission electron microscopy (TEM) has been long used as a tool for characterization of inorganic and organic crystals at near-atomic resolution, and is familiar to scientists of diverse fields, including biology. For a long time, it was believed that the conditions for high resolution TEM observation would damage organic molecules,[5] making the observation of single molecule dynamics impossible. Contrary to common belief, Nakamura *et al.* succeeded in monitoring single organic molecules by using an observation technique named single-molecule and real-time TEM (SMART-TEM).[6,7] In SMART-TEM, the observation of organic molecules is made possible by encapsulation or attachment of the specimen molecule to a carbon cluster, that acts as an single-atom thin substrate. Consecutive acquiring of TEM images allows the observation of conformational changes[8,9] and reactions[10,11] of small organic molecules as TEM movies. However, the movies themselves are an insufficient tool for in-depth studies of molecular conformations in the absence of a method to change and to quantify the magnitude and the frequency of the molecular motions.

In this chapter, it is described that the overall motion of organic molecules attached to the edge of carbon nanohorns observed in a TEM movie is a result of the interaction with inelastic scattered electrons, which can be regulated by the acceleration voltage of the electron beam, and the interaction

between nanotube and single molecule. The irradiation of the sample with electrons of low energy at a low acceleration voltage (60 or 80 kV) accelerates the dynamics of biotinylated molecules (e.g. rotation and isomerization of an amide bond) without causing damage to the molecule or the nanocarbon substrate (Figure 5-1a). Quantitative comparison via cross correlation of the TEM movies of molecules **1–3**, which were attached to the nanohorn by different linkers, showed that the molecular design also affects the dynamics of the molecules (Figure 5-1b). Cross-correlation analysis was also shown to be useful for computer-aided structural identification of the conformer seen in each frame of the molecular movie. The phenomenon found by this study, together with further improvement of the resolution and data acquisition time of TEM, will contribute for the understanding of the dynamics of more complex organic molecules, such as proteins.

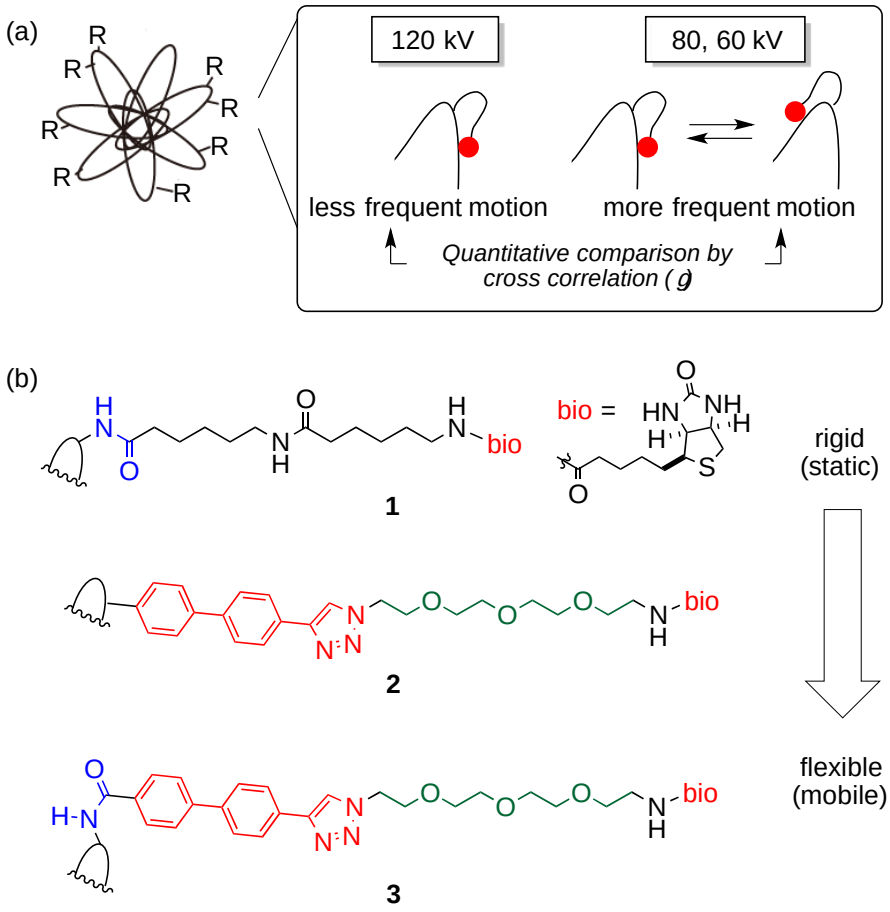

Figure 5-1. Biotinylated molecules **1–3** on a carbon nanohorn. (a) Molecular motion accelerated under low acceleration voltage in TEM measurement. (b) Molecular designs.

5.2 Effect of acceleration voltage in the dynamics of single molecules in TEM observation

Although the temperature dependence is a standard protocol of conformational research, the system under the TEM conditions was reported to be unusually insensitive to temperature (between 4 K[12] and 793 K[11]). Therefore, I considered other parameters to control the frequency of the conformational changes of the specimen molecule. During TEM observation, the sample is irradiated by electrons of energy proportional to the acceleration voltage. Since molecules interact with electrons in a different manner depending on their energy (e.g. energy dependence on the cross-section of inelastic and elastic electron scattering), single organic molecules are expected to behave differently when irradiated with electrons of different energy.

Carbon nanohorn aggregates modified with rather inflexible biotinylated triamide molecules, compound **1**, previously reported by Nakamura *et al.* on the imaging of conformational changes (Figure 1-12)[9], was chosen as a model molecule. A dispersion of **1** in water was deposited on a TEM grid and submitted to measurement after drying. The TEM movies were obtained by consecutive image acquiring at 298 K and electron dose rates in the order of 10^4 – 10^6 e^- nm^{-2} s^{-1}. Each image was obtained after 0.40 s irradiation of the sample with a 0.25 s interval between measurements. In this study, compound **1** was observed at an acceleration voltage of 80 and 60 kV for ca. 1 minute to complement the data reported for 120 kV by Nakamura.

At 80 kV, **1** underwent small conformational changes (Figure 5-2) very similar to the ones observed at 120 kV. The contrast of the TEM image at a lower acceleration voltage was considerably improved due to an increase in the cross-section of inelastic electron scattering.[13] The resolution did not seem to be affected, as would be expected, since the small conformational changes of the molecule slightly blurs the image, making observation at the machine's best resolution difficult even at 120 kV. The position of the terminal biotin group did not change significantly (Figure 5-2, yellow arrows) after irradiation of a total dose of 1.2×10^9 e^- nm^{-2}.

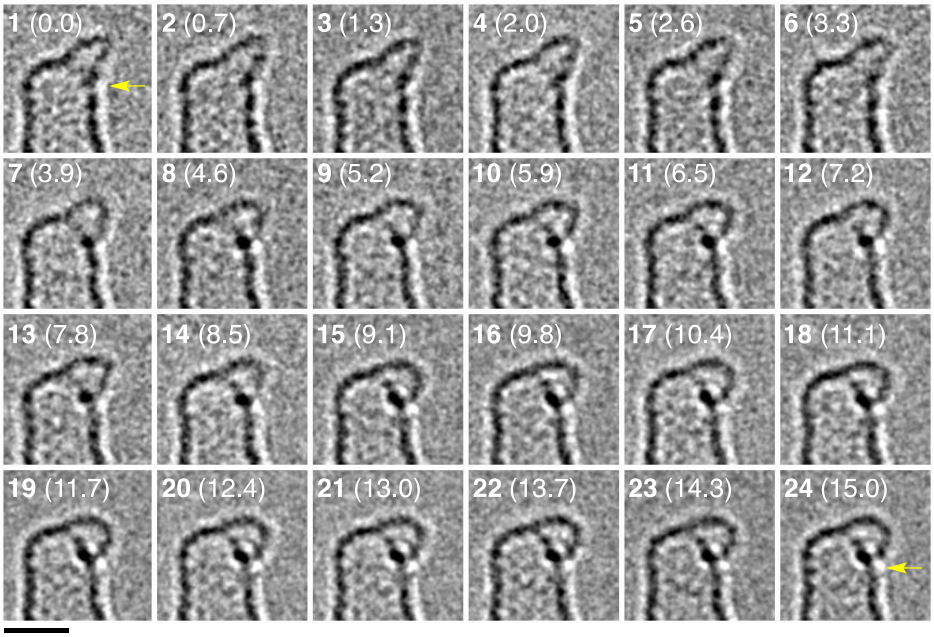

Figure 5-2. Slow dynamics of molecule **1** observed by TEM under an acceleration voltage of 80 kV and electron dose rate of 1.3 x 10^6 e^- nm^{-2} s^{-1}. The position of the terminal biotin, determined as the end of the molecule that moves, is shown by yellow arrows. Scale bars are 1 nm. The numbers refer to the frame number in the movie. Time is shown inside the parenthesis in seconds.

On the other hand, at 60 kV the conformational changes were more significant and the terminal biotin moved over a distance of ca. 1.6 nm on the nanohorn surface after irradiation of 3.6 x 10^5 e^- nm^{-2} (Figure 5-3a). The faster dynamics of **1** at 60 kV is better exemplified by the movie in Figure 5-3b, because the single molecule does not overlap with the carbon nanohorn. Up to frame 21 of this movie, the position of the terminal biotin does not change too much, but the conformation of the linker between carbon nanohorn and biotin changes frequently. From frame 22 up to 30, the terminal biotin moves ca. 2.2 nm on the surface of the carbon nanohorn.

At 60 kV, the contrast of the TEM images was further enhanced at the cost of image resolution. At this deteriorated resolution, the determination of plausible conformations for the single molecules is challenging. As an attempt to accelerate the conformational changes of single molecules observed by TEM at higher acceleration voltages, other molecular designs for biotinylated molecules were considered.

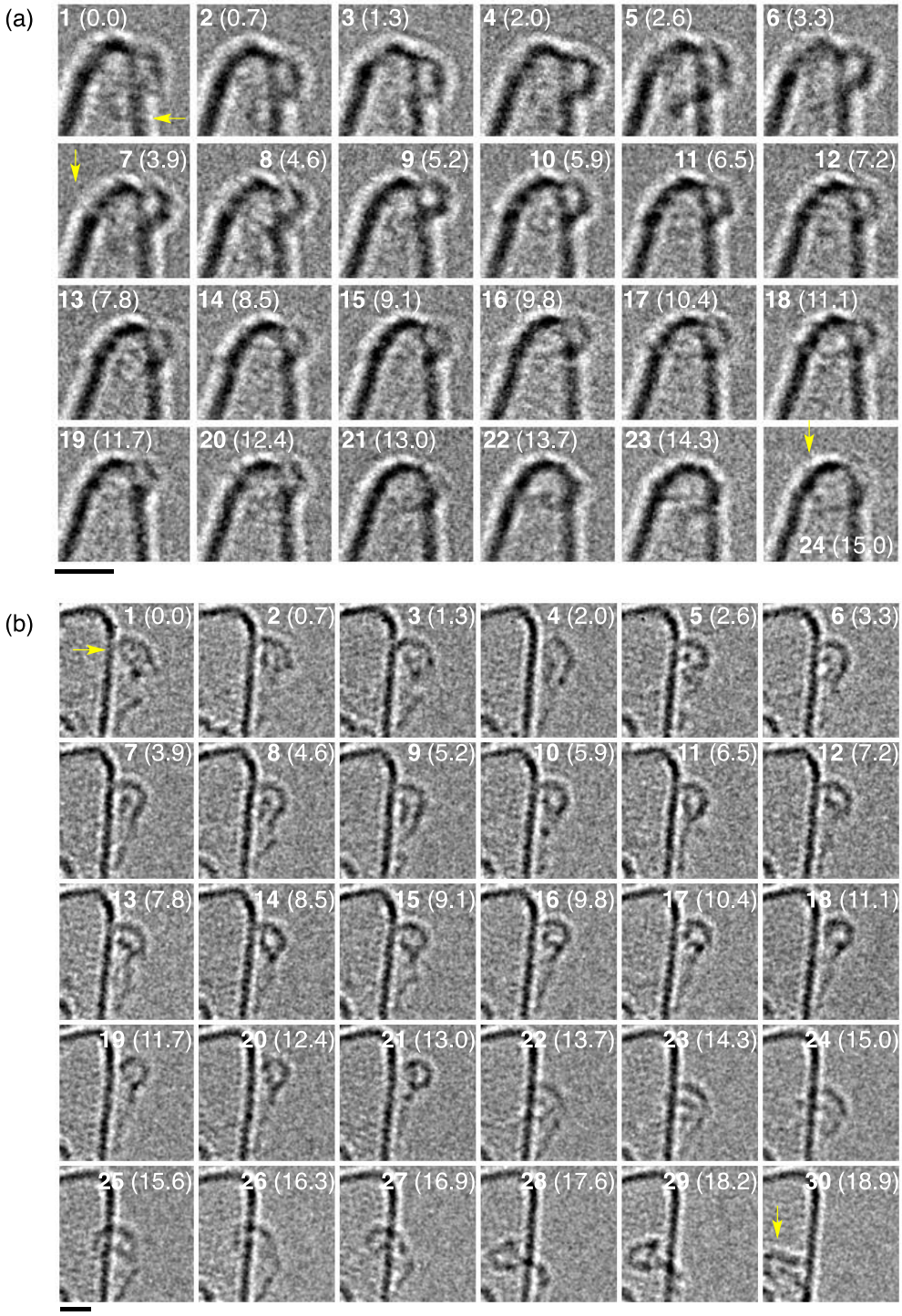

Figure 5-3. Accelerated conformational changes of biotinylated molecule **1** under an acceleration voltage of 60 kV and electron dose rate of 1.5 x 10^4 e^- nm^{-2} s^{-1}. Movies of two different molecules are shown. The position of the terminal biotin is shown by yellow arrows. Scale bars are 1 nm. The numbers refer to the frame number in the movie. Time is shown inside the parenthesis in seconds.

Molecules **2** and **3** were designed to become more complex in their mode of motion (Figure 5-1b). In these molecules, rigid biphenyl and flexible

oligoethylene oxide were introduced in the place of the triamide spacer between the nanohorn and the terminal biotin to induce characteristic dynamics that should be easier to identify. Biphenyl was introduced as a rigid moiety with the intention of decreasing the contact between the nanohorn surface and the biotinylated molecule. In **2**, the molecule was attached directly to the nanohorn and in **3**, via an amide bond. The synthesis was achieved by adapted procedures from the literature (details in section 5.8).[14]

Both molecules showed only small conformational changes at 120 kV, as molecule **1** (Figure 5-4d,f). While the dynamics of **2** at 80 kV were similar to the dynamics of **1** (Figure 5-4e), the dynamics of **3** was much more complex and large conformational changes were observed (Figure 5-4g, vide infra).

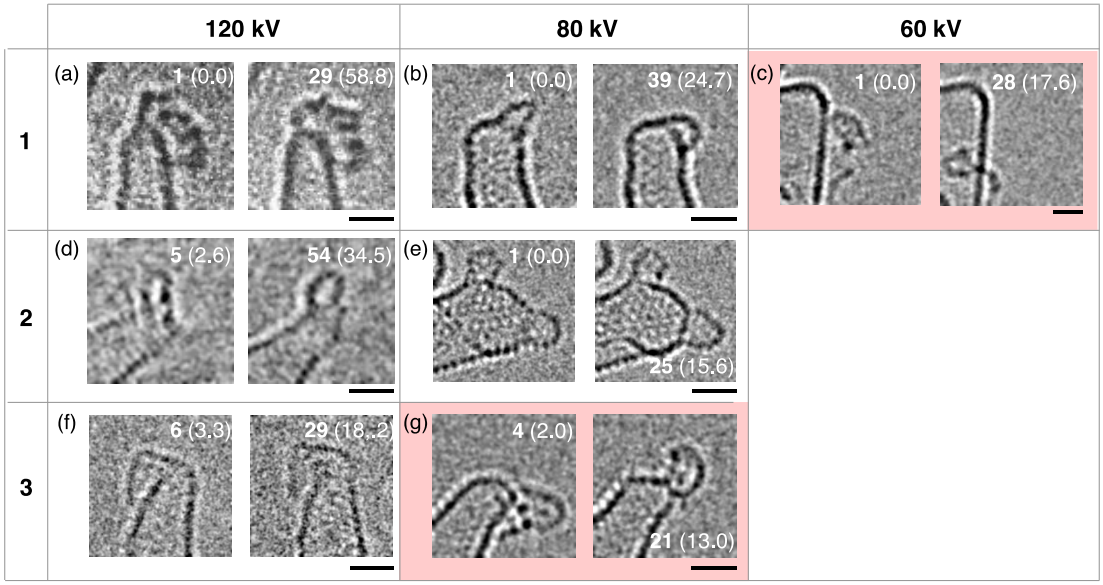

Figure 5-4. Representative frames of TEM movies of biotinylated molecules **1**–**3** obtained under different acceleration voltages. (a-c) Molecule **1** at (a) 120, (b) 80, and (c) 60 kV. (d,e) Molecule **2** at (d) 120 and (e) 80 kV. (f,g) Molecule **3** at (f) 120 and (g) 80 kV. Scale bars are 1 nm. The numbers refer to the frame number in the movie. Time is shown inside the parenthesis in seconds. Note that the images in d and f were obtained at a condition of overfocus and the contrast was inverted for an easier comparison with the other images, which were obtained at a condition of underfocus.

5.3 Quantitative analysis of single molecule dynamics by calculation of the cross correlation between TEM images

The overall motion of the molecules in TEM movies was analyzed in more details by quantification of image change via a cross correlation method, previously reported by Zewail *et al.* in the analysis of 4D TEM data.[15,16] The

cross correlation, $\gamma(t,t')$ in Equation 5-1, was calculated from frames t and t', where $I_t(r_{ij})$ and $I_{t'}(r_{ij})$ are the intensity of pixel (*ij*) in frame *t* and *t'*, and $\overline{I_t}$ and $\overline{I_{t'}}$ are the mean of $I_t(r_{ij})$ and $I_{t'}(r_{ij})$, and represents the matching between these two frames as a number between 1 and –1, being 1 for perfect match and 0 for no match. A factor calculated between the first frame of the movie and all subsequent ones, γ_1 (t = 1), provided information about the accumulated changes on the conformation of the molecule during the movie. Another factor calculated between every two consecutive frames, γ_2 (t' = t + 1), provided information on the small conformational changes between consecutive frames, and these changes were summarized by its average, $\overline{\gamma_2}$.

$$\gamma(t,t') = \frac{\sum_{ij}^{N}\left[I_t(r_{ij}) - \overline{I_t}\right]\cdot\left[I_{t'}(r_{ij}) - \overline{I_{t'}}\right]}{\sqrt{\sum_{ij}^{N}\left[I_t(r_{ij}) - \overline{I_t}\right]^2}\cdot\sqrt{\sum_{ij}^{N}\left[I_{t'}(r_{ij}) - \overline{I_{t'}}\right]^2}} \quad \text{(Equation 5-1)}$$

Prior the analysis, the TEM images were carefully aligned using the nanohorn structure as a reference. The images were equally treated in an image software with a bandpass filter to improve the signal to noise ratio. Samples where the terminal biotin did not overlap with the carbon nanohorn were chosen. To simplify the calculation and obtain meaningful data on the motion of the single molecules, the part of the movie where the terminal biotin appeared not to move on the nanohorn surface was analyzed. As an example, cross correlation of the TEM movie of **1** at 60 kV is shown Figure 5-5. The methods for calculation of cross correlation are shown schematically in Figure 5-5a. The part of the image used in the calculation is shown in Figure 5-5b by black and red rectangles and the sequence of images is shown in Figure 5-5d. Note that for both calculation methods, the cross correlation calculated based on the carbon nanohorn region was constant and close to 1 (Figure 5-5c, black line), while the one calculated based on the biotinylated molecule showed larger variation and was much smaller than 1 (Figure 5-5c, red).

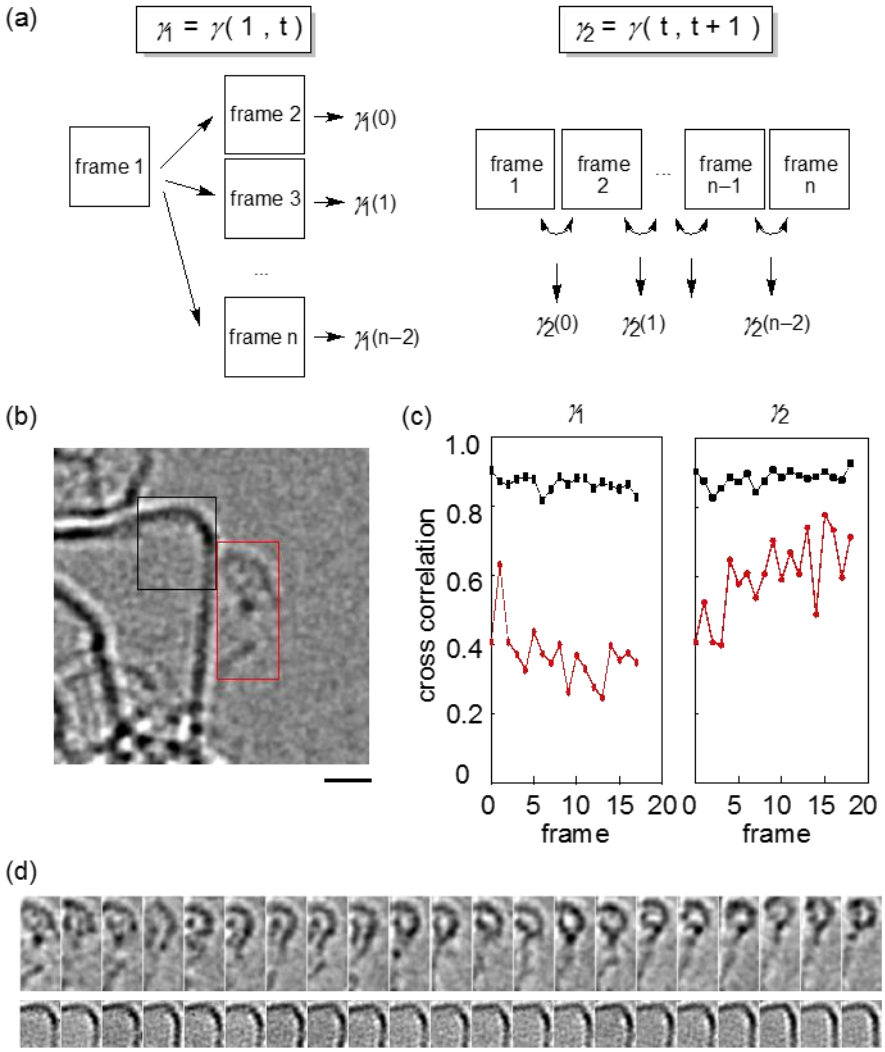

Figure 5-5. Quantitative analysis of TEM movie of molecule **1** at 60 kV by cross correlation. (a) Schematic image of methods for calculation of cross correlation. (b) TEM image of frame 1 showing the parts of the image used for calculation of the cross correlation. The black rectangle shows the carbon nanohorn and the red rectangle shows the biotinylated molecule. Scale bar is 1 nm. (c) Cross correlation γ_1 and γ_2 calculated from carbon nanohorn (black line) and biotinylated molecule **1** (red line). (d) Sequential images of the specimen molecule (top) and carbon nanohorn (bottom).

The summary of the cross correlation analysis is shown in Figure 5-6. Analysis of the TEM movies of **1** by calculation of the cross correlations confirmed the preliminary conclusion that electron irradiation at a lower acceleration voltage accelerates the conformational changes (Figure 5-6). Factor γ_1 shows that the value of cross correlation is very sensitive even for small changes in the TEM image (Figure 5-6a, left). At 120 kV, γ_1 gradually decreased up to 0.24 after 20 frames. At 80 or 60 kV, the decrease was more abrupt, suggesting larger conformational changes in a shorter timeframe.

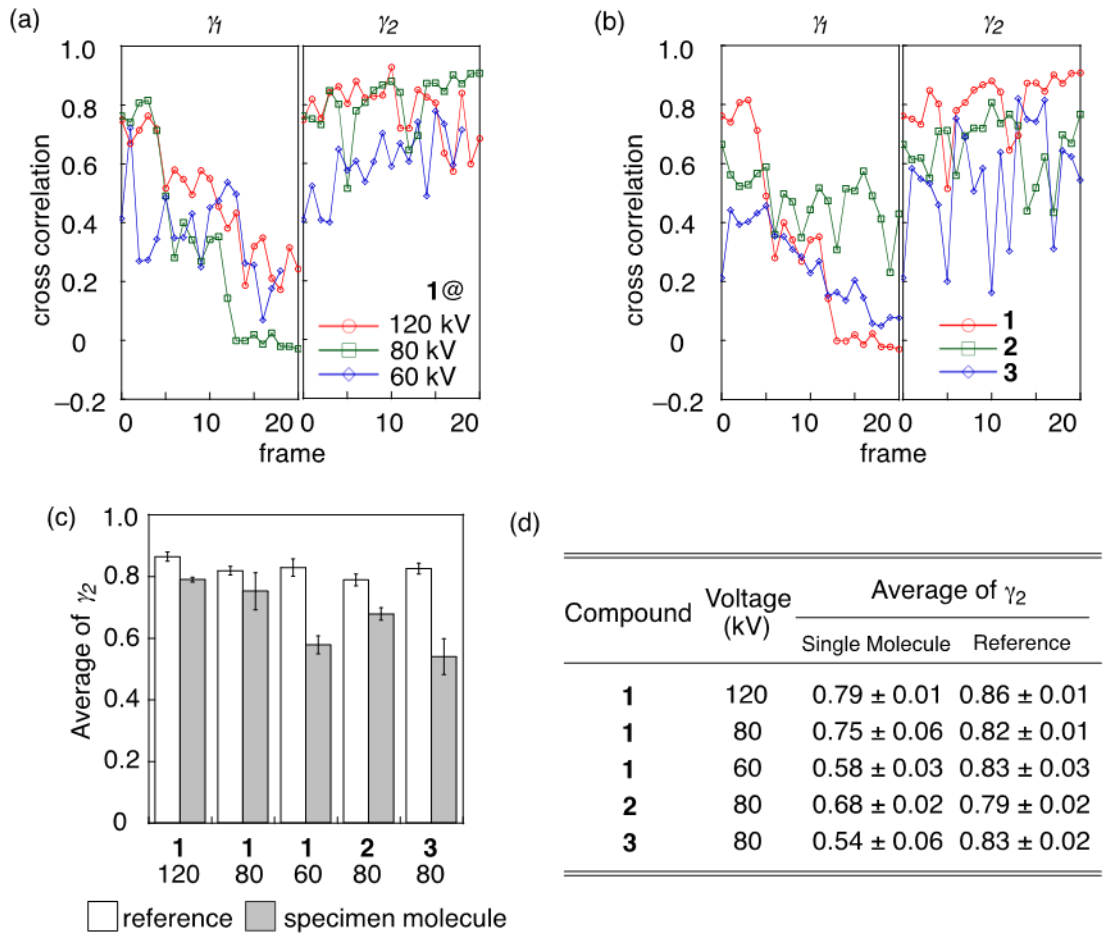

Compound	Voltage (kV)	Average of γ_2	
		Single Molecule	Reference
1	120	0.79 ± 0.01	0.86 ± 0.01
1	80	0.75 ± 0.06	0.82 ± 0.01
1	60	0.58 ± 0.03	0.83 ± 0.03
2	80	0.68 ± 0.02	0.79 ± 0.02
3	80	0.54 ± 0.06	0.83 ± 0.02

Figure 5-6. Quantitative analysis of the conformational changes of biotinylated molecules **1**–**3**. (a) Cross correlation γ_1 and γ_2 calculated from the TEM movie of **1** under an acceleration voltage of 120 (red line), 80 (green) and 60 kV (blue). (b) Cross correlation factor γ_1 and γ_2 of the TEM movie of **1**–**3** measured at 80 kV. (c,d) Average of γ_2, of TEM movies of molecules **1**–**3** obtained under different conditions. The value calculated from the carbon nanohorn part of the molecule is shown as a reference. Standard error of three samples is shown.

Factor γ_2 was clearly smaller at 60 kV than at 80 or 120 kV (Figure 5-6a, right). The cross correlation average $\overline{\gamma_2}$ is lower at 60 kV (0.58 ± 0.03) than at 80 (0.75 ± 0.06) or 120 kV (0.79 ± 0.01) (Figure 5-6c,d). This result supports the existence of a relationship between the degree of conformational changes of single molecules and acceleration voltage in TEM. Furthermore, similar $\overline{\gamma_2}$ at 80 and 120 kV suggests that there is an acceleration voltage threshold for the acceleration of molecular dynamics, which is expectable since other molecular events in TEM observation also have thresholds (e.g. displacement of carbon atoms in graphene occurs at acceleration voltages of 86 kV or higher) [17]. Note that γ_1 and γ_2 calculated from the carbon nanohorn part of the images was constant and did no depend on the acceleration voltage (Figure 5-6c,d; column

reference).

Cross correlation γ_1 shows that **1** and **3** present similar overall changes in TEM movies (Figure 5-6b). On the other hand, γ_2 and $\overline{\gamma_2}$ show that the changes between two consecutive frames are more significant in the order of **3** (0.54 ± 0.06), **2** (0.68 ± 0.02) and **1** (0.75 ± 0.06) under 80 kV (Fig. 3b,c). Therefore, the dynamics observed in TEM observation also depends on the design of the molecules.

5.4 Analysis of the dynamics of the biotinylated molecule 3 by TEM

To understand the origin of the conformation changes observed by TEM, the movie of molecule **3**, which showed the most significant conformational changes, was further investigated. A TEM movie of 100 frames and length of 40 seconds (Figure 5-7 and Figure 5-8) was analyzed. The total electron dose was 1.0 x 10^8 e^- nm^{-2}. Conformational changes occurred in two moments in particular, frame 50 and 85, and the movie was divided in three parts. In the first part, frames 1 to 49, the molecule is mainly located in the right side of the nanohorn (Figure 5-7). The conformation of **3** at the first few frames of the movie is very similar to the one observed at 120 kV (Figure 5-4f). In the second part, frames 50 to 84, the molecule suddenly moves to the left side of the nanohorn (Figure 5-8, top). Such conformational change would only be allowed by the rotation of a *cis*-amide bond. In the last part, frames 85 to 100, the molecule becomes perpendicular to the nanohorn edge during frame 85 and then is mainly located above the center region of the horn edge (Figure 5-8, bottom). During each phase, small conformational changes between every frame were also observed. The dynamic profile described here is in agreement with the molecular design of **3**, where the combination of rigid and flexible spacers produced a motion of two different time scales.

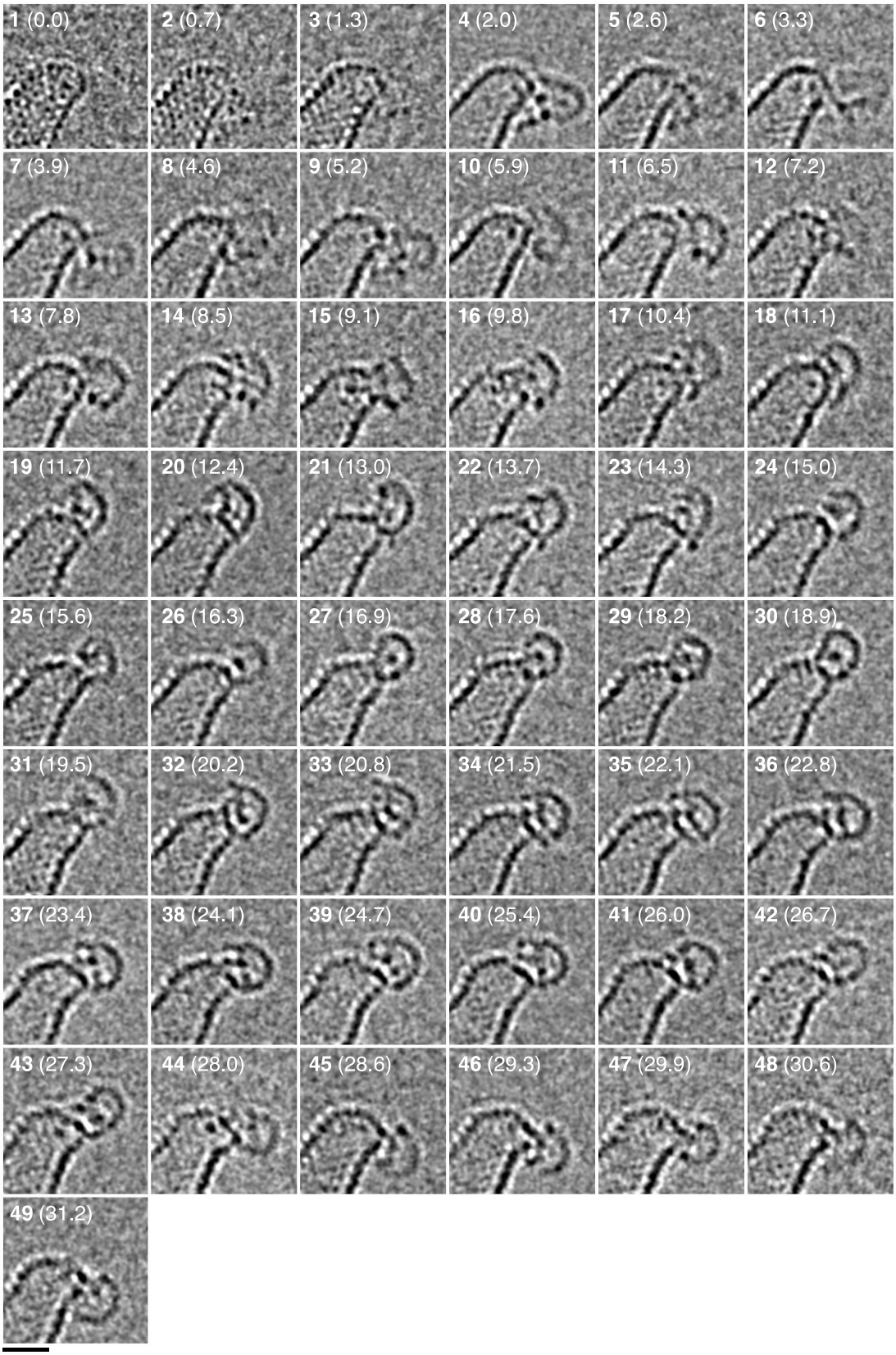

Figure 5-7. Conformational changes of biotinylated molecule **3** under an acceleration voltage of 80 kV and electron dose rate of 2.53 x 10^6 e^- nm^{-2} s^{-1} (frames 1 to 49). Scale bar is 1 nm. The numbers refer to the frame number in the movie. Time is shown inside the parenthesis in seconds.

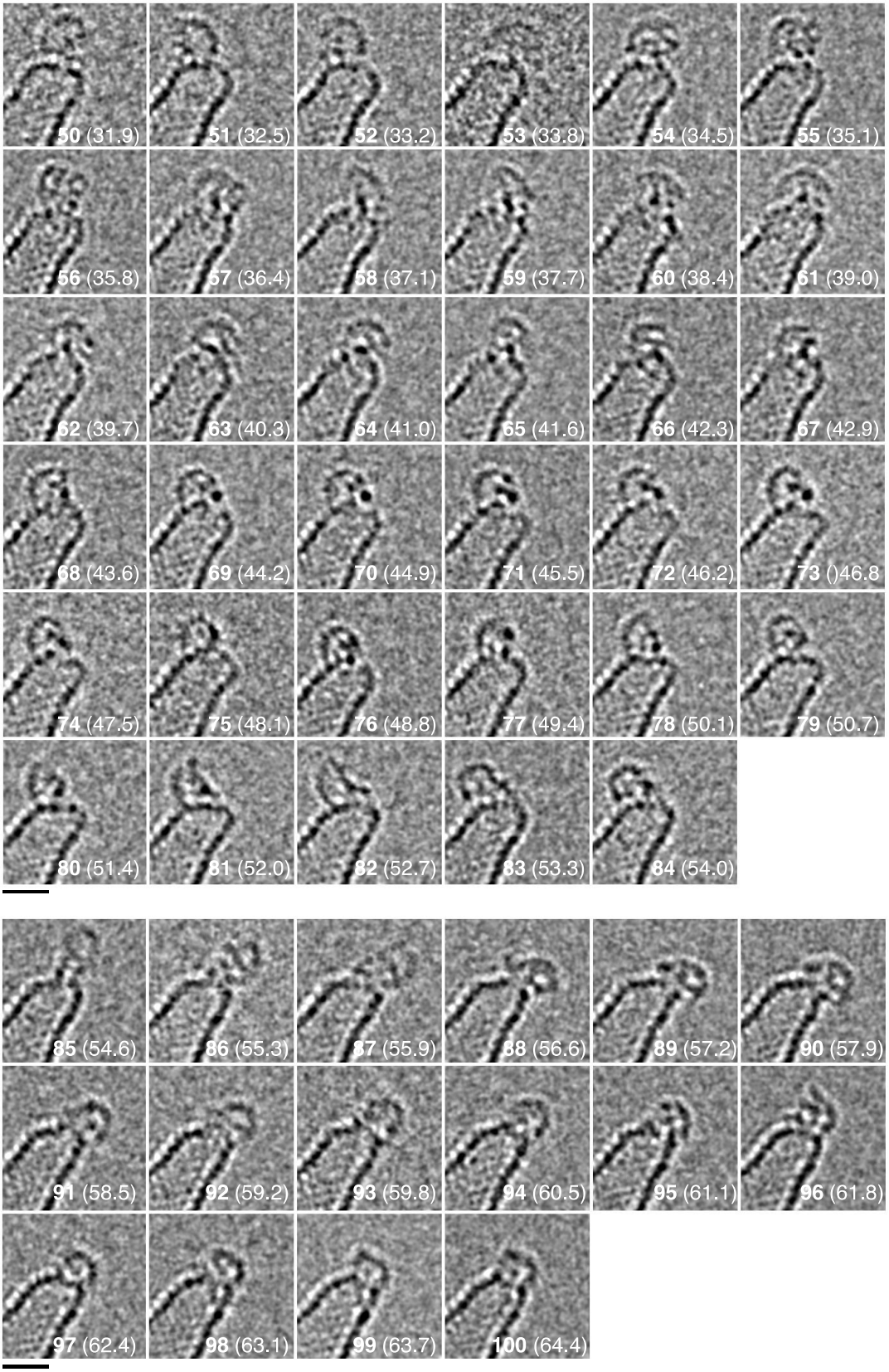

Figure 5-8. Conformational changes of biotinylated molecule **3** under an acceleration voltage of 80 kV (top: frames 50 to 84; bottom: 85 to 100). Scale bars are 1 nm. The numbers refer to the frame number in the movie. Time is shown inside the parenthesis in seconds.

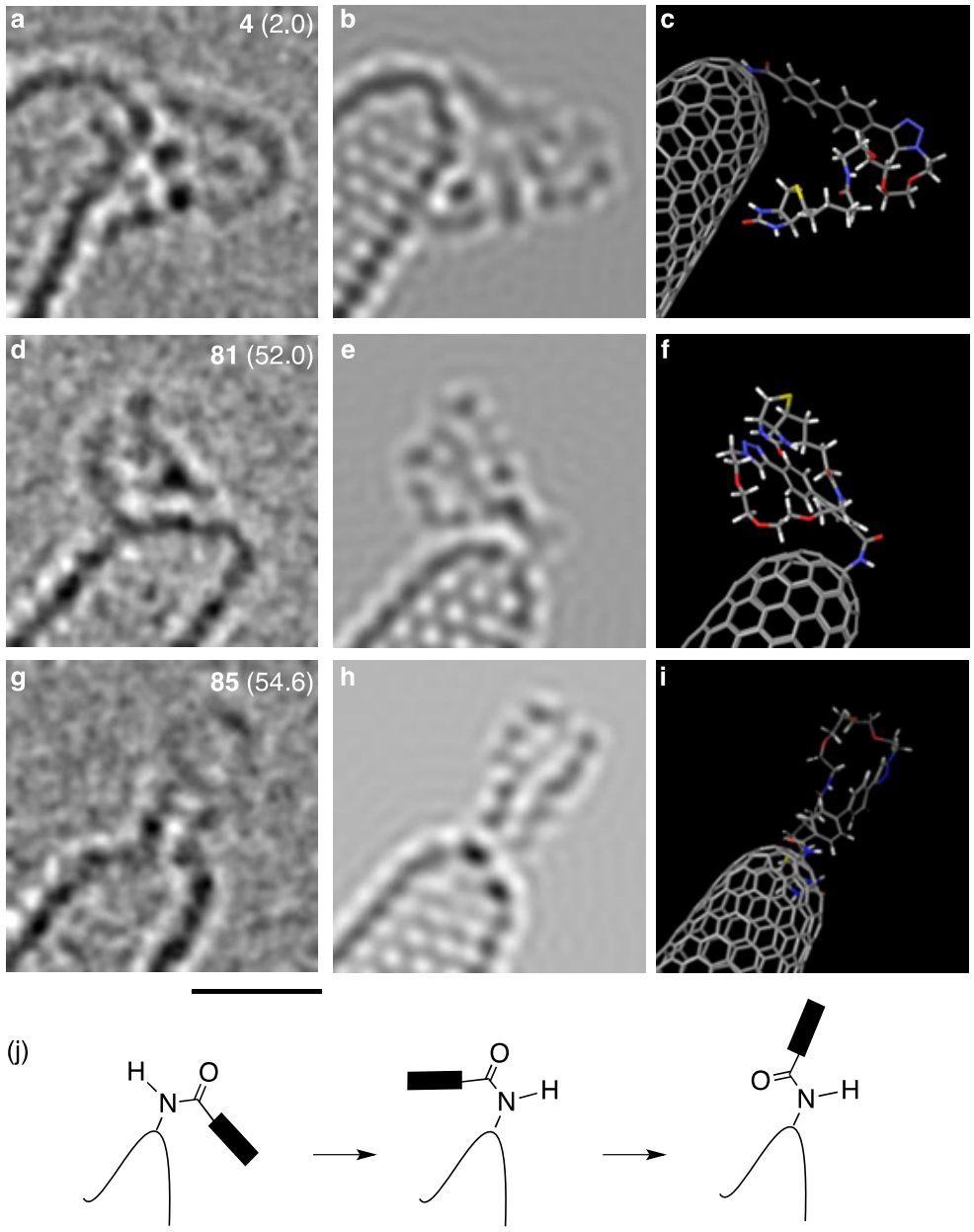

Figure 5-9. Plausible conformations of frames 4, 81 and 85 of a TEM movie of **3** under 80 kV. (a–i) The TEM image is shown in the left, a molecular model of a plausible conformation is shown in the right, and its TEM simulation is shown in the middle. Scale bar is 1 nm. (j) Schematic image of the conformational changes of **3**.

Plausible conformations of the biotinylated molecule for representative frames of the TEM movie (frames 4, 81, and 85) were determined by comparison to simulated TEM images from molecular models of **3** (Figure 5-9) and further supported the conclusions of the preliminary analysis. Molecular models of the biotinylated carbon nanohorns were constructed and minimized by molecular mechanics calculations[18] and the TEM simulation images were

generated by using a multi-slice procedure implemented in a standard simulation software[19]. The molecular models were optimized by rotation of the bonds and further minimization of the structure so that the simulated TEM image matched the experimental image.

The simulated images matched well enough for determination of the structural characteristics of **3** in each frame, such as the conformation of the amide bond or the position of the spacers and terminal biotin. In frame 4 (Figure 5-9a–c), the terminal biotin is close the nanohorn surface and appears in a v-shape. In frame 81 (Figure 5-9d–f), the amide bond rotates and the single molecule is seen on the opposite side of the nanohorn. By rotation of the single molecule, the terminal biotin is placed at the top of the image, appearing as a large and dark spot. The amide bound is in the *cis* conformation in these two frames. In frame 85 (Figure 5-9g–i), the molecule adopts a hairpin shape formed by the tetraethylene oxide chain and the biphenyl spacer. To achieve the conformation perpendicular to the horn edge, the amide isomerized to *trans* conformation (Figure 5-9j).

The results presented in this section suggests the observation of the different conformations of a single organic molecule in a TEM movie may become a useful tool for the observation of a same molecule under different angles, providing much more structural information than a single image would provide.

5.5 Analysis of the dynamic profile by molecular dynamics simulation

The conformational changes of **3** in the TEM movie were reproduced in molecular dynamics simulations and analysis of the simulation result suggested that they were originated from steric hindrance between nanohorn and biphenyl, which favored particular conformers. The simulation was performed in vacuum for 100 ns using the molecular model of frame 4 (Figure 5-9c) as initial state and OPLS-2005 as the force field. The temperature was set between 100 and 1000 K, and not 297 K as in the experiment, because there is no direct relationship between the experimental and simulation temperatures. The temperature of the TEM stage was reported to have no relationship to the temperature of the single molecules on carbon nanohorn, as the frequency in the conformational changes did not change by cooling or heating.[6]

The results were analyzed by the change in the dihedral angle θ of the C_{NH}-N bond between the nanohorn and the single molecule and in the potential energy of the conformers. Temperatures between 340 and 470 K were able to reproduce the dynamic profile of **3** observed in TEM in the time scale of the simulation (Figure 5-10a). After 28 ns, the dihedral angle θ changes irreversibly from a range of –20～–80° to a range of 150～180°, and the specimen molecule is transferred to the opposite side of the nanohorn (Figure 5-10b). This transformation is very similar to the transition observed between frames 49 and 50 in the TEM movie.

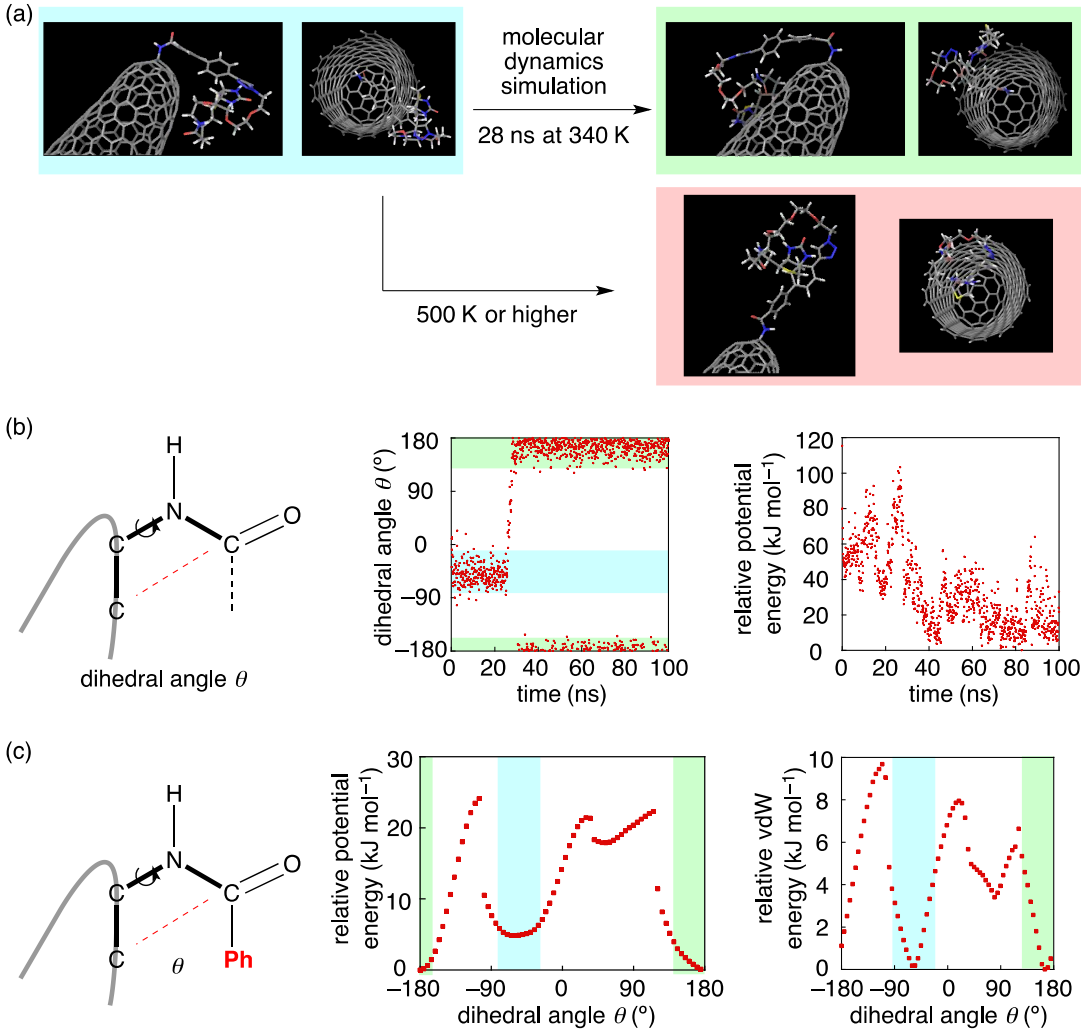

Figure 5-10. Molecular dynamics simulation of **3**. Molecular model in **Figure 5-9**f is used as initial state (force field is OPLS2005, no solvent, time step is 1.5 fs, equilibration time is 1.0 ps, simulation time is 100 ns, and sampling number is 1000). (a) Molecular model of **3** after simulation at 340 K and 500 K. (b) Time evolution of dihedral angle and relative potential energy at 340 K. (c) Dihedral angle dependence on the relative potential and vdW energies for a phenylbenzamide modified carbon nanohorn.

The average of the potential energy of the molecule after rotation of the bond is 36.0 kJ mol^{-1} lower than in the first region, suggesting that under these conditions the molecule converges to the conformer of lower energy. The existence of two preferable states is most likely originated from the chirality upon functionalization of the nanohorn, which affects the intensity of the van der Waals interaction between the nanohorn surface and the biphenyl spacer depending on the position of the C_{NH}-N bond. This conclusion was further supported by investigation of a benzamide modified carbon nanohorn (Figure 5-10c). The conformation minima (potential and vdW energies) coincided well with the dihedral angle θ of the conformers of **3**.

When the simulation was performed at temperatures above 500 K, the amide bond isomerizes as in frame 85 of the TEM movie (Figure 5-10a). This process accompanies an average energy decrease of 43.8 kJ mol^{-1}.

5.6 Analysis of conformational changes in TEM by automatic conformer determination using molecular dynamics simulation and calculation of cross correlation

The small conformational changes of molecule **3** were analyzed in more details and it was found that the small changes between consecutive frames were produced mainly by conformational changes of the flexible oligoethylene oxide spacer.

Possible conformers of **3** were generated by molecular dynamics simulation and the cross correlation was used to assign the most plausible molecular model to several TEM images (Figure 5-11). The molecular model of frame 83 (Figure 5-9d) was used as the initial state for the simulation. A simulation time as short as 1 ns at 300 K (sampling every 0.01 ns) was able to simulate representative frames of the TEM movie (Figure 5-11, e.g. frames 56, 71, 75, and 84). In these molecular models, the dihedral angle of the amide bond between the biphenyl spacer and carbon nanohorn changes only 17^{o} suggesting that the conformational changes observed for **3** in these TEM images were produced mainly by the changes in the flexible moiety of the molecule. The conformers differ from each other by approximately 30 kJ mol^{-1} in energy.

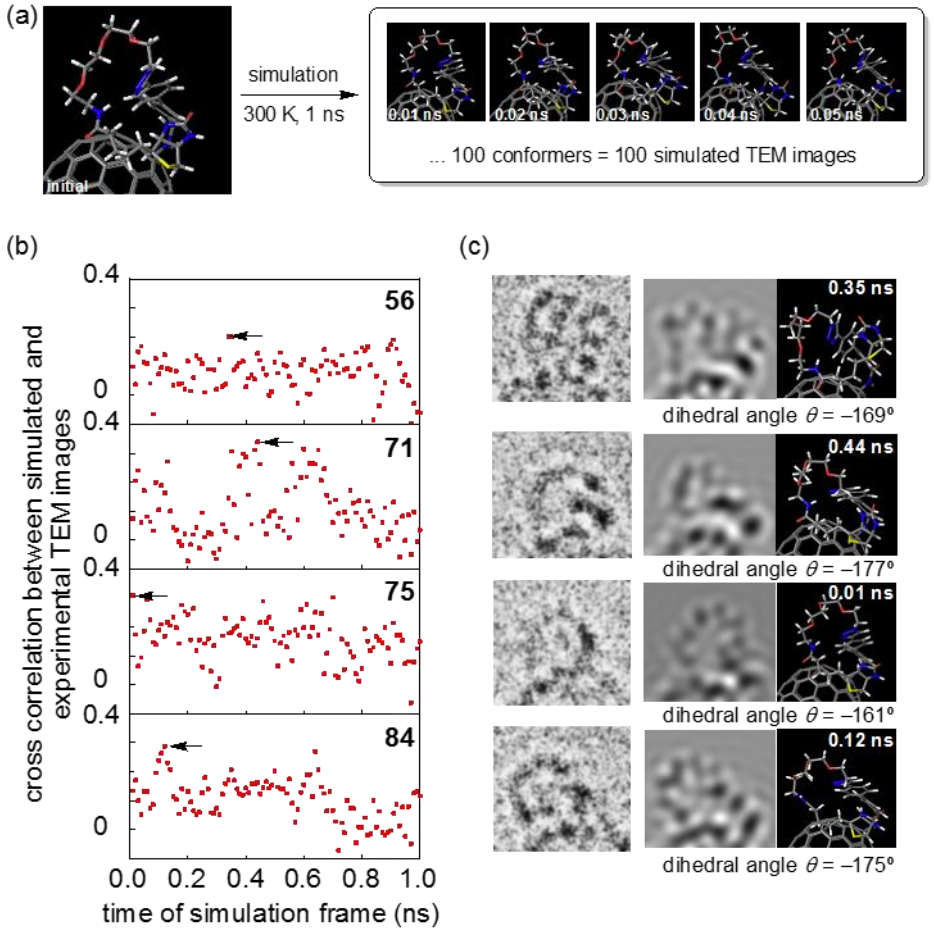

Figure 5-11. Investigation of the conformational changes of molecule **3** in frames 50 to 84 by comparison to simulated models using cross correlation. Results of representative frames 56, 71, 75, and 84 are shown. (a) Molecular dynamics simulation produced 100 conformers. (b) Cross correlation between experimental and simulated TEM images. (c) The images from left to right are the TEM data, the TEM simulated image and the molecular model determined by this method.

The approximate energetics obtained by the molecular dynamics calculations for the images shown in Figure 5-7 and Figure 5-8 of molecule **3** are summarized in Figure 5-12. The group of conformers seen in frames 1–49 is the least stable group, which involves a *cis*-amide, a small θ value and a variety of OEO conformations. The N–C_{CNH} bond rotation (θ) results in the more stable conformers seen in frames 50–84 and the *cis*-to-*trans* amide rotation results in the most stable conformers seen in frames 85–100.

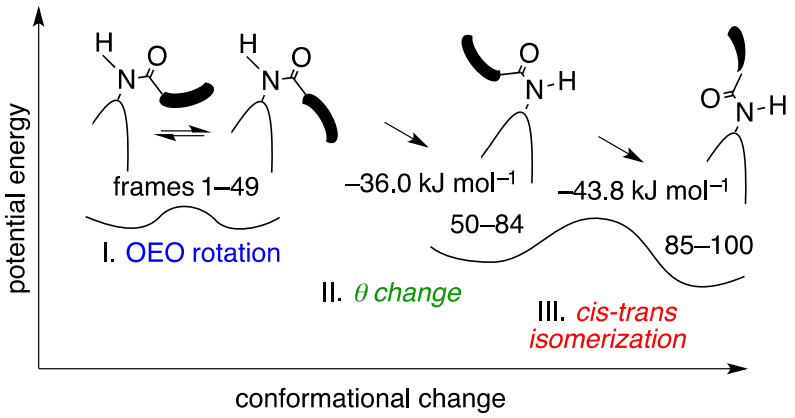

Figure 5-12. An approximate potential surface for the conformational change of **3** as deduced from the time evolution of the TEM images supported by the MD calculations.

Although molecule **2** also contains an oligo(ethylene oxide) moiety, its conformational changes were much simpler than the one observed for **3** (Figure 5-4e). The difference in the TEM movies of these two molecules can be explained by the completely different molecular design. The perpendicular attachment of the single molecule allows free rotation of the biphenyl moiety in **2**, which is not possible in **3**. However, the rotation of the biphenyl moiety in **2** produces less obvious conformational changes than the rotation of the amide bond in **3**, as a TEM movie.

5.7 Conclusion

In conclusion, control of the conformational changes of single organic molecules observed by SMART-TEM was achieved. A low acceleration voltage of 60 or 80 kV was necessary to accelerate the conformational changes of the molecules observed in TEM movies. The observed dynamics also depended on the design of the molecules. The more flexible molecule **3** is mobile enough at 80 kV to show us visually the process of stepwise energy relaxation by sequential rotations of σ-bonds in vacuum—a piece of information so far unobtainable by experimental methods but only by theoretical simulations.

In the near future, the combination of SMART-TEM technique with improvements in the imaging resolution of electron microscopy will allow the investigation of the dynamics of more complex organic molecules, such as small proteins and their self-assembled structures.

5.8 Experimental Section

5.8.1 General

All reactions dealing with air- or moisture-sensitive compounds were carried out in a dry reaction vessel under nitrogen or argon. The water content of the solvent was confirmed with a Karl-Fischer Moisture Titrator (MKC-210, Kyoto Electronic Company) to be less than 100 ppm. Analytical thin-layer chromatography was performed on glass plates coated with 0.25 mm 230-400 mesh silica gel containing a fluorescent indicator (Merck). Flash silica gel column chromatography was performed on silica gel 60N (Kanto, spherical and neutral, 140-325 mesh) as described by Still.[20] NMR spectra were measured on JEOL ECA-500 or on JEOL ECX-400 spectrometers and reported in parts per million from tetramethylsilane. ^{1}H NMR spectra in $CDCl_3$ were referenced internally to tetramethylsilane as a standard, and ^{13}C NMR spectra to the solvent resonance. Methyl, methylene, and methyne signals in ^{13}C NMR spectra were assigned by DEPT spectra. IR spectra were recorded on JASCO FT-IR-6100 equipped with attenuated total reflection (ATR) and are reported as wavenumber in cm^{-1}. High resolution mass spectra were acquired by APCI or electrospray ionization (ESI) using a time-of-flight mass analyzer on JEOL JMS-T100LC (AccuTOF) spectrometer with a calibration standard of reserpine. Distilled water was further deionized with Millipore Milli-Q. Scanning electron microscopy (SEM) was performed on FEI Magellan 400L. Single-molecule and real-time TEM (SMART-TEM) observations were carried out using JEOL ARM-200F or FEI Titan G2 at 293 K under reduced pressure of 1.0×10^{-5} Pa in the sample column. Detailed observation conditions and procedures are described below.

5.8.2 Materials

Unless otherwise noted, materials were purchased from Tokyo Kasei Co., Aldrich Inc., and other commercial suppliers and used after appropriate purification before use. Anhydrous ethereal solvents (stabilizer-free) were purchased from WAKO Pure Chemical and purified by a solvent purification system (GlassContour)[21] equipped with columns of activated alumina and supported copper catalyst (Q-5) prior to use. All other solvents were purified by distillation and stored over molecular sieves 4Å. Carbon grids for the TEM observation were purchased from Oken Shoji Co., Ltd. Azide-PEG3-biotin

conjugate **4** (*N*-[2-[2-[2-(2-Azidoethoxy)ethoxy]ethoxy]ethyl]biotinamide), 4'-ethynyl-[1,1'-biphenyl]-4-carboxylic acid **5** and 4'-trimethylsilyl-4-amino -biphenyl **10** were synthesized following the reported procedures.[22,23,24] Carbon nanohorn was purchased from NEC. Amino carbon nanohorn (amino–CNH) and biotinylated triamide carbon nanohorn **1** were prepared according to previous reports.[9,25]

5.8.3 Synthesis: Functionalization of carbon nanohorn aggregates

Scheme 5-1. Synthesis of biotinylated carbon nanohorn **3** from amino carbon nanohorn. (i) $CuSO_4 \cdot 5H_2O$ (0.10 eq), sodium L-ascorbate (1.0 eq), ^{t}BuOH/H_2O/THF (1:1:2), 15 h, 25 ºC. (ii) *N*,*N*-diisopropylethylamine (1.1 eq), TSU (2.0 eq), DMF, 5 h, 25 ºC. (iii) amino carbon nanohorn (0.11 eq of NH_2 per azide), DMF, 22 h, 25 ºC.

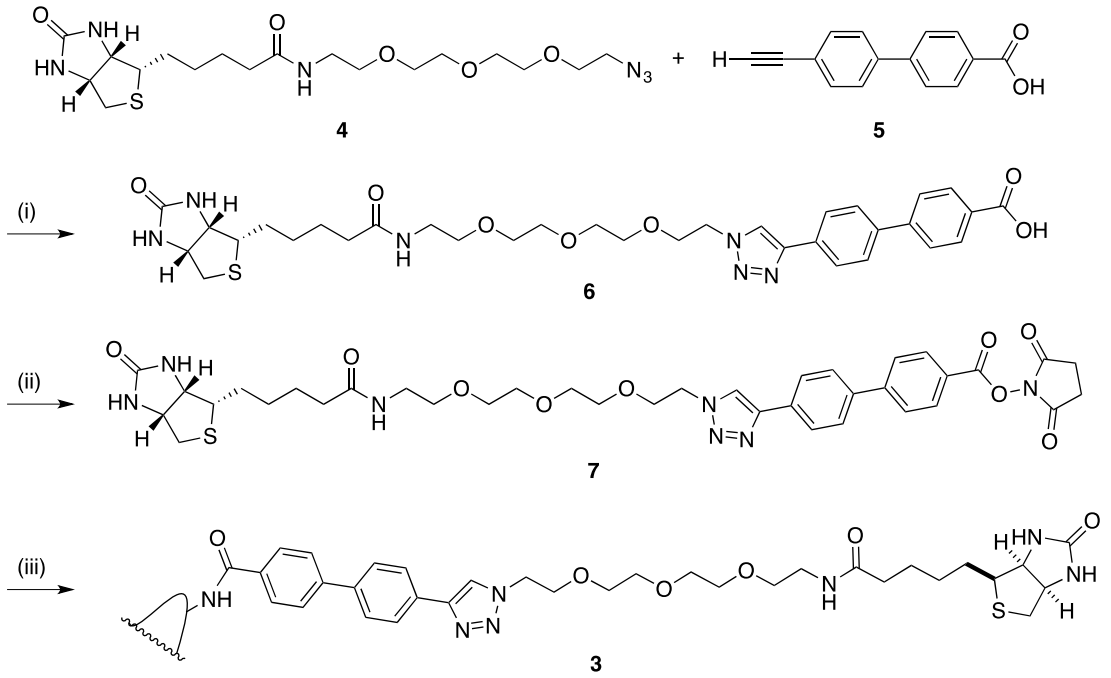

Synthesis of biotin-PEG3-biphenyl-COOH conjugate **6** (adapted procedure from ref. 26)

A solution of azide-PEG3-biotin conjugate **4** (45.0 mg, 102 μmol) and 4'-ethynyl-[1,1'-biphenyl]-4-carboxylic acid **5** (25.0 mg, 112 μmol) in *t*-butanol / water / THF (1:1:2, 2 mL) was prepared. Copper sulfate pentahydrate (2.61 mg, 10.5 μmol) and sodium L-ascorbate (102 μL, 1.0 M, 102 μmol, aqueous solution) were added to the solution of starting materials and the reaction mixture was stirred for 15 hours at 25 ºC. After dilution with dichloromethane (50 mL), hydrochloric acid (3 M, 0.5 mL) was added. The organic phase was washed

with water (25 mL), dried under magnesium sulfate, filtered and concentrated under reduced pressure. The crude was dissolved in methanol / chloroform (1:1, 6 mL) and the product was selectively precipitated by addition of an excessive amount of diethyl ether. Filtration though a membrane filter and drying under reduced pressured yielded compound **6** as a white solid (18.5 mg, 27%). Mp 165–167 °C; IR 2924, 2863, 1746, 1690, 1630, 1604, 1543, 1458, 1425, 1368, 1309, 1288, 1232, 1118, 1049, 1007, 921, 838, 805, 775, 684, 632, 602, 590, 576, 558 cm^{-1}. ^{1}H NMR ($CDCl_3$, 500 MHz) δ 1.16–1.67 (m, 6H), 2.14 (t, *J* = 7.5 Hz, 2H), 2.68 (d, *J* = 12.6 Hz, 1H), 2.85–2.89 (m, 2H), 3.12–3.16 (m, 1H), 3.43–3.66 (m, 12 H), 3.96 (t, *J* = 5.2 Hz, OH), 4.24 (dd, *J* = 4.6 Hz, *J* = 8.0 Hz, 1H), 4.45 (dd, *J* = 4.6 Hz, *J* = 8.0 Hz, 1H), 4.66 (t, *J* = 5.2 Hz, 2H), 7.76 (d, *J* = 8.6 Hz, 2H), 7.78 (d, *J* = 8.6 Hz, 2H), 7.94 (d, *J* = 8.6 Hz, 2H), 8.09 (d, *J* = 8.6 Hz, 2H), 8.44 (s, 1H). ^{13}C NMR (methanol-d4, 100 MHz) δ 26.94 (CH2), 29.60 (CH2), 29.89 (CH2), 36.84 (CH2), 40.41 (CH2), 41.18 (CH2), 51.73 (CH2), 57.12 (CH), 61.74 (CH), 63.48 (CH), 70.48 (CH2), 70.68 (CH2), 71.37 (CH2), 71.60 (CH2), 71.63 (CH2), 71.68 (CH2), 116.15, 123.57 (CH), 127.41 (CH), 128.01 (CH), 128.95 (CH), 131.59 (CH), 131.84, 141.13, 146.23, 148.27, 166.24, 169.65, 176.21. HRMS (APCI+) calcd for $C_{33}H_{42}N_6O_7S$ $[M+Na]^+$ m/z = 689.2733, found m/z = 689.2734.

*Synthesis of biotinylated carbon nanohorn **3***

TSU (3.80 mg, 12.6 μmol) and DIPEA (1.16 uL, 6.63 μmol) were added to a solution of **6** (4.09 mg, 6.13 μmol) in DMF (2.8 mL) and stirred at 25 °C for 2 hours. Consumption of **6** was confirmed by disappearance of the peak from **6** in the mass spectrum. DMF was removed under reduced pressure and the crude product was used in the next step without further purification.

Amino carbon nanohorn (4.83 mg, 0.672 μmol) was dispersed in DMF (5 mL) and added to the crude product (6.13 μmol, 9 eq) of the previous reaction. The reaction mixture was stirred at 25 °C for 22 hours. The product was collected by filtration through a membrane filter (pore size of 200 nm) and washed with DMF (1 mL × 5) and ethanol (1 mL × 5). The filtrate was dried under reduced pressure to give a black powder (5.15 mg) of particles of **3**.

Scheme 5-2. Synthesis of biotinylated carbon nanohorn **2** from pristine carbon nanohorns (adapted procedure from ref. 14). (i) 4'-trimethylsilyl-4-amino-biphenyl **10** (4 eq. per carbon in carbon nanohorn), isoamyl nitrite (4 eq. per carbon), NMP, 70 ºC, 26 h. (ii) TBAF (excess), THF/NMP (1:6), 25 ºC, 2 h. (iii) 4 (1.0 eq), $CuSO_4 \cdot 5H_2O$ (1.0

eq), sodium ascorbate (10 eq), NMP, 70 ºC, 48 h.

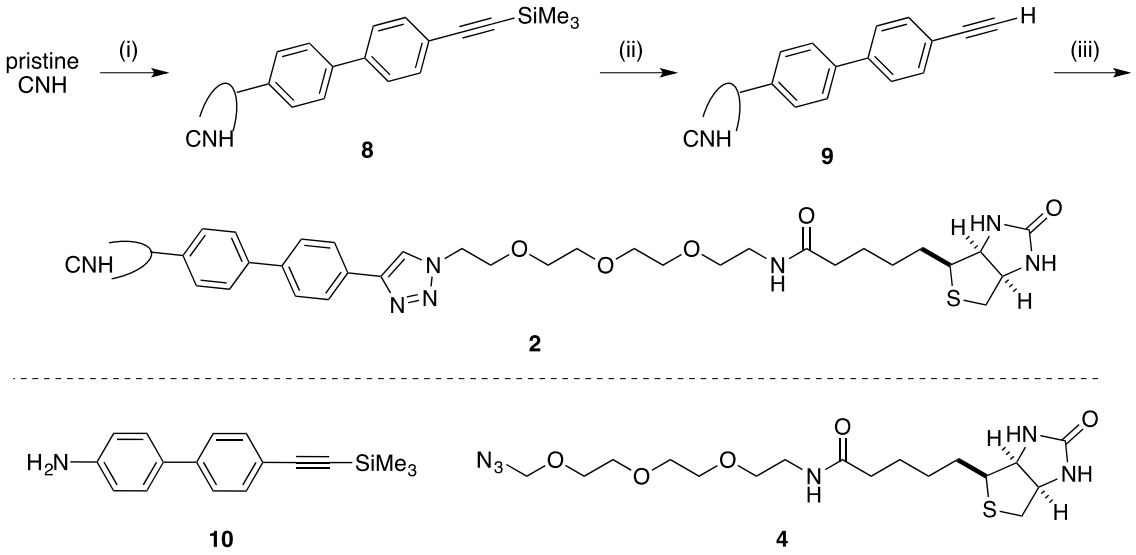

*Synthesis of functionalized carbon nanohorn **8***

Pristine carbon nanohorn (14.9 mg) was suspended in NMP (50 mL) and dispersed by bath sonication under argon for 10 minutes. 4'-trimethylsilyl-4-amino-biphenyl (1.34 g, 5.05 mmol, 4 equivalents per carbon) was added and the mixture was bubbled with argon for 10 minutes before addition of isoamyl nitrile (551 mg, 4.70 mmol). The reaction mixture was stirred at 70 °C for 24 hours. After cooling to room temperature, the modified carbon nanohorn was collected by filtration through a membrane filter and washed with DMF (5 mL × 3) and DCM (1 mL). The product was obtained as a black powder (18.8 mg) and used in the next step without further purification.

*Synthesis of biotinylated carbon nanohorn **2***

Functionalized carbon nanohorn **8** (10.0 mg) was suspended in NMP (37 mL) and dispersed by bath sonication for 10 min under argon. After bubbling with argon at 0 °C for 10 minutes, a 1.0 M solution of TBAF in THF (4.0 mL, 4 mM) was added dropwise. The reaction mixture was warmed to room temperature and stirred for 2 hours. The unprotected carbon nanohorn **9** was collected by filtration through a membrane filter and washed with DMF (3 mL, then 1 mL x 2) and DCM (1 mL × 3). The product was obtained as a black solid (9.99 mg).

The alkyne modified carbon nanohorn **9** (5.26 mg) was suspended in NMP (17 mL) and dispersed by bath sonication for 10 minutes under argon.

After bubbling with argon for 10 minutes, azide-PEG3-biotin conjugate **4** (5.13 mg, 11.5 μmol), copper (II) sulfate pentahydrate (2.75 mg, 11.0 μmol), and (+)-sodium L-ascorbate (23.6 mg, 119 μmol) were added. The reaction mixture was warmed to 70 ^{o}C and stirred for 48 hours. The product was collect by filtration through a membrane filter and washed under sonication with water:DMF (4:1, 5 mL) and THF:DMF (4:1) for three times. The product was washed with THF and dried under vacuum to yield biotinylated carbon nahorn **2** as a black solid (4.79 mg).

5.8.4 Methods

Procedure for dynamic light scattering analysis

Dynamic light scattering (DLS) measurement was performed on a Malvern Zetasizer Nano ZS equipped with an He-Ne laser operating at 4 mW power and 633 nm wavelength, and a computer-controlled correlator, at a 173 ^{o} accumulation angle. Measurement was carried out at 25 ^{o}C in a polystyrene or glass cuvette. The data were processed using dispersion technology software version 5.10 to give Z-average particle size and polydispersity index (PdI) value by cumulant analysis, and particle size distribution by CONTIN analysis.

The drastic changes in the dispersibility of carbon nanohorn **2** from its precursor **9** observed in water and dichloromethane supports the successful functionalization of the nanohorns with the water-soluble biotinylated molecules.

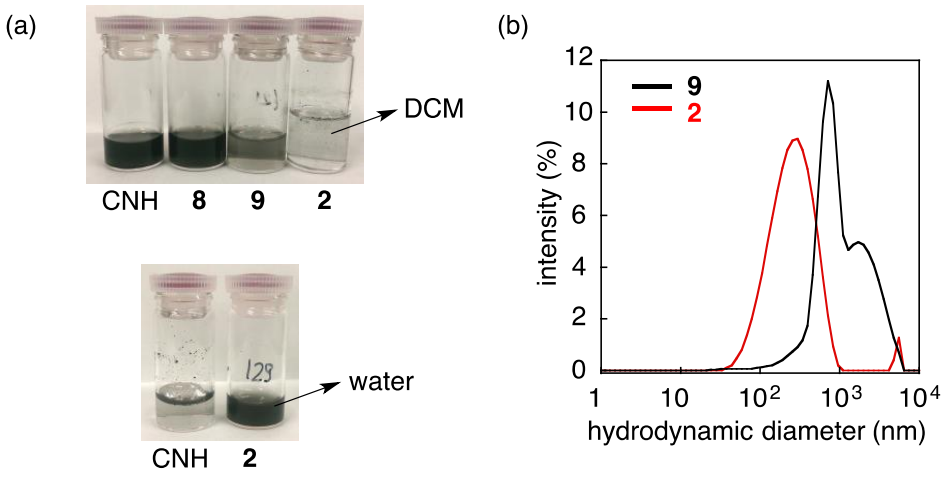

Figure 5-13. (a) Dispersion of pristine and functionalized carbon nanohorns in (top) dichloromethane and (bottom) water after bath sonication of 0.1 mg of sample in 1 mL of solvent for 30 minutes. After introduction of PEG3-biotin moiety, the dispersibility of carbon nanohorn **2** in dichloromethane decreased, and in water increased. (b) Size distribution of dispersed carbon nanohorn before and after functionalization with the hydrophilic PEG3-biotin moiety in water determined at 25 ºC by DLS.

Preparation of sample for electron microscope investigation

The black powder of modified carbon nanohorns (ca. 0.1 mg) was dispersed in water (1 mL) by bath sonication (2 seconds × 5). 10 μL of the suspension was placed onto a TEM mesh pre-coated by microgrids and the excessive amount of solvent was blotted by a filter paper. The TEM mesh was dried under reduced pressure (6×10^{-2} Pa) for 1 hour before observation by electron microscope.

Procedure for high-resolution SEM observation

SEM observation was performed on a FEI Magellan 400L instrument at 5×10^{-5} Pa. The working distance was set to 4 mm. Secondary electrons were collected with a through-lens detector. Observation at a beam landing voltage of 25 kV under a current of 3.1–25 pA was performed.

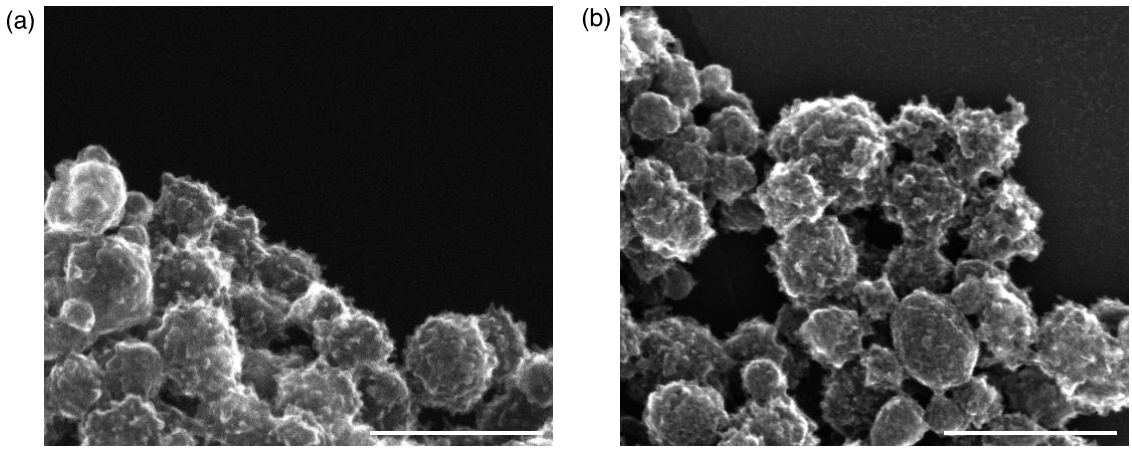

Figure 5-14. SEM images of biotinylated carbon nanohorn (a) **2** and (b) **3** under 10^{-5} Pa on a TEM copper grid. Individual horns can be clearly seen on the aggregate surface. Scale bars are 200 nm.

Procedure for SMART-TEM observation

Single-molecule and real-time TEM (SMART–TEM) measurements were carried on a C_s-corrected JEOL ARM-200F (acceleration voltage of E = 80 kV or 60 kV, 1.3×10^6 e$^-$ nm^{-2} s^{-1} or 1.5×10^4 e$^-$ nm^{-2} s^{-1} of dose rate, T = 293 K, 4×10^{-6} Pa) for **1** or in a FEI Titan G2 (acceleration voltage of E = 80 kV, 2.5×10^6 e$^-$ nm^{-2} s^{-1} of dose rate, T = 293 K, 1.0×10^{-5} Pa) in a sample column equipped with a monochromator and aberration corrector for **2**. The imaging instrument was a multiscan camera (1,024 × 1,024 pixels). A series of TEM images was obtained at intervals of 0.65 s with an exposure time of 0.4 s followed by a readout time of 0.25 s (non-irradiated).

SMART–TEM image simulation: Determination of the molecular structure of biotinylated molecules on carbon nanohorns.

Computational molecular models of the biotinylated carbon nanohorns were constructed with a variety of conformations of the biotin moiety, and viewed from a variety of directions. TEM simulation images were generated for each structure by using a multi-slice procedure implemented in a standard simulation software,[19] where a defocus value of –47.5 nm and a spherical aberration coefficient (Cs) of 0 mm were used. Each of the simulated TEM images was carefully compared with each image in the movie of biotinylated carbon nanohorns to conclude that the specimen molecule that we examined is indeed the biotinylated molecule that we attached by the amide bond

formation.

TEM analysis of carbon nanohorn 2

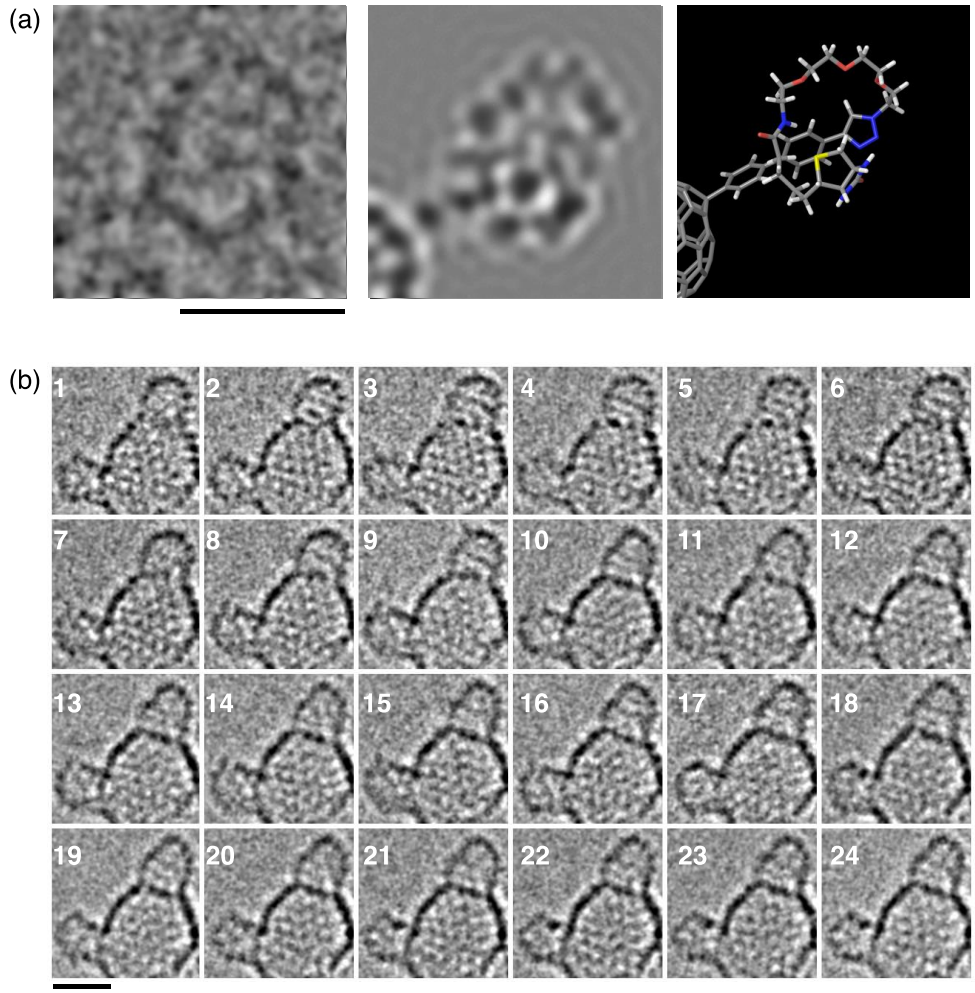

Figure 5-15. (a) TEM image of **2** under an acceleration voltage of 120 kV in the left, a plausible molecular model in the right and the TEM image in the middle simulated from the molecular model. Scale bar is 1 nm. (b) Small conformational changes of biotinylated molecule **2** under an acceleration voltage of 80 kV. Scale bar are 1 nm. The numbers refer to the frame number in the movie.

Analysis of overall motion of single organic molecules in TEM movies by calculation of cross correlation between TEM images

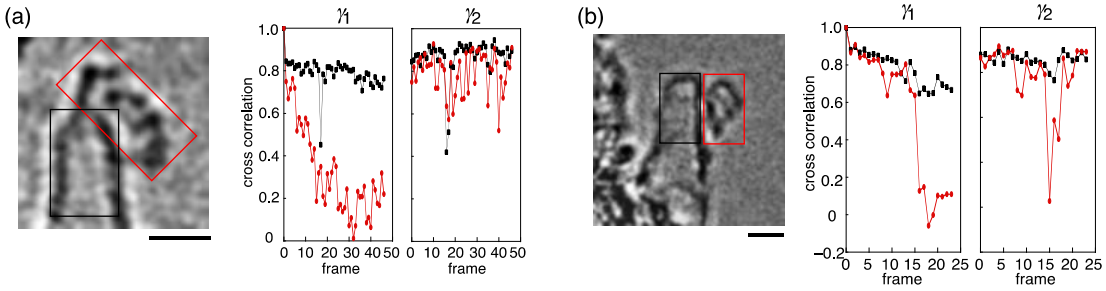

Figure 5-16. Cross correlation analysis of two different movies of **1** at 120 kV. Scale bars are 1 nm.

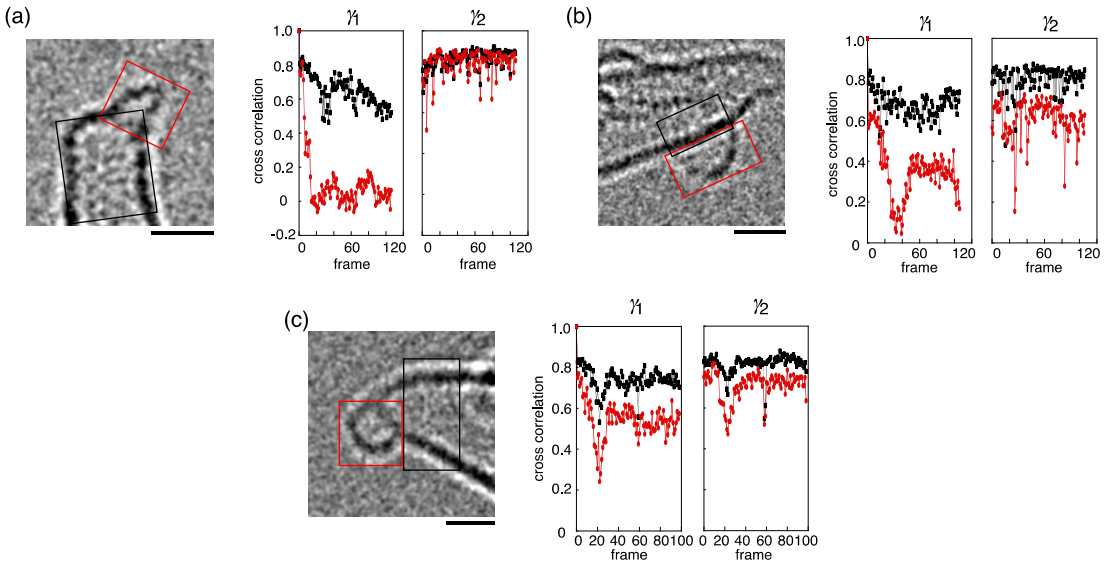

Figure 5-17. Cross correlation analysis of three different movies of **1** at 80 kV. Scale bars are 1 nm.

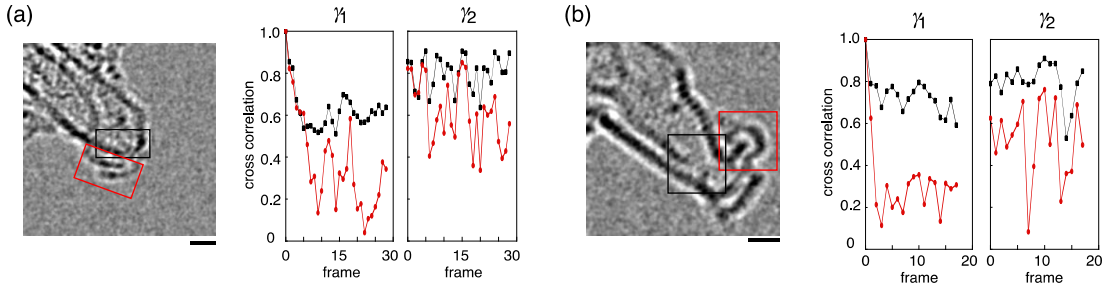

Figure 5-18. Cross correlation analysis of two different movies of **1** at 60 kV. Scale bars are 1 nm.

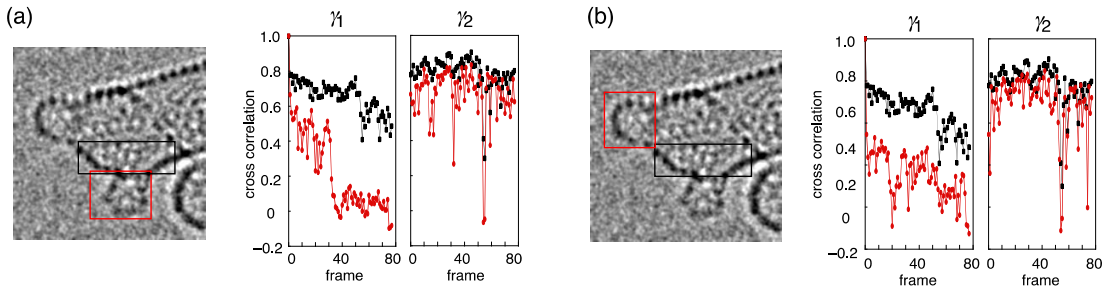

Figure 5-19. Cross correlation analysis of two different movies of **2** at 80 kV. Scale bars are 1 nm.

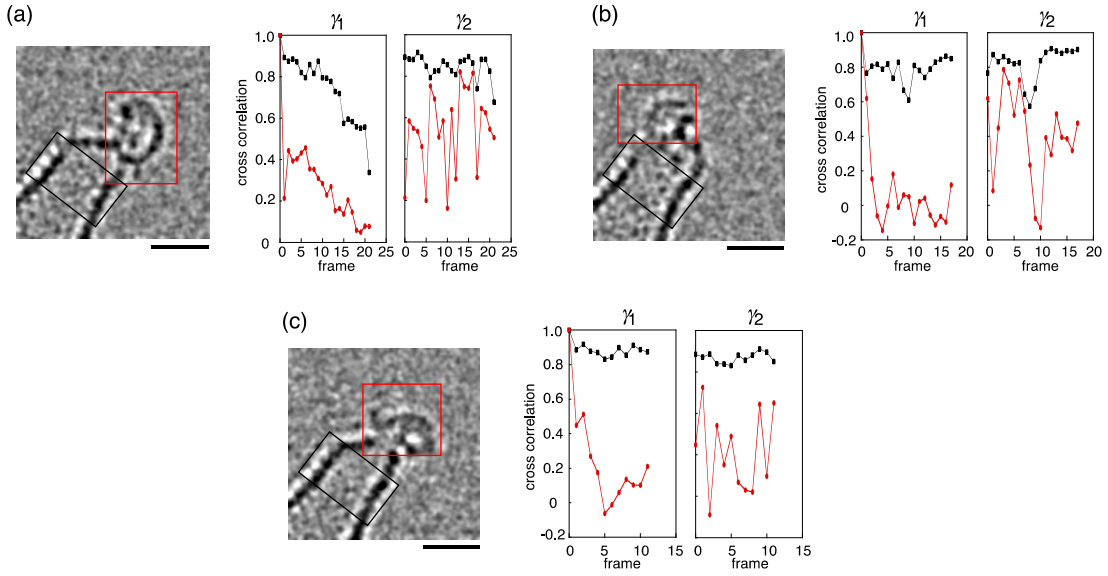

Figure 5-20. Cross correlation analysis of **3** at 80 kV. Scale bars are 1 nm.

Molecular dynamics simulation

Molecular mechanics calculation was conducted on Maestro, version 9.3, Schrödinger, LLC, New York, NY, 2012. and MacroModel, version 9.9, Schrödinger, LLC, New York, NY, 2012. with OPLS-2005 force field. Molecular dynamics simulation was conducted on a stochastic dynamics mode with 1.5 fs time step and 1.0 ps equilibration time.

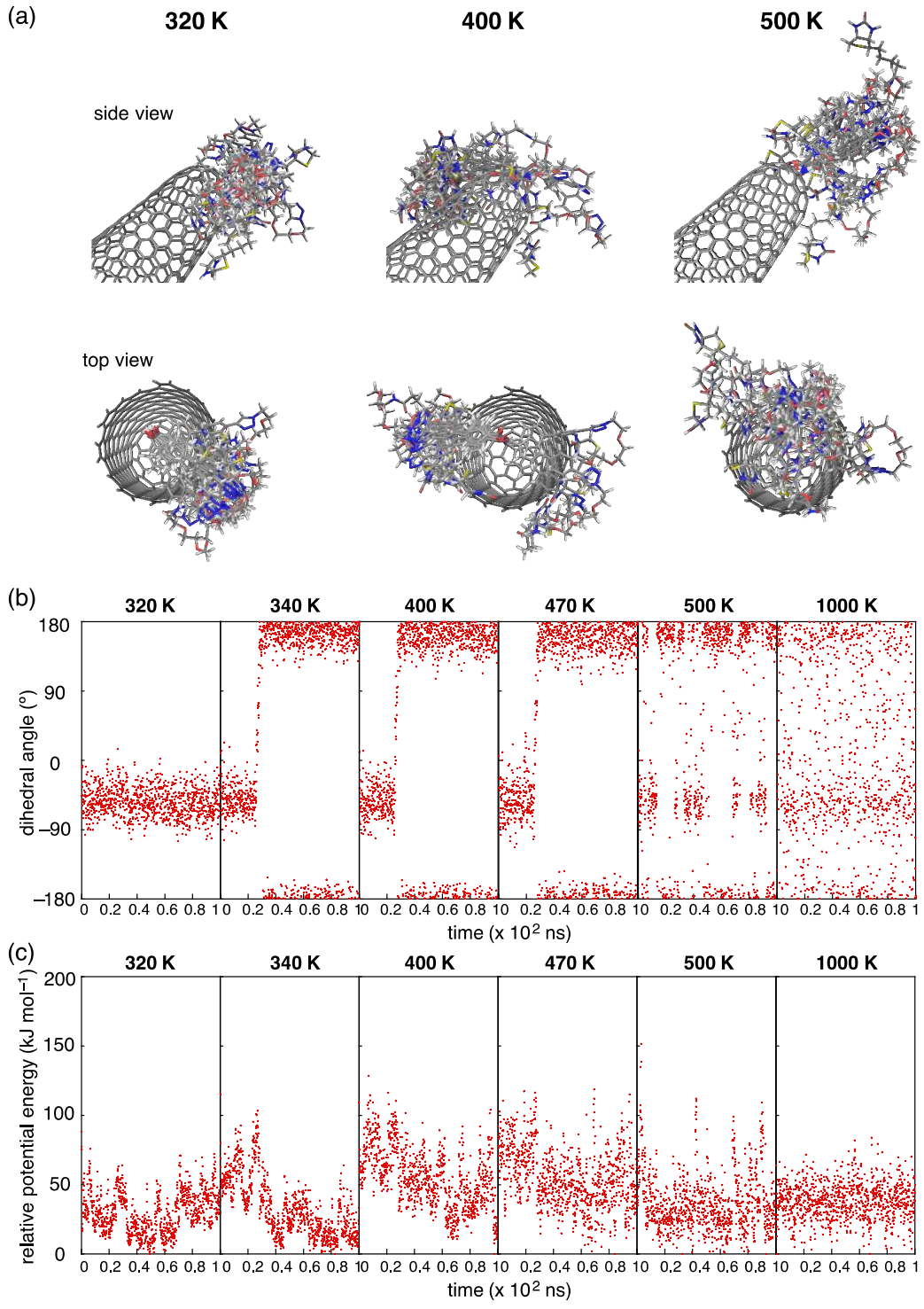

Figure 5-21. Molecular dynamics simulation of compound **3** at different temperatures (320 K to 1000 K). Molecular model in **Figure 5-9**f is used as initial state. (Force field is OPLS2005, no solvent, time step is 1.5 fs, equilibration time is 1.0 ps, simulation time is 100 ns, sampling number is 1000). (a) Overlay image of molecular conformers sampled every 10 ns. (b) Schematic image of the dihedral angle θ analyzed in this simulation. (c) Change of the dihedral angle θ during the simulation. (d) Change of potential energy during the simulation.

Calculation of cross correlation between experimental and simulated TEM images

The cross correlation γ (Equation 5-1) between experimental and simulated TEM images was found to be a good parameter to determine the accuracy of the molecular model.

The matching of a TEM image of a 1.3 nm carbon nanotube fragment and its simulated image is shown as an example. The cross correlation was calculated by using different parts of the TEM image, as shown in Figure 5-22, and the maximum value was obtained only when the position of the nanotube walls coincided in the two images.

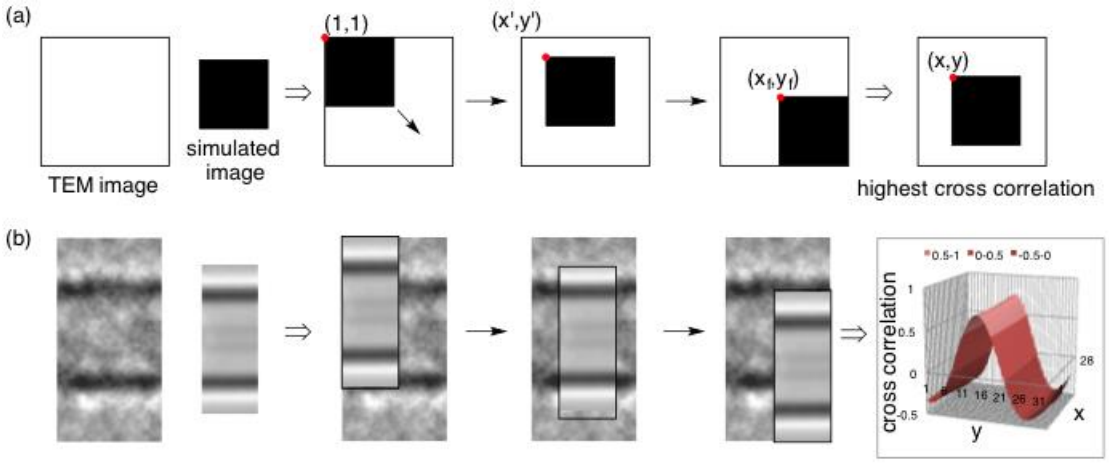

Figure 5-22. Cross correlation between experimental and simulated TEM images. (a) Schematic image showing the method for calculation of the cross correlation. A simulated image is compared with all possible selections of a TEM image. The combination that gives the highest cross correlation value is selected. (b) Experimental and simulated TEM images of a carbon nanotube. The nanotube has a diameter of 1.2 nm. Cross correlation value was plotted against the coordinates of the upper-left pixel of the simulated image relative to the TEM image.

The value of cross correlation could also be used to determine the position of the gauche conformation in a perfluoroalkyl chain of a fullerene derivative (Figure 5-23a), which Nakamura *et al.* investigated previously in a qualitative manner (Figure 5-23b).[7] The highest value for cross correlation was obtained for the simulation with a gauche conformation at position 8-9 (Figure 5-23c), confirming the conclusion obtained in that work.

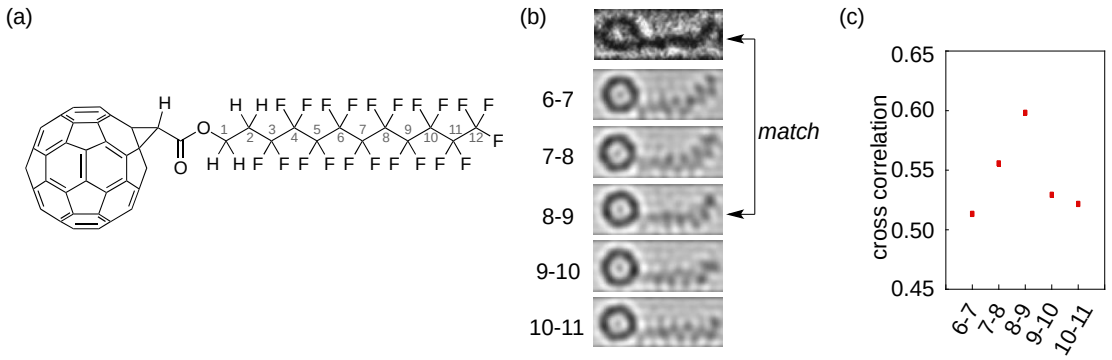

Figure 5-23. Example of the application of cross correlation value for determination of the molecular conformation of a fullerene derivative. (a) Structure of perfluoroalkyl modified fullerene. (b) A TEM image and a series of simulated images with one gauche conformation in different positions of the perfluoroalkyl chain. (c) Cross correlation calculated between experimental and simulated images. As previously reported, C8-C9 gauche conformer is the best match. Images are cited from ref. 7. Copyright 2014 American Chemical Society.

5.9 References

[1] Karplus, M. & McCammon, A. Molecular dynamics simulation of biomolecules. *Nat. Struct. Biol.* **9**, 646–652 (2002)

[2] Lensen, D. & Elemans, J. A. A. W. Artificial molecular rotors and motors on surfaces: STM reveals and triggers. *Soft Matter* **8**, 9053–9063 (2012).

[3] Tierney, H. L., Murphy, C. J., Jewell, A. D., Baber, A. E., Iski, E. V., Khodaverdian, H. Y., McGuire, A. F., Klebanov, N. & Sykes, C. H. Experimental demonstration of a single-molecule electric motor. *Nat. Nanotechnol.* **6**, 625–629 (2011).

[4] Schaffert, J., Cottin, M. C., Sonntag, A., Karacuban, H., Bobisch, C. A., Lorente, N., Gauyacq, J.–P. & Möller, R. Imaging the dynamics of individually adsorbed molecules. *Nat. Mater.* **12**, 223–227 (2013).

[5] Kobayashi, T. & Isoda, S. Lattice images and molecular images of organic materials. *J. Mater. Chem.* **3**, 1–14 (1993).

[6] Nakamura, E. Movies of molecular motions and reactions: The single-molecule, real-time transmission electron microscope imaging technique. *Angew. Chem. Int. Ed.* **52**, 236–252 (2013).

[7] Harano, K., Takenaga, S., Okada, S., Niimi, Y., Yoshikai, N., Isobe, H., Suenaga, K., Kataura, H., Koshino, M. & Nakamura, E. Conformational analysis of single perfluoroalkyl chains by single-molecule real-time transmission electron microscopic imaging. *J. Am. Chem. Soc.* **136**, 466–473 (2014).

[8] Harano, K., Homma, T., Niimi, Y., Koshino, M., Suenaga, K., Leibler, L. & Nakamura, E. Heterogeneous nucleation of organic crystals mediated by single-molecule templates. *Nat. Mater.* **11**, 877–881 (2012).

[9] Nakamura, E., Koshino, M., Tanaka, T., Niimi,Y., Harano, K., Nakamura, Y. & Isobe, H. Imaging of conformational changes of biotinylated triamide molecules covalently bonded to a carbon nanotube surface. *J. Am. Chem. Soc.* **130**, 7808–7809 (2008).

[10] Nakamura, E., Koshino, M., Saito, T., Niimi, Y., Suenaga, K. & Matsuo, Y. Electron microscopic imaging of single group 8 metal atom catalyzing C-C bond reorganization of fullerenes. *J. Am. Chem. Soc.* **133**, 14151–14153 (2011).

[11] Koshino, M., Niimi, Y., Nakamura, E., Kataura, H., Okazaki, T., Suenaga, K. & Iijima, S. Analysis of the reactivity and selectivity of fullerene dimerization reactions at the atomic level. *Nat. Chem.* **2**, 117–124 (2010).

[12] Koshino, M., Solin, N., Tanaka, T., Isobe, H. & Nakamura, E. Imaging of the Passage of a Single Hydrocarbon Chain through a Nanopore. *Nat. Nanotechnol.* **3**, 595–597 (2008).

[13] Williams, D. B. & Carter, C. B. *Transmission eelctron microscopy: A textbook for materials science*, 2nd Edition, Springer Science+Business Media LLC, USA, 2009.

[14] Vizuete, M., Gómez-Escalonilla, M. J., Fierro, J. L. G., Yudasaka, M., Iijima, S., Vartanian, M., Iehl, J., Nierengarten, J.-F. & Langa, F. A soluble hybrid material combining carbon nanohorns and C_{60}. *Chem. Commun.* **47**, 12771–12773 (2011).

[15] Kwon, O.-H., Barwick, B., Park, H. S., Baskin, J. S. & Zewail, A. H. Nanoscale Mechanical Drumming Visualized by 4D Electron Microscopy. *Nano Lett.* **8**, 3557–3562 (2008).

[16] Barwick, B., Park, H. S., Kwon, O.-H., Baskin, J. S. & Zewail, A. H. 4D Imaging of transient structures and morphologies in ultrafast electron microscopy. *Science* **322**, 1227–1231 (2008).

[17] Meyer, J. C., Eder, F., Kurasch, S., Viera, S., Kotakoshi, J., Park, H. J., Roth, S., Chuvilin, A., Eyhusen, S., Benner, G., Krasheninnikov, A. V. & Kaiser, U. Accurate measurement of electron beam induced displacement cross sections for single-layer graphene. *Phys. Rev. Let.* **1808**, 196102 (2012).

[18] Maestro, version 10.0, Schrödinger, LLC, New York, NY, 2014.

[19] Kirkland, E. J.; in Advanced Computing in Electron Microscopy, Plenum, London, **1998**.

[20] Still, W. C., Kahn, M. & Mitra, A. Rapid chromatographic technique for preparative separations with moderate resolution. *J. Org. Chem.* **43**, 2923–2925 (1978).

[21] Pangborn, A. B., Giardello, M. A., Grubbs, R. H., Rosen, R. K. & Timmers, F. J. Safe and convenient procedure for solvent purification. *Organometallics* **15**, 1518–1520 (1996).

[22] Fusz, S., Srivatsan, S. G., Ackermann, D. & Famulok. M. Photocleavable initiator nucleotide substrates for an aldolase ribozyme. *J. Org. Chem.* **73**, 5069–5077 (2008).
[23] Wright, A. T., Song, D. J. & Cravatt, B. F. A suite of activity-based probes for human cytochrome P450 enzymes. *J. Am. Chem. Soc.* **131**, 10692–10700 (2009).
[24] Bellamy, F. D. & Ou, K. Selective reduction of aromatic nitro compounds with stannous chloride in non acidic and non aqueous medium. *Tetrahedron Lett.* **25**, 839–842 (1984).
[25] Isobe, H., Tanaka, T., Maeda, R., Noiri, E., Solin, N., Yudasaka, M., Iijima, S. & Nakamura, E. Preparation, purification, characterization, and cytotoxicity assessment of water-soluble, transition-metal-free carbon nanotube aggregates. *Angew. Chem. Int. Ed.* **45**, 6676–6680 (2006).
[26] Tae, H. S., Hines, J., Schnnekloth, A. R. & Crews, C. M. Total Synthesis and Biological Evaluation of Tyroscherin. *Org. Lett.* **12**, 4308–4311 (2010).

— Chapter 6 —
Summary and outlook

In the present thesis, I developed the chemistry at the interfaces on carbons clusters based on precise molecular design and synthesis. Fullerene vesicles and carbon nanohorn aggregates were applied as scaffolds for selective binding of small molecules, tunable nanoreactors, plasmonic vesicles, and observation of single organic molecule dynamics.

In chapter 2, the binding of small aromatic molecules in the fullerene-rich interior of fullerene bilayer membranes was realized. Vesicles made of a nonpolar/polar/nonpolar amphiphilic fullerene, $R_5C_{60}^-K^+$, are composed of a bilayer of amphiphilic fullerenes where the fullerene core is located in the interior, the R groups are exposed to an aqueous environment, and the anionic part is located in the middle. Because of the unique architecture, the fullerene bilayers bind small hydrophobic molecules in a different way from lipid bilayers, which are made of nonpolar/polar lipid molecules. The part of the membrane that traps organic molecules was determined by using an aromatic fluorescent dye, prodan. The strong quenching of the fluorescence indicates that the vesicle binds aromatic molecules primary in the interior of the fullerene bilayer. The binding profile of the fullerene membrane for hydrocarbons largely depends on the structure of the R group. The fullerene-rich interior of the fullerene bilayer is the primary binding site of a small aromatic molecule, while the outer layer may host an aliphatic molecule when the R group bears aliphatic side chains. This preference does not reflect the logP_{ow} values and suggests that the binding occurs because of an aromatic–fullerene interaction. In addition, the vesicles take up a planar molecule very well but not bulky aromatic molecules. These results demonstrate the design of the hydrophobic environment of fullerene membranes in water by the R group on the fullerene amphiphile.

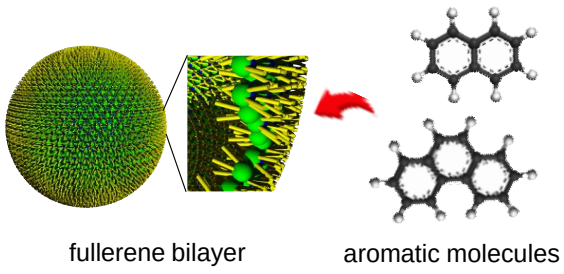

Figure 6-1. Binding of aromatic molecules to the fullerene-rich interior of fullerene

bilayer vesicles in water.

Attempts to utilize membranes for the control of polymerization were only partially successful because of the structural instability of the lipid bilayer. In chapter 3, I considered the fullerene bilayer membrane as a nanoreactor for controlled polymerization in water because it is a structurally robust liquid crystal. The fullerene bilayer gains its stability from mutually orthogonal forces, π–π, hydrophobic and fluorous interactions, and creates three regions: fullerene-rich core, interior and exterior. Ring-opening metathesis polymerization (ROMP) of a norbornene dicarboxylate ester catalyzed by a fluorous-tagged Hoveyda-Grubbs' catalyst on fullerene vesicles produced polyester of same molecular weight but in two different nm-scale morphologies, a capsule and a particle, isolable after removal of the vesicle by extraction. The ROMP conditions allowed the polymerization of a halide-containing monomer and a copolymer bearing a dansyl dye. The location of the polymers in the bilayer, determined by fluorescence quenching and shift measurements of the dansyl-functionalized copolymer formed in the vesicles as well as the water permeation profile and electron microscopic analysis, affected its morphology.

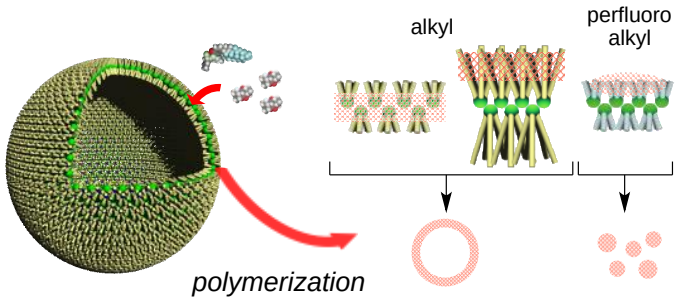

Figure 6-2. Control of polymer growth in nm-thick fullerene bilayer membranes.

In chapter 4, I achieved the construction of hybrids of fullerene vesicles and gold nanoparticles by interfacial adsorption. Functionalization of vesicles with inorganic particles is usually achieved by electrostatic interaction between vesicle surface and particles. However, strong repulsion between neighboring particles results in low surface coverage, limiting the applications of such structures. The hydrophobic surface of fullerene vesicles, created by the display of (perfluoro)alkyl chains on the surface, allowed the construction of sub-100

nm plasmonic vesicles densely covered with neutral gold nanoparticles by adsorption on the vesicle/water interface. The supramolecular assembly withstands purification by size exclusion chromatography and enhances the vesicle stability in biological conditions. The hierarchical structure is also maintained in the solid state after removal of water. The high stability was attributed to interparticle interaction mediated by the OEO chains on the nanoparticles, as suggested by NMR experiments. The nanoparticle size could be controlled by in situ growth on the vesicle surface. Coupling of the surface plasmon resonance of the larger nanoparticles was detected, suggesting the potential of these hybrids in imaging applications.

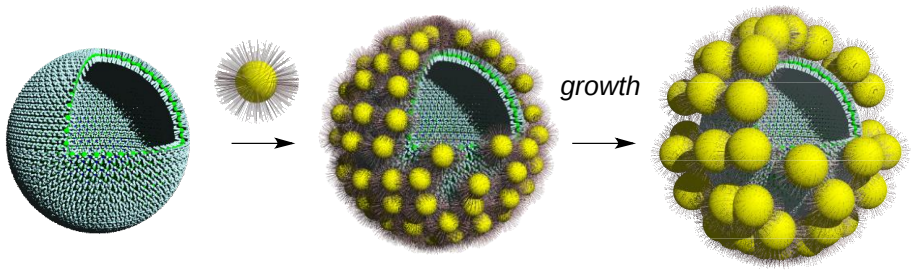

Figure 6-3. Self-assembly of gold nanoparticles on the hydrophobic surface of fullerene vesicles in water.

In chapter 5, dynamic conformational changes of single organic molecules on carbon nanohorns were observed in TEM movies. In a TEM measurement, the molecule is irradiated by electrons of energy proportional to the acceleration voltage. The dynamics of the molecules were accelerated during measurements under a lower acceleration voltage, suggesting that low-energy electrons induce molecular motion more than high-energy electrons. The biphenyl and tetraethylene oxide moieties introduced as rigid and flexible spacers to a single molecule produced complex dynamics. Further analysis of the dynamics and comparison with molecular dynamics simulation suggested that the faster dynamics of this molecular design is a result of the high flexibility of the ethylene oxide spacer, rotation and isomerization of the amide bond, and local conformational minima originated from steric hindrance between biphenyl and the nanohorn surface.

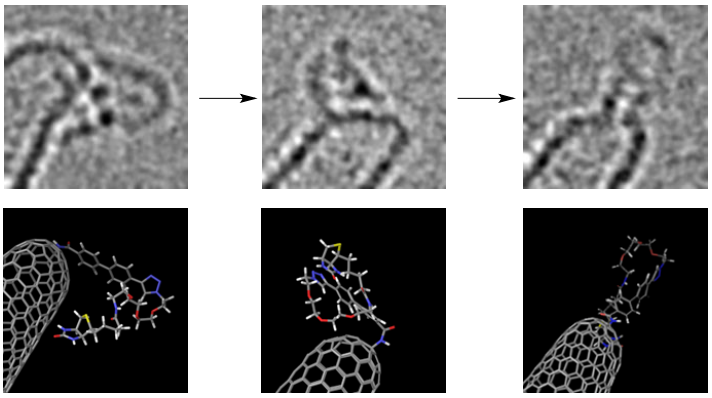

Figure 6-4. Observation of dynamic conformational changes of single organic molecules on a carbon nanohorn by low-acceleration voltage TEM.

The high stability, facile chemical modification and well-defined scaffold of carbon clusters assemblies allowed the construction of hierarchical systems for diverse applications. The fullerene bilayer vesicle, which is stabilized by orthogonal forces (π-π and hydrophobic/fluorous interactions), was used as a binding site for aromatic molecules, a nanoreactor for the synthesis of polymeric objects, and a scaffold for plasmonic vesicles. The morphology of carbon nanohorn aggregates allowed the experimental observation of the dynamics of single organic molecules in electron microscope, which was controlled by the acceleration voltage and molecular design. The methods developed in this thesis pave the way for a new chemistry made possible by the unique properties of carbon clusters.